Ragnar Lehmann

Modelling of Magma Dynamics from the Mantle to the Surface

Dissertation

Dissertation zur Erlangung des Grades eines
'Doktor rerum naturalium (Dr. rer. nat.)' der Fachbereiche:
08 – Physik, Mathematik und Informatik,
09 – Chemie, Pharmazie und Geowissenschaften,
10 – Biologie,
Universitätsmedizin
der Johannes Gutenberg-Universität im Rahmen der
Promotionsordnung des Max Planck Graduate Center

Gutachter
[…]
[…]

Datum der Prüfung
8. April 2016

Modelling of Magma Dynamics from the Mantle to the Surface

Contents

List of Figures

List of Tables

Abstract

Commonly, melt migration in the Earth is modelled by a coupled system of Stokes and Darcy equations governing slowly creeping deformation of highly-viscous (geo)materials and flow in porous media, respectively.

In this work we derive and investigate a discontinuous Galerkin method for the stationary Stokes system using divergence-conforming approximation spaces. Testing it in geodynamically relevant benchmark setups we find that this yields a stable and robust method. However, for fixed computational expenses it was in most cases *not* superior to a second order (continuous) finite element method using discontinuous pressures (Q_2P_1) which is often used in geodynamic modelling softwares.

Then, we focus on the coupled system. We introduce the equations governing the system including constitutive equations for visco-elasto-plastic rheologies relevant on the lithospheric scale, and we derive a stable numerical method using continuous finite elements of Taylor-Hood type. We investigate the experimental order of convergence and show validity of the method and its implementation in benchmark setups relevant for lithosphere dynamics and melt migration.

Applying this method, firstly, we perform a broad parameter study systematically varying physical parameters such as, e.g., the rheology, the tectonic deformational regime, and the geothermal gradient, and examining the corresponding effects. As the study is the first of this type, we learn about interactions of the various parameters in a numerical experiment. Furthermore, we identify physical regimes of efficient melt transport.

Secondly, we focus on multiple subsequent melt pulses and multiple simultaneous pulses. For the latter we employ an unstructured triangular mesh that is adaptively refined in regions of increased porosity for every time step. Again, it is the first application of adaptive meshes in lithospheric scale melt migration modelling using visco-elasto-plastic rheologies.

Zusammenfassung

Der Aufstieg von Gesteinsschmelzen in der Erde wird zumeist mit Hilfe eines Ansatzes modelliert, der die Stokes'schen Gleichungen mit Darcys Gesetz kombiniert. Hierbei bestimmen die Stokes'schen Gleichungen die langsame Verformung hoch-viskoser Materialien (Gesteine) und Darcys Gesetz die Strömung in einem porösen Medium.

In dieser Arbeit leiten wir eine diskontinuierliche Galerkin-Methode für die stationären Stokes'schen Gleichungen her und untersuchen diese. Die Ansatzräume wählen wir divergenzkonform. Mittels geodynamisch relevanter Benchmarks weisen wir die numerische Stabilität und Robustheit der Methode nach. Unter der Voraussetzung gleicher Rechenkapazität stellen wir jedoch im Vergleich mit einer (stetigen) Finite-Elemente-Methode zweiter Ordnung in den meisten Fällen *keinen* Vorteil der diskontinuierlichen Galerkin-Methode fest. Das Q_2P_1-Element mit unstetigem Druck wird in vielen Softwares zur Modellierung geodynamischer Prozesse eingesetzt.

Dann betrachten wir das gekoppelte Stokes/Darcy-System. Wir führen die relevanten Gleichungen einschließlich der für die Lithosphäre bedeutsamen visko-elasto-plastischen Zustandsgleichungen ein und leiten eine stabile numerische Methode her, für die wir Finite Elemente vom Taylor-Hood-Typ einsetzen. Wir untersuchen die experimentelle Konvergenzordnung und weisen die Gültigkeit der Methode und ihrer Implementierung mittels Benchmarks nach, die relevante Mechanismen für Lithosphärendynamik und den Aufstieg von Gesteinsschmelzen umfassen.

Zunächst wenden wir diese Methode in einer breit angelegten Parameterstudie an, in der wir die Auswirkungen systematisch variierter physikalischer Parameter, etwa der Rheologie, der tektonischen Rahmenbedingungen oder des geothermischen Gradienten, untersuchen. Da die Studie die erste ihrer Art ist, gewinnen wir Erkenntnisse über die Interaktion der Parameter in numerischen Experimenten. Ferner identifizieren wir physikalische Rahmenbedingungen für effiziente Transportmechanismen für Gesteinsschmelzen.

Darüber hinaus modellieren wir den Aufstieg mehrerer zeitlich versetzter Pulse sowie mehrerer gleichzeitiger Pulse. Für Letzteres nutzen wir ein unregelmäßiges Dreiecksgitter, das für jeden Zeitschritt in Bereichen erhöhter Porosität adaptiv verfeinert wird. Wiederum ist dies die erste Anwendung von Gitteradaptivität im Bereich der Modellierung des Aufstiegs von Gesteinsschmelzen durch die Lithosphäre unter Berücksichtigung visko-elasto-plastischer Rheologien.

CHAPTER 1

INTRODUCTION

WHY SHOULD WE MODEL MELT MIGRATION?

Only 1 % of the Earth's land surface is covered by volcanically active regions. Yet, roughly 500 million people live in these regions. Apart from hazardous events, magmatism also has significant economic effects, as, e.g., some of these regions are relevant in obtaining geothermal energy, many large ore deposits correlate to (previously) active magmatism [1], and volcanic soils have proved to be fertile for agricultural purposes [2].

Despite the significance of the subject and increasing research there is still an endless list of unresolved (or partially resolved) questions related to magmatism. How does melt rise through the Earth's mantle and crust? In what kind of physical regimes does it reach the surface? How much reaches the surface? How do plumbing systems of volcanoes work? How is the melt migration process affected by large scale tectonic deformation?

Of course, there has been progress over the last decades regarding some of these questions. There are geological field observations of volcanic and plutonic rocks, geophysical obervations give indications on the present-day setup of the crustal setup below volcanoes. However, today's "snapshot" geological record as a result of millions of years of magmatic activities, deformation, crystallization, eruptions, provides only a very small window to the history behind. Interpreting this data to formulate a physically consistent model of how melt propagates through the Earth's lithosphere is subject of ongoing research.

Magmatic systems typically occur either at spreading regions (mid-oceanic ridges, continental rifts) or in the vicinity of subduction zones. In a subduction

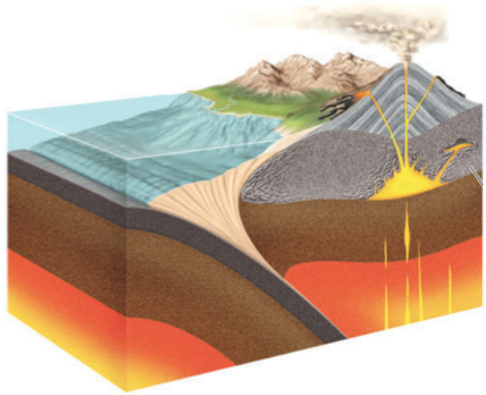

Figure 1.1: Illustration of ocean-continent subduction zone, taken from [3, ch. 3]. Oceanic lithosphere subducts under a contintent bringing down water-rich sediments and basalts to great depths. At high pressure and temperature the water is released to the mantle reducing its melting temperature. Magma accumulates and, due to the density difference, rises towards the surface.

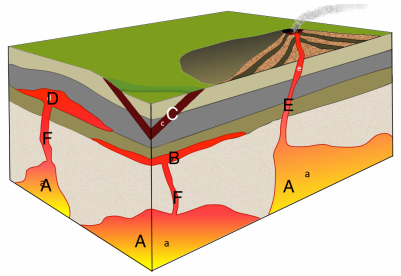

Figure 1.2: Top left: Schematic illustration of types of plutons (modified from [4, ch. 3]). A: stocks (might constitute a batholith if crystallized at depth), B: sill (tabular body, parallel to bedding), C: dike (cross-cuts bedding), D: laccolith (a sill having pushed up overlying rock layers), E: pipe (cylindrical conduit feeding a volcano), F: these features could be be pipes or dikes, depending on their 3D structure.

Bottom left: Photo of intrusive sill on Réunion island by B.navez via Wikimedia Commons, https://commons.wikimedia.org/wiki/File%3AReunion_Mafate_sill.JPG.

Right: Photo by T. Eliasson of the Geological Survey of Sweden showing "light-gray igneous intrusion in Sweden cut by a younger white pegmatite dike, which in turn is cut by an even younger black diabase dike", https://commons.wikimedia.org/wiki/File:Multiple_Igneous_Intrusion_Phases_Kosterhavet_Sweden.jpg.

zone setup the most common concept of how melt migration initializes is the following [3, ch. 4], cp. Figure 1.1: When oceanic lithosphere subducts under a continent basalts and sediments with enriched water content are brought down. At high pressures and temperatures the water is released to the surrounding mantle and the subducted material partially melts. An increasing water content reduces the solidus temperature of the mantle rock. The result is a partially molten melange of mantle material and oceanic crust that, due to buoyancy, starts rising towards the continental crust.

While the description hides a lot of the complexity involved in this process (e.g., metamorphism of subducted material, chemically bound water vs. water in pores), it only brings us to the starting point of the even more enigmatic ascent of the partially molten material. Conceptual "cartoon" models of the melt ascent are presented in virtually every introductory geosciences textbook, see Figure 1.1. Melt pulses might first rise as a diapir in a viscously deforming mantle host rock. In shallower depths the ascent transitions into a combination of diapiric, porous and channelling flow. When being exhumed, intrusive dike and sill structures can be observed, i.e., small (meter) scale vertical and horizontal structures of magmatic origin that crystallized in crustal depths, see Figure 1.2. Measurements of, e.g., seismic velocities imply the existence of very complex magmatic network below volcanoes [5, 6]. Yet, the interpretation of the data is cumbersome and has many free parameters.

Hence, the number of constraints for conceptual models of melt ascent is small and it is unknown whether existing models are accurate and physically consistent. Numerical modelling is probably the most attractive tool to provide a quantitative complement.

Stokes Flow in Geodynamic Modelling

Geomaterials deforming over geological timescales are usually modeled with the Stokes equations describing slowly creeping motion where viscous forces dominate over (negligible) advective inertial forces, i.e., in the limit of a small Reynolds number ($\mathrm{Re} \ll 1$) [7, sec. 6-14]. Coupling this with the assumption of incompressibility leads to the following quasi-static system of equations,

$$-\nabla \cdot \boldsymbol{\tau} + \nabla p = -\varrho \boldsymbol{g}, \tag{1.1a}$$

$$\nabla \cdot \boldsymbol{v} = 0, \tag{1.1b}$$

where $\boldsymbol{\tau} \equiv \boldsymbol{\tau}(\boldsymbol{v}, \eta, \ldots)$ denotes the deviatoric stress, $\boldsymbol{v}$ velocity, η viscosity, p pressure, ϱ density, $\boldsymbol{g}$ gravitational acceleration. Typically, density and viscosity fields are advected with the flow via a complementary advection equation, see, e.g., [8–10].

The discretization of the fluid flow problem (1.1) with common grid-based methods yields a saddle-point problem with a coefficient matrix that is very large, ill-conditioned and indefinite [11]. The condition number is strongly affected by the contrast in viscosity that can easily span six or more orders of magnitude over the computational domain. Even locally it can vary by several orders of magnitude, e.g., at material interfaces or in zones of shear localization.

As geomaterials are non-Newtonian fluids, their rheological behavior introduces nonlinearities into the system that require an iterative solution procedure: *(i)* determine viscosity depending on current guess for, e.g., the rate of strain, *(ii)* assemble system matrix and solve system, back to *(i)* until some convergence criterion is met.

While models of mantle convection are usually restricted to viscous deformation, see, e.g., [12, 13], lithosphere dynamics also feature elastic stress accumulation and plastic failure. In geodynamic applications plastic deformation is typically modeled with an effective viscosity approach, altering iteratively the viscoelastic constitutive relationship to not let the stress state exceed the failure envelope [14–16].

The mentioned complexities in models of lithosphere dynamics give rise to searching modern numerical methods. Therefore, we studied a discontinuous Galerkin (DG) method for stationary Stokes flow with strongly variable viscosity. In chapter 2 we present the derivation of a DG method and a benchmark comparison of standard finite elements in a continuous Galerkin framework with tailored divergence-free elements in a DG framework. The chapter has been published in *ZAMM – Journal of Applied Mathematics and Mechanics/Zeitschrift für Angewandte Mathematik und Mechanik*. See [17] for its full bibliographic record.

Towards a Mathematical Model of Melt Migration

Apart from slowly creeping motion (Stokes flow), a proper model of melt migration also needs to consider flow in porous media as described by Darcy's law. Coupling these two flow regimes has also been studied in other areas of research such as interactions of surface and groundwater flows or studying permeability in carbonate reservoirs with cavities and fractures.

The Stokes-Darcy-Brinkman approach merges the two flow regimes into a single momentum equation that reduces to the end-member cases Stokes or Darcy flow for suitable coefficients [18–21]. Another approach enforces either Stokes or Darcy equations locally on subdomains, coupled with appropriate interface conditions. There are two major classes of numerical meth-

ods for this system: iteratively solving the Stokes and Darcy problem separately [22, 23], or solving a monolithic system in a single step, see below. Approaches similar to the latter one have also been investigated for coupled Navier-Stokes/Darcy problems [24–27].

In the class of monolithic methods the Stokes/Darcy case has for example been tackled with continuous finite elements [28–32]. As these lead to unbalanced rates of convergence for the two subproblems different approaches were presented, such as the combinations of mixed finite elements (for Darcy region) and a discontinuous Galerkin method (for Stokes region) [33–35] or a reformulation of discretized Darcy flow combined with arbitrary stable Galerkin finite element methods for Stokes flow [36]. Egger and Waluga [37] presented a hybridized discontinuous Galerkin method that is capable of solving the Stokes equations, the Darcy equations or the coupled problem in a unified manner.

A recent and promising approach for Darcy flow has been presented by Lin et al. [38] based on so-called weak Galerkin finite elements (WGFEM) [39]. This method is locally conservative and, in contrast to mixed finite elements, the resulting system is positive definite. Furthermore, no tuning of problem-dependent penalty parameters is required as in the discontinuous Galerkin method. However, this method has not been considered in the context of a coupled Stokes/Darcy problem.

So far, the described methods consider a set of subdomains where either Stokes or Darcy flow applies. When we consider partially molten rocks we fail to identify clear boundaries of where to apply one or the other flow regime. Since McKenzie's work on partially molten rocks incorporating Darcy's law into the conservation equations and combining it with a compacting solid matrix [40] most models of melt migration in the last 30 years have followed this path.

In the following years there has been theoretical and numerical research on different modes of melt migration. Studies have dealt with different aspects of viscous or porous two-phase flow, e.g., solitary wave propagation [41, 42], melt ascent at midoceanic ridges [43–45], decompaction channeling [46] or formation of dikes [47]. Yet, these models have in common that they consider particular deformation modes and, hence, *a priori* prescribe the deformation mode in the respective model, i.e., diapiric, percolative, diking, channeling. Obviously, with such constraints it is not possible to recover all phases of the melt propagating through the Earth's mantle and crust in a single model.

Based on the mentioned references and on the work by Bercovici et al. [48], recently Keller et al. [16] reformulated McKenzie's model in the context of lithospheric scale melt migration advancing it in multiple ways: they intro-

duced visco-elasto-plastic rheologies to the system via appropriate constitutive equations, presented it as an extension to the well understood Stokes flow the way it is implemented in many geodynamic numerical modelling softwares, and formulated it symmetrically such that discretizations lead to symmetric matrices that are faster to solve for. In particular, they derived the so-called three-field formulation for the fluid flow referring to the major unknowns solid velocity, fluid pressure and compaction pressure, which proved to be superior to previous formulations, especially in terms of numerical stability when being discretized [49].

In chapter 3 we are going to review the fluid flow system described by Keller et al. and present a formal mathematical derivation of a stable numerical method to solve it overcoming methodological issues of their approach. We present some numerical experiments obtaining experimental orders of convergence and proving validity of the method and its implementation in geodynamically relevant physical regimes.

In the 4th chapter we present a study on lithospheric scale models varying physical parameters such as the background strainrate (representing large-scale tectonic deformation), the size of the melt pulse, the rheology of the crust and the mantle etc., and discuss the implications.

In chapter 5 we focus on certain aspects of melt migration modelling, particularly, multiple subsequent pulses and mesh adaptivity, before we summarize our findings and provide an outlook of future projects in the final chapter.

References

[1] G. P. L. Walker. Basaltic Volcanoes and Volcanic Systems. In H. Sigurdsson, editor, *Encyclopedia of Volcanoes*, pages 283–289. Academic Press, San Diego, CA, 2000.

[2] C.-L. Ping. Volcanic Soils. In H. Sigurdsson, editor, *Encyclopedia of Volcanoes*, pages 1259–1270. Academic Press, San Diego, CA, 2000.

[3] J. Grotzinger, T. H. Jordan, F. Press, and R. Siever. *Allgemeine Geologie (orig. Understanding Earth)*. Springer, Berlin, Heidelberg, 5th edition, 2011. ISBN 978-3-827-41828-8.

[4] S. Earle. *Physical Geology*. British Columbia: BCcampus, retrieved from http://opentextbc.ca/geology/, 2015.

[5] E. Auger, P. Gasparini, J. Virieux, and A. Zollo. Seismic Evidence of an Extended Magmatic Sill Under Mt. Vesuvius. *Science*, 294(5546):1510–1512, 2001. ISSN 0036-8075. DOI:10.1126/science.1064893.

[6] H.-H. Huang, F.-C. Lin, B. Schmandt, J. Farrell, R. B. Smith, and V. C. Tsai. The Yellowstone magmatic system from the mantle plume to the upper crust. *Science*, 348(6236):773–776, 2015. ISSN 0036-8075. DOI:10.1126/science.aaa5648.

[7] D. L. Turcotte and G. Schubert. *Geodynamics*. Cambridge University Press, 2nd edition, 2002. ISBN 978-0-521-66624-4.

[8] H. Schmeling, A. Y. Babeyko, A. Enns, C. Faccenna, F. Funiciello, T. Gerya, G. J. Golabek, S. Grigull, B. J. P. Kaus, G. Morra, S. M. Schmalholz, and J. van Hunen. A benchmark comparison of spontaneous subduction models—Towards a free surface. *Physics of the Earth and Planetary Interiors*, 171(1–4):198–223, 2008. ISSN 0031-9201. DOI:10.1016/j.pepi.2008.06.028.

[9] T. Duretz, D. A. May, T. V. Gerya, and P. J. Tackley. Discretization errors and free surface stabilization in the finite difference and marker-in-cell method for applied geodynamics: A numerical study. *Geochemistry, Geophysics, Geosystems*, 12(7):1200–1225, 2011. ISSN 1525-2027. DOI:10.1029/2011GC003567.

[10] M. Furuichi and D. A. May. Implicit solution of the material transport in Stokes flow simulation: Toward thermal convection simulation surrounded by free surface. *Computer Physics Communications*, 192:1–11, 2015. ISSN 0010-4655. DOI:10.1016/j.cpc.2015.02.011.

[11] S. A. Melchior, V. Legat, P. van Dooren, and A. J. Wathen. Analysis of preconditioned iterative solvers for incompressible flow problems. *International Journal for Numerical Methods in Fluids*, 68(3):269–286, 2012. DOI:10.1002/fld.2505.

[12] K. Stemmer, H. Harder, and U. Hansen. A new method to simulate convection with strongly temperature- and pressure-dependent viscosity in a spherical shell: Applications to the Earth's mantle. *Physics of the Earth and Planetary Interiors*, 157(3–4):223–249, 2006. ISSN 0031-9201. DOI:10.1016/j.pepi.2006.04.007.

[13] P. J. Tackley. Modelling compressible mantle convection with large viscosity contrasts in a three-dimensional spherical shell using the yin-yang grid. *Physics of the Earth and Planetary Interiors*, 171(1–4):7–18, 2008. DOI:10.1016/j.pepi.2008.08.005.

[14] L. Moresi, F. Dufour, and H.-B. Mühlhaus. A Lagrangian integration point finite element method for large deformation modeling of viscoelastic geomaterials. *Journal of Computational Physics*, 184(2):476–497, 2003. ISSN 0021-9991. DOI:10.1016/S0021-9991(02)00031-1.

[15] B. J. P. Kaus. Factors that control the angle of shear bands in geodynamic numerical models of brittle deformation. *Tectonophysics*, 484(1–4):36–47, 2010. ISSN 0040-1951. DOI:10.1016/j.tecto.2009.08.042.

[16] T. Keller, D. A. May, and B. J. P. Kaus. Numerical modelling of magma dynamics coupled to tectonic deformation of lithosphere and crust. *Geophysical Journal International*, 195(3):1406–1442, 2013. DOI:10.1093/gji/ggt306.

[17] R. S. Lehmann, M. Lukáčová-Medvid'ová, B. J. P. Kaus, and A. A. Popov. Comparison of continuous and discontinuous Galerkin approaches for variable-viscosity Stokes flow. *ZAMM – Journal of Applied Mathematics and Mechanics/Zeitschrift für Angewandte Mathematik und Mechanik*, 2015. ISSN 1521-4001. DOI:10.1002/zamm.201400274.

[18] H. C. Brinkman. A calculation of the viscous force exerted by a flowing fluid on a dense swarm of particles. *Applied Scientific Research*, 1(1):27–34, 1949. ISSN 0003-6994. DOI:10.1007/BF02120313.

[19] X. Xie, J. Xu, and G. Xue. Uniformly Stable Finite Element Methods for Darcy-Stokes-Brinkman Models. *Journal of Computational Mathematics*, 26(3):435–455, 2008.

[20] N. Chen, M. Gunzburger, and X. Wang. Asymptotic analysis of the differences between the Stokes-Darcy system with different interface conditions and the Stokes-Brinkman system. *Journal of Mathematical Analysis and Applications*, 368(2):658–676, 2010. ISSN 0022-247X. DOI:10.1016/j.jmaa.2010.02.022.

[21] M. Krotkiewski, I. S. Ligaarden, K.-A. Lie, and D. W. Schmid. On the Importance of the Stokes-Brinkman Equations for Computing Effective Permeability in Karst Reservoirs. *Communications in Computational Physics*, 10(05):1315–1332, 2011. ISSN 1991-7120. DOI:10.4208/cicp.290610.020211a.

[22] M. Discacciati, A. Quarteroni, and A. Valli. Robin-Robin Domain Decomposition Methods for the Stokes-Darcy Coupling. *SIAM Journal on Numerical Analysis*, 45(3):1246–1268, 2007. DOI:10.1137/06065091X.

[23] A. Caiazzo, V. John, and U. Wilbrandt. On classical iterative subdomain methods for the Stokes-Darcy problem. *Computational Geosciences*, 18(5):711–728, 2014. DOI:10.1007/s10596-014-9418-y.

[24] M. Discacciati and A. Quarteroni. Navier-Stokes/Darcy coupling: Modeling, Analysis, and Numerical Approximation. *Revista Matemática Complutense*, 22(2):315–426, 2009. DOI:10.5209/rev_REMA.2009.v22.n2.16263.

[25] L. Badea, M. Discacciati, and A. Quarteroni. Numerical Analysis of the Navier-Stokes/Darcy Coupling. *Numerische Mathematik*, 115(2):195–22, 2010. DOI:10.1007/s00211-009-0279-6.

[26] A. Çeşmelioğlu and B. Rivière. Existence of a weak solution for the fully coupled Navier-Stokes/Darcy-transport problem. *Journal of Differential Equations*, 252(7):4138–4175, 2012. ISSN 0022-0396. DOI:10.1016/j.jde.2011.12.001.

[27] A. Çeşmelioğlu, V. Girault, and B. Rivière. Time-dependent coupling of Navier-Stokes and Darcy flows. *ESAIM: Mathematical Modelling and Numerical Analysis*, 47:539–554, 2013. ISSN 1290-3841. DOI:10.1051/m2an/2012034.

[28] M. Discacciati, E. Miglio, and A. Quarteroni. Mathematical and numerical models for coupling surface and groundwater flows. *Applied Numerical Mathematics*, 43(1–2):57–74, 2002. ISSN 0168-9274. DOI:10.1016/S0168-9274(02)00125-3. 19th Dundee Biennial Conference on Numerical Analysis.

[29] T. Arbogast and H. L. Lehr. Homogenization of a Darcy-Stokes system modeling vuggy porous media. *Computational Geosciences*, 10(3):291–302, 2006. DOI:10.1007/s10596-006-9024-8.

[30] T. Arbogast and D. S. Brunson. A computational method for approximating a Darcy-Stokes system governing a vuggy porous medium. *Computational Geosciences*, 11(3):207–218, 2007. ISSN 1573-1499. DOI:10.1007/s10596-007-9043-0.

[31] J. M. Urquiza, D. N'Dri, A. Garon, and M. C. Delfour. Coupling Stokes and Darcy equations. *Applied Numerical Mathematics*, 58(5):525–538, 2008. ISSN 0168-9274. DOI:10.1016/j.apnum.2006.12.006.

[32] T. Arbogast and M. S. M. Gomez. A discretization and multigrid solver for a Darcy-Stokes system of three dimensional vuggy porous media. *Computational Geosciences*, 13(3):331–348, 2009. DOI:10.1007/s10596-008-9121-y.

[33] B. Rivière and I. Yotov. Locally Conservative Coupling of Stokes and Darcy Flows. *SIAM Journal on Numerical Analysis*, 42(5):1959–1977, 2005. DOI:10.1137/S0036142903427640.

[34] G. Kanschat and B. Rivière. A strongly conservative finite element method for the coupling of Stokes and Darcy flow. *Journal of Computational Physics*, 229(17):5933–5943, 2010. ISSN 0021-9991. DOI:10.1016/j.jcp.2010.04.021.

[35] V. Girault, G. Kanschat, and B. Rivière. Error analysis for a monolithic discretization of coupled Darcy and Stokes problems. *Journal of Numerical Mathematics*, 22(2):109–142, 2014. DOI:10.1515/jnma-2014-0005.

[36] M. R. Correa and A. F. D. Loula. A unified mixed formulation naturally coupling Stokes and Darcy flows. *Computer Methods in Applied Mechanics and Engineering*, 198(33–36):2710–2722, 2009. ISSN 0045-7825. DOI:10.1016/j.cma.2009.03.016.

[37] H. Egger and C. Waluga. A Hybrid Discontinuous Galerkin Method for Darcy-Stokes Problems. In R. Bank, M. Holst, O. Widlund, and J. Xu, editors, *Domain Decomposition Methods in Science and Engineering XX*, pages 663–670. Springer, Berlin, Heidelberg, 2013. ISBN 978-3-642-35275-1. DOI:10.1007/978-3-642-35275-1_79.

[38] G. Lin, J. Liu, L. Mu, and X. Ye. Weak Galerkin finite element methods for Darcy flow: Anisotropy and heterogeneity. *Journal of Computational Physics*, 276:422–437, 2014. ISSN 0021-9991. DOI:10.1016/j.jcp.2014.07.001.

[39] J. Wang and X. Ye. A weak galerkin finite element method for second-order elliptic problems. *Journal of Computational and Applied Mathematics*, 241:103–115, 2013. ISSN 0377-0427. DOI:10.1016/j.cam.2012.10.003.

[40] D. P. McKenzie. The Generation and Compaction of Partially Molten Rock. *Journal of Petrology*, 25(3):713–765, 1984. DOI:10.1093/petrology/25.3.713.

[41] V. Barcilon and F. M. Richter. Nonlinear waves in compacting media. *Journal of Fluid Mechanics*, 164:429–448, 1986.

[42] M. Spiegelman. Flow in deformable porous media. Part 2—Numerical analysis – the relationship between shock waves and solitary waves. *Journal of Fluid Mechanics*, 247:39–63, 1993. ISSN 1469-7645. DOI:10.1017/S0022112093000370.

[43] W. R. Buck and W. Su. Focused mantle upwelling below mid-ocean ridges due to feedback between viscosity and melting. *Geophysical Research Letters*, 16(7):641–644, 1989. ISSN 1944-8007. DOI:10.1029/GL016i007p00641.

[44] D. R. Scott and D. J. Stevenson. A self-consistent model of melting, magma migration and buoyancy-driven circulation beneath mid-ocean ridges. *Journal of Geophysical Research: Solid Earth*, 94(B3):2973–2988, 1989. ISSN 2156-2202. DOI:10.1029/JB094iB03p02973.

[45] R. F. Katz. Porosity-driven convection and asymmetry beneath mid-ocean ridges. *Geochemistry, Geophysics, Geosystems*, 11(11):Q0AC07, 2010. ISSN 1525-2027. DOI:10.1029/2010GC003282.

[46] J. A. D. Connolly and Y. Y. Podladchikov. Decompaction weakening and channeling instability in ductile porous media: Implications for asthenospheric melt segregation. *Journal of Geophysical Research: Solid Earth*, 112(B10), 2007. DOI:10.1029/2005JB004213.

[47] A. Y. Rozhko, Y. Y. Podladchikov, and F. Renard. Failure patterns caused by localized rise in pore-fluid overpressure and effective strength of rocks. *Geophysical Research Letters*, 34(22): L22304, 2007. DOI:10.1029/2007GL031696.

[48] D. Bercovici, Y. Ricard, and G. Schubert. A two-phase model for compaction and damage: 1. General Theory. *Journal of Geophysical Research: Solid Earth*, 106(B5):8887–8906, 2001. ISSN 2156-2202. DOI:10.1029/2000JB900430.

[49] S. Rhebergen, G. N. Wells, A. J. Wathen, and R. F. Katz. Three-Field Block Preconditioners for Models of Coupled Magma/Mantle Dynamics. *SIAM Journal on Scientific Computing*, 37 (5):A2270–A2294, 2015. DOI:10.1137/14099718X.

The following chapter has been published in *ZAMM – Journal of Applied Mathematics and Mechanics/Zeitschrift für Angewandte Mathematik und Mechanik*. Its full bibliographic record is provided below. It was co-authored by Mária Lukáčová-Medvid'ová, Boris Kaus and Anton Popov.

R. S. Lehmann, M. Lukáčová-Medvid'ová, B. J. P. Kaus, A. A. Popov. Comparison of continuous and discontinuous Galerkin approaches for variable-viscosity Stokes flow. *ZAMM – Journal of Applied Mathematics and Mechanics/Zeitschrift für Angewandte Mathematik und Mechanik*, 2015. DOI:10.1002/zamm.201400274.

CHAPTER 2

Comparison of Continuous and Discontinuous Galerkin Approaches for Variable-Viscosity Stokes Flow

2.1 Introduction and Geophysical Motivation

Numerical simulations of geological and geodynamic processes is an important and growing research field which helps to interprete geological observations in a physically meaningful manner. Typical questions that are addressed include: How are sedimentary basins formed (e.g., [1])? How do lithospheric plates collide and how are mountains formed (e.g., [2–5])? Why do we have plate tectonics on Earth and not on other planets (e.g., [6, 7])? What is the rheology of magma [8] and how does magma move through the Earth and why does it only sometimes result in volcanic eruptions [9]? How does mantle convection work [7], and was this different in the early Earth [10]? While the rheology of rocks is rather complex and nonlinear and is best described as viscoelastoplastic, inertial terms are not important for these processes and the governing equations that need to be solved in this case are often very similar to the incompressible Stokes equations [7, 11–14]. Yet, different than in many classical CFD applications, geological processes have viscosities that vary by many orders of magnitude over spatially small domains as the viscosity of rocks depends on pressure, temperature, strain rate. The location of these viscosity jumps are typically not known a-priori but might form spontaneously during a simulation, for example when a plastic shear band forms [15]. Obviously, geodynamic models need to capture these variations, see, e.g., [9, 16, 17]. The reliability of the numerical method is influenced by its stability and accuracy for the case of discontinuous model parameters, cf. [18, 19].

Most geodynamic models contain a Stokes flow component, e.g. [20–22], as typical time scales are long, inertial effects are negligible and rocks can often be considered nearly incompressible. Therefore, finding a good way of solving the Stokes system is likely to contribute to a better understanding of, e.g., mantle convection, subduction of tectonic plates or continental collision. The choice of the discretization method represents the first step in that solution process. Grid-based methods such as finite differences [12, 23], finite elements and finite volumes [24] are predominantly used. Each of these methods algebraically yields a saddle point problem with a coefficient matrix that is, typically, very large, ill-conditioned and indefinite [25]. Particularly for solving 3D problems, massively parallel systems need to be solved, for which iterative methods are crucial although finding fast methods is still an open question, cf. [26]. We refer to recent works dealing with block preconditioning with algebraic multigrid [25, 27, 28], Krylov subspace methods on decoupled and fully coupled systems [22, 29] and projection-based preconditioners [30, 31].

The Finite Element Method (FEM) is one of the standard means for the simulation of geodynamic processes used in, e.g., [32–37]. However, the "natural" trade-off between accuracy and computational expenses accounts for searching enhanced methods. As discontinuous Galerkin methods have been demonstrated to be very efficient for solving (seismic) wave propagation in heterogeneous media [38], they might be useful for solving variable viscosity Stokes problems as well. Our aim is therefore to test how the Continuous Galerkin (CG) and the Discontinuous Galerkin (DG) methods compare with the two most commonly used quadrilateral elements for Stokes flow (Q_1P_0 and Q_2P_1). We do not consider the Q_1Q_1/stab element [39–41], as stabilization of this element is achieved by introducing an artificial compressibility that dominates for flows mainly driven by buoyancy variations [37]. In geophysical flow models this yields unphysical pressure artifacts for cases where both the free surface of the Earth and mantle flow are considered, because the driving density contrast between cold sinking plates and the warmer surrounding Earth's mantle is much smaller than the density difference between rocks and air [15, 35, 36]. In our experience, this results in artificial "compaction" of the Earth's mantle if Q_1Q_1/stab element is used, which makes them unsuitable for these purposes.

The DG method generalizes the FEM by eliminating continuity constraints and providing the tools to handle potential jumps via numerical fluxes. In this respect it transfers a classical advantage of the finite volume methods to a finite element approach [42]. Hence, it provides additional flexibility in designing the shape functions that are discontinuous, and means to stabilize discontinuities or steep gradient regions. DG methods are inherently local requiring less communication between neighbouring mesh cells. This facili-

tates the enforcement of local mass conservation (i.e., per mesh cell) [43–45], the development of multiscale methods [46], *hp*-adaptivity [47, 48] and parallelization [49, 50]. On the other hand, DG methods yield additional degrees of freedom compared to CG.

Since about two decades DG methods have become increasingly popular in the mathematical community [51, 52] and are tested and used more and more in different fields of applications. Geophysical applications using DG methods are hitherto mainly restricted to seismology (wave modelling, waveform inversion), see, e.g., [38, 53, 54]. Wilcox et al. [38] give as reasons for employing a DG method (among others) strong wave speed contrasts and the need for *h*-adaptive non-conforming meshes to track solution features. Although steep gradients and discontinuities are present in solutions and material properties of typical geodynamic models, so far DG methods have not been applied to common geodynamic model benchmarks. The aim of this paper is to realize a first step in this direction. We employ $H(\mathrm{div})$-conforming elements of Raviart-Thomas and of Brezzi-Douglas-Marini kind. Thus, the velocity approximation is globally divergence free in the Sobolev space H^1, cf. (2.4c). It is a well-known fact that exactly divergence-free basis functions can be advantageous for the approximation of the Navier-Stokes and Darcy flows, see, e.g., [55, 56].

This article is organized as follows: in section 2.2 we give a brief review on the main differences between CG and DG methods, present the elements, show the derivation of a DG scheme for the Stokes flow, and describe the benchmark setups we used in the numerical experiments. In particular, we enforce local mass conservation by preserving the divergence-free condition using div-conforming approximation for velocities in our DG scheme as described in section 2.2.3. In section 2.3 we confer the results of the benchmark setups and the computational costs arising from the different elements and schemes. Finally, these results are discussed and conclusions are drawn.

2.2 Derivation of the Numerical Method

2.2.1 Governing Equations

Stokes flow plays a major role in geodynamic processes like, e.g., mantle convection. It is also called creeping motion describing a flow where viscous forces dominate over inertial forces. If the material is assumed to be incompressible, Stokes flow can be described by the following conservation laws of momentum and mass:

$$-\nabla \cdot \boldsymbol{\tau} + \nabla p = -\varrho g \hat{\boldsymbol{z}}, \tag{2.1a}$$

$$\nabla \cdot \boldsymbol{v} = 0, \tag{2.1b}$$

where $\boldsymbol{v}$ denotes the velocity, p pressure, $\boldsymbol{\tau}$ the deviatoric stress tensor, ϱ density, g the gravitational acceleration and $\hat{\boldsymbol{z}}$ the unity vector pointing in (vertical) z direction. The equation of state specifying the deviatoric stress $\boldsymbol{\tau}$ completes the system,

$$\boldsymbol{\tau} = 2\mu\dot{\boldsymbol{\varepsilon}}, \tag{2.2}$$

where μ denotes the viscosity and $\dot{\boldsymbol{\varepsilon}} \equiv \dot{\boldsymbol{\varepsilon}}(\boldsymbol{v}) = {}^1/_2\left(\nabla\boldsymbol{v} + \nabla\boldsymbol{v}^{\mathsf{T}}\right)$ the strain rate. In the following, we only consider the 2D case with (x, z) coordinates and the following boundary conditions,

$$\text{Free-slip:} \qquad \boldsymbol{v}\cdot\boldsymbol{n} = 0, \quad \frac{\partial \boldsymbol{v}}{\partial \boldsymbol{n}} = 0 \quad \text{on } \Gamma_1 \subset \partial\Omega, \tag{2.3a}$$

$$\text{No-slip:} \qquad \boldsymbol{v} = 0 \quad \text{on } \Gamma_2 \subset \partial\Omega, \tag{2.3b}$$

where $\boldsymbol{n}$ is the normal and tangential unit vectors on the boundaries Γ_1, Γ_2 of the open domain Ω; $\Gamma_1 \cup \Gamma_2 = \partial\Omega$, $\Gamma_1 \cap \Gamma_2 = \emptyset$.

2.2.2 Overview – CG and DG

The CG method (classical FEM) is a numerical method for solving (systems of) differential equations. It is based on *(i)* a computational domain discretized into cells of finite (not infinitesimal) size (finite elements), *(ii)* a variational formulation of the differential equation and *(iii)* a finite set of shape functions, each one being non-zero only on a small patch of mesh cells. The shape functions are usually chosen as piecewise polynomials that form a basis of a discrete space approximating the solution space, cf. section 2.2.3. Being a linear combination of those shape functions, also the approximate solution is piecewise polynomial.

The DG method generalizes the FEM in such a way that in general no continuity along the mesh cell edges is enforced. Thus, the approximate solution is piecewise polynomial, meaning polynomial on every single mesh cell. However, it may have jumps across the cell edges of the mesh. This jump resembles a non-zero *flux* from one mesh cell to the adjacent one given by the cell interface integrals. Describing and handling this flux is the main difference in the numerical scheme for a CG and a DG method.

2.2.3 Numerical Scheme

In what follows we will derive a numerical approximation of (2.1)–(2.3). We will in particular concentrate on the derivation of the DG method, since the CG

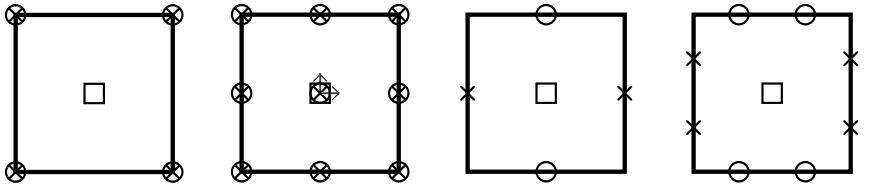

Figure 2.1: Degrees of freedom (DOFs) for the elements Q_1P_0, Q_2P_1, lowest-order Raviart-Thomas RT_0P_0 and Brezzi-Douglas-Marini BDM_1P_0 (left to right). Crosses and circles denote DOFs for horizontal and vertical velocity, respectively. Squares and arrows denote pressure and pressure gradient DOFs.

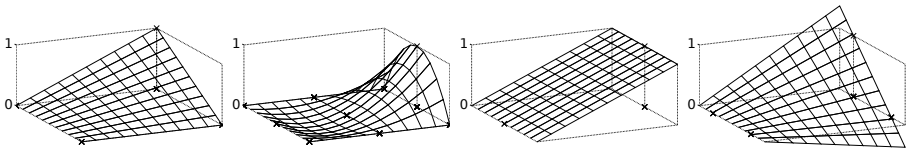

Figure 2.2: Instances of basis functions for (horizontal) velocity component of the elements Q_1P_0, Q_2P_1, RT_0P_0, BDM_1P_0 (left to right).

FEM is a standard method also in the framework of geophysical applications. Let $\Omega \subset \mathbf{R}^2$ be an open, bounded polygonal computational domain and $\mathcal{T}_h$ ($h > 0$ is a mesh parameter denoting the maximal edge length) denote a partition of the closure $\bar{\Omega}$ into a finite number of mesh elements. We denote a general mesh element by E and set $\mathcal{T}_h := \{E_i\}_{i \in I}$, where I is a suitable index set of all elements. We call two elements E_i, E_j neighbouring elements, if $E_i \cap E_j$ contains their common edge. We will only consider quadrilateral elements in this article, but results can be generalized also to the triangular case.

The approximate solution to our problem (2.1)–(2.3) is sought in the space of polynomial functions. We denote by $P_k(E)$ the space of polynomials of (total) degree $\leq k$ on a mesh element E and $Q_k(E) = P_{k,k}(E)$, where

$$P_{k_1,k_2}(E) = \left\{ p(x_1, x_2) \,\middle|\, p(x_1, x_2) = \textstyle\sum_{i \leq k_1, j \leq k_2} a_{ij} x_1^i x_2^j \right\}.$$

Finite Element Basis Before introducing suitable discrete spaces $\boldsymbol{X}_h$ and Q_h which are used for the velocity and pressure discretization, we first present different finite element bases that are used in our numerical schemes. The elements listed below are, except for Q_1P_0, inf-sup stable, i.e., they fulfill the so-called LBB or inf-sup stability condition, see [57].

Q_1P_0 Element Although proven to be unstable [58] the seemingly easy-to-use Q_1P_0 element with bilinear velocity and piecewise constant pressure

shape functions is still heavily applied in practice. Therefore, we will use it as a reference pointing out its benefits and limitations.

Raviart-Thomas Element For elliptic problems this element has been introduced in 1977 [59]. We will consider only the lowest-order Raviart-Thomas element $\mathrm{RT}_0\mathrm{P}_0$. The velocity components can locally be written as $\mathrm{RT}_0(E) = \mathrm{P}_{1,0}(E) \times \mathrm{P}_{0,1}(E)$. Globally, the horizontal velocity component is piecewise linear and continuous in horizontal direction and piecewise constant and discontinuous in vertical direction. The vertical velocity component is the other way around, i.e., piecewise linear and continuous in vertical direction and piecewise constant and discontinuous in horizontal direction. The matching pressure space P_0 is piecewise constant and discontinuous.

As shown in [60] for the isoviscous case, the $\mathrm{RT}_0\mathrm{P}_0$ element in the corresponding numerical scheme resembles the finite difference (FD) staggered grid stencil. Raviart-Thomas elements of order k can, therefore, be considered a higher-order generalization of the FD method working on irregular meshes. Limitations to this consideration are given in section 2.3 for geodynamic benchmarks.

Brezzi-Douglas-Marini Element This element type has been introduced in 1985 [61] following the Raviart-Thomas element in its approach to design a discrete basis of $H_0(\mathrm{div}, \Omega)$, cf. (2.4c), see also [62, §III.3]. Locally, it is bilinear like the $\mathrm{Q}_1\mathrm{P}_0$ element, $\mathrm{BDM}_1(E) = \mathrm{Q}_1(E)^2$ with $\mathrm{Q}_1(E)$ defined above. Across mesh edges, it is continuous in normal direction and discontinuous in tangential direction like the $\mathrm{RT}_0\mathrm{P}_0$ element. The matching pressure space is piecewise constant and discontinuous.

$\mathrm{Q}_2\mathrm{P}_1$ Element This element is based on a biquadratic approximation for velocity and a piecewise linear approximation for pressure. On the same mesh this element reaches higher accuracy at increased computational cost compared to the $\mathrm{Q}_1\mathrm{P}_0$ element. As for the other elements the pressure approximation may encounter discontinuities across mesh edges. This element is commonly used for discretization of the Stokes flow.

In what follows we use the abbreviation $\mathrm{Q}_1\mathrm{P}_0$ or $\mathrm{Q}_2\mathrm{P}_1$ for the FEM based on using either the $\mathrm{Q}_1\mathrm{P}_0$ or the $\mathrm{Q}_2\mathrm{P}_1$ element, respectively. On the other hand we use the abbreviation $\mathrm{RT}_0\mathrm{P}_0$ or $\mathrm{BDM}_1\mathrm{P}_0$ for the DG method based on using either the $\mathrm{RT}_0\mathrm{P}_0$ or the $\mathrm{BDM}_1\mathrm{P}_0$ element, respectively.

Function Spaces The finite element bases $\mathrm{Q}_1\mathrm{P}_0$ and $\mathrm{Q}_2\mathrm{P}_1$ yield well-known continuous finite element methods, see, e.g., [63, III.§6]. In what follows we define suitable discrete spaces $\boldsymbol{X}_h$, Q_h for the discretization of velocity and pressure, respectively, that will be used in the framework of the discontinuous Galerkin scheme.

$$\boldsymbol{X}_h = \{\boldsymbol{u} \in H_0(\mathrm{div}, \Omega) \,|\, \boldsymbol{u}|_E \in \mathrm{RT}_0(E) \text{ or } \mathrm{BDM}_1(E) \quad \forall E, \boldsymbol{u} \cdot \boldsymbol{n} = 0 \text{ on } \partial\Omega\}\,, \tag{2.4a}$$

$$Q_h = \left\{q \in L^2(\Omega) \,\middle|\, q|_E \in \mathrm{P}_0(E)\ \forall E,\ \textstyle\int_\Omega q = 0\right\}, \tag{2.4b}$$

$$H_0(\mathrm{div}, \Omega) = \left\{\boldsymbol{u} \in (L^2(\Omega))^2 \,\middle|\, \nabla \cdot \boldsymbol{u} \in L^2(\Omega), \boldsymbol{u} \cdot \boldsymbol{n} = 0 \text{ on } \partial\Omega\right\}. \tag{2.4c}$$

Thus, the approximation for the velocity is div-conforming, i.e., included in $H_0(\mathrm{div}, \Omega)$. It has continuous normal components across elements and it is globally divergence free in the space $H_0(\mathrm{div}, \Omega)$, cf. [60].

Scheme Derivation We now introduce notations for the jump and average of a (scalar or vector-valued) quantity $\boldsymbol{u} \in \mathbf{R}^n$, $n \geq 1$, along an edge $e = E_i \cap E_j$ shared by two neighbouring mesh elements E_i, E_j with the respective outer normal vectors $\boldsymbol{n}_i$ pointing to E_j, and $\boldsymbol{n}_j$ pointing to E_i,

$$[\boldsymbol{u}]_{ij} := \boldsymbol{u}_j - \boldsymbol{u}_i, \qquad \langle \boldsymbol{u} \rangle_{ij} := \frac{\boldsymbol{u}_i + \boldsymbol{u}_j}{2}, \tag{2.5}$$

where $\boldsymbol{u}_i$ denotes the limiting value of $\boldsymbol{u}$ from the mesh elements E_i along edge e. The analogous notation holds for $\boldsymbol{u}_j$. Fixing either of the normal vectors $\boldsymbol{n}_i$, $\boldsymbol{n}_j$ as belonging to the edge e, we drop the index notation for the jump since $\boldsymbol{n}_i = -\boldsymbol{n}_j$ and thus $[\boldsymbol{u}]_{ij}\boldsymbol{n}_j = [\boldsymbol{u}]_{ji}\boldsymbol{n}_i =: [\boldsymbol{u}]\,\boldsymbol{n}_e$. Consequently, we fix either of the normal vectors on interior edges and refer to it as $\boldsymbol{n}_e$. For boundary edges $e \subset \partial\Omega$ the notation $\boldsymbol{n}_e$ refers to the unique outward pointing normal. Secondly, we note without proof the following Lemma, cf. e.g., [64],

Lemma 2.1 *For $\boldsymbol{a}, \boldsymbol{b} \in \mathbf{R}^n$, $n \geq 1$, (or $\boldsymbol{a} \in \mathbf{R}$, $\boldsymbol{b} \in \mathbf{R}^n$, $n > 1$) the following equality applies:*

$$[\boldsymbol{a} \cdot \boldsymbol{b}] = \langle \boldsymbol{a} \rangle \cdot [\boldsymbol{b}] + [\boldsymbol{a}] \cdot \langle \boldsymbol{b} \rangle\,. \tag{2.6}$$

Now, we will derive our DG approximation following [42], [65, 4.2 and 6.2], [66, 14.2]. Note that the different approach of [55] yields similar forms. First, multiplying the momentum conservation equation (2.1a) with a test function $\boldsymbol{\phi} \in \boldsymbol{X}_h$ yields after elementwise integration by parts,

$$\int_E 2\mu\, \dot{\boldsymbol{\varepsilon}}(\boldsymbol{\phi}) : \dot{\boldsymbol{\varepsilon}}(\boldsymbol{v}) - \int_{\partial E} \boldsymbol{\phi} \cdot (\boldsymbol{\tau}\boldsymbol{n}_E) - \int_E p(\nabla \cdot \boldsymbol{\phi}) + \int_{\partial E} p\boldsymbol{\phi} \cdot \boldsymbol{n}_E = \int_E -\varrho g \hat{\boldsymbol{z}} \cdot \boldsymbol{\phi}, \tag{2.7}$$

where $\boldsymbol{n}_E$ denotes the unit outer normal of the mesh cell E and $\boldsymbol{a} : \boldsymbol{b}$ the so-called Frobenius product, i.e., componentwise inner product of two matrices.

Let us look in more details at the second term summed with respect to the mesh cells:

$$-\sum_{E\in\mathcal{T}_h}\int_{\partial E}\boldsymbol{\phi}\cdot(\boldsymbol{\tau}\boldsymbol{n}_E)=-\sum_{e\in\mathcal{F}_h}\int_e[\boldsymbol{\phi}\cdot\boldsymbol{\tau}]\,\boldsymbol{n}_e-\sum_{e\subset\partial\Omega}\int_e\boldsymbol{\phi}\cdot\boldsymbol{\tau}\boldsymbol{n}_e. \tag{2.8}$$

First, we would like to mention that the integrals along the boundary edges $e\subset\partial\Omega$ vanish due to the boundary conditions (2.3). Indeed, on Γ_2 the test function vanishes due to the Dirichlet boundary conditions. On Γ_1 we have $\sum_{e\subset\Gamma_1}\int_e\boldsymbol{\phi}\mu(\nabla\boldsymbol{v}+(\nabla\boldsymbol{v})^\mathsf{T})\boldsymbol{n}_e=\sum_{e\subset\Gamma_1}\int_e\boldsymbol{\phi}\mu(\nabla\boldsymbol{v})^\mathsf{T}\boldsymbol{n}_e$, since $\nabla\boldsymbol{v}\cdot\boldsymbol{n}_e=\partial v/\partial n_e=0$. Furthermore, we recall that Ω is a polygonal domain, thus on each boundary segment we have a constant outer normal. Applying both conditions from (2.3a) we finally obtain that $(\nabla\boldsymbol{v})^\mathsf{T}\boldsymbol{n}_e=(\sum_{j=1}^2\partial v_j/\partial x_1 n_{e,j},\sum_{j=1}^2\partial v_j/\partial x_2 n_{e,j})^\mathsf{T}=\boldsymbol{0}$ on Γ_1.

Further, we exploit Lemma 2.1 and, as argued in [66], we apply the interior penalty method. Thus, we replace the normal flux term, $\boldsymbol{\tau}\boldsymbol{n}$, by the discrete flux, $\langle 2\tilde{\mu}\dot{\boldsymbol{\varepsilon}}(\boldsymbol{v})\rangle\,\boldsymbol{n}_e-{}^{\sigma}/_{|e|}\,[\boldsymbol{v}]$, where σ is a suitable positive weight parameter, cf. also, e.g., [42, 4.6], [60]. In our numerical experiments presented in section 2.3 the parameter σ was chosen to be globally constant.

$$-\sum_{e\in\mathcal{F}_h}\int_e[\boldsymbol{\phi}\cdot\boldsymbol{\tau}]\,\boldsymbol{n}_e=-\sum_{e\in\mathcal{F}_h}\int_e[\boldsymbol{\phi}]\cdot\langle\boldsymbol{\tau}\rangle\,\boldsymbol{n}_e+\langle\boldsymbol{\phi}\rangle\cdot[\boldsymbol{\tau}]\,\boldsymbol{n}_e \tag{2.9}$$

$$=-\sum_{e\in\mathcal{F}_h}\int_e[\boldsymbol{\phi}]\cdot\boldsymbol{\tau}\boldsymbol{n}_e \tag{2.10}$$

$$\simeq-\sum_{e\in\mathcal{F}_h}\int_e[\boldsymbol{\phi}]\cdot\left(\langle 2\tilde{\mu}\dot{\boldsymbol{\varepsilon}}(\boldsymbol{v})\rangle\,\boldsymbol{n}_e-\frac{\sigma}{|e|}[\boldsymbol{v}]\right). \tag{2.11}$$

We have also used the fact that $\boldsymbol{\tau}\boldsymbol{n}_e$ is continuous across mesh edges for $\boldsymbol{v}$ being the exact solution, cf. [67]. Further, $\tilde{\mu}$ denotes an average viscosity value depending on the values of μ on the mesh cells that adhere to the respective edge e. We choose $\tilde{\mu}$ to be the geometric average accommodating the fact that μ may change by orders of magnitude. We note that, for the chosen benchmark setups, this yields smaller errors than taking the arithmetic or harmonic mean. For other ways of computing weighted averages in this context compare, e.g., [65, 4.5.2].

We note that the term $[\boldsymbol{v}]\cdot\langle 2\tilde{\mu}\dot{\boldsymbol{\varepsilon}}(\boldsymbol{\phi})\rangle$ is zero for $\boldsymbol{v}$ being the exact solution. Therefore, we could add it to (or subtract it from) the previous term without losing consistency. These considerations yield the following bilinear form a_h, which will be used for the numerical scheme,

$$
\begin{aligned}
a_h(\boldsymbol{v},\boldsymbol{\phi}) = \sum_E \int_E 2\mu\dot{\boldsymbol{\varepsilon}}(\boldsymbol{\phi}) : \dot{\boldsymbol{\varepsilon}}(\boldsymbol{v}) + \sum_{e\in\mathcal{F}_h} \frac{\sigma}{|e|} \int_e [\boldsymbol{\phi}] \cdot [\boldsymbol{v}] \\
- \sum_{e\in\mathcal{F}_h} \int_e [\boldsymbol{\phi}] \cdot \langle 2\mu\dot{\boldsymbol{\varepsilon}}(\boldsymbol{v})\rangle \boldsymbol{n}_e \\
- \epsilon \sum_{e\in\mathcal{F}_h} \int_e [\boldsymbol{v}] \cdot \langle 2\mu\dot{\boldsymbol{\varepsilon}}(\boldsymbol{\phi})\rangle \boldsymbol{n}_e, \quad \boldsymbol{v},\boldsymbol{\phi} \in \boldsymbol{X}_h.
\end{aligned} \tag{2.12}
$$

For $\epsilon = 1$, -1 , 0, this is referred to as the symmetric, nonsymmetric or incomplete interior penalty Galerkin method (SIPG, NIPG, IIPG), respectively. SIPG methods have been introduced in [64], NIPG in [68], IIPG in [69]. We refer also to other works, see, e.g., [52, 70–73] and the references therein, where full numerical analysis of the discontinous Galerkin method with SIP for the Laplace equation is available. For more details on the differences of these methods, we refer the reader to [74, 1.2], [65, 5.3] and the references therein. Numerical results presented in this paper were obtained using the NIPG ($\epsilon = -1$) that yielded best results for the considered benchmark problems.

The weak form of the incompressibility condition (2.1b) yields the bilinear form b_h and is given by:

$$
0 = b_h(\boldsymbol{v}, q) = \sum_E \int_E (\nabla \cdot \boldsymbol{v}) q, \quad q \in Q_h. \tag{2.13}
$$

To discretize the pressure terms from the momentum equation we extend the bilinear form b_h, cf. [65, 6.1],

$$
b_h^*(\boldsymbol{\phi}, p) = -b_h(\boldsymbol{\phi}, p) + \sum_{e\in\mathcal{F}_h} \int_e [p]\, \boldsymbol{\phi}\cdot\boldsymbol{n}_e + \sum_{e\subset\partial\Omega} \int_e p\boldsymbol{\phi}\cdot\boldsymbol{n}_e, \tag{2.14}
$$

where we used that $\boldsymbol{\phi}\cdot\boldsymbol{n}_e$ is continuous across mesh edges. Note again that the boundary integrals vanish due to eq. (2.3).

Now, we can state our DG approximation scheme: Find $(\boldsymbol{v}, p) \in \boldsymbol{X}_h \times Q_h$ such that

$$
a_h(\boldsymbol{v},\boldsymbol{\phi}) + b_h^*(\boldsymbol{\phi}, p) = \int_\Omega -\varrho g\hat{\boldsymbol{z}}\cdot\boldsymbol{\phi}, \quad \forall \boldsymbol{\phi} \in \boldsymbol{X}_h, \tag{2.15a}
$$

$$
b_h(\boldsymbol{v}, q) = 0, \qquad \forall q \in Q_h. \tag{2.15b}
$$

In [55] analytic properties of a large class of divergence-free DG methods have been investigated. The authors studied div-conforming spaces, which

satisfy the condition $\nabla \cdot X(E) \subseteq P(E)$, where $X(E)$ and $P(E)$ are local spaces for the approximation of velocity and pressure, respectively. Note that our local element $\mathrm{RT}_0\mathrm{P}_0$ satisfies the above condition. The use of the local space $\mathrm{BDM}_{k+1}\mathrm{P}_k$ for velocity and pressure, respectively, has been analyzed in [75] in the framework of DG FEM. For a large class of DG methods (including our particular choice (2.15)) stability and accuracy have been investigated theoretically in [55]. In particular, it has been proven that resulting methods satisfy the inf-sup stability condition and that the following error estimates hold.

Let us denote by $\boldsymbol{v}$, p, $\boldsymbol{v}_h$, p_h the exact and approximate solutions (velocity vector and pressure), respectively. Moreover let $\boldsymbol{v} \in H^{k+1}(\Omega)$, $p \in H^k(\Omega)$ a regular solution and $\|\cdot\|_{1,h}$ a suitable discrete H^1 norm in the broken Sobolev space $\boldsymbol{X}_h$, i.e., $\|\boldsymbol{u}_h\|_{1,h}^2 = \sum_E \int_E (\nabla \boldsymbol{u}_h)^2 \,\mathrm{d}x + \sum_e \int_e \frac{\sigma}{h} |[\boldsymbol{u}_h]|^2$ for any $\boldsymbol{u}_h \in \boldsymbol{X}_h$. Then it holds

$$\|\boldsymbol{v} - \boldsymbol{v}_h\|_{1,h} + \|p - p_h\|_{L^2(\Omega)} \leq c h^k \left(\|\boldsymbol{v}\|_{k+1} + \|p\|_k \right), \tag{2.16}$$

where $k \geq 1$, $c > 0$ is a constant independent of the mesh size h. Moreover, the approximate velocity $\boldsymbol{v}_h$ is exactly divergence-free and the resulting DG methods are conservative, energy-stable and optimally convergent, cf. [55] and [75].

Let us also point out that in [60] the author investigates the use of the $\mathrm{RT}_0\mathrm{P}_0$ element in the framework of divergence-free DG methods. It has been proven that such a DG scheme is algebraically equivalent to the standard MAC finite difference scheme, that is often used in engineering applications in order to approximate the Stokes problem. Using this fact, we can apply the recent result of Li and Sun [76] who have proven superconvergence of the MAC scheme, i.e., the discrete L^2 errors of pressure, velocity as well as gradient of velocity are of second order.

In this paper we compare the behaviour of the above DG methods and standard, i.e., continuous finite elements, for some typical geophysical tests. Recall that when we apply CG FEM method the space $\boldsymbol{X}_h$ is a discrete space approximating $(H^1(\Omega))^2$ with cellwise bilinear Q_1 or cellwise biquadratic functions Q_2. For the latter the pressure space Q_h is the space of cellwise *linear* functions with mean value zero. Thus, we do not require that the discrete velocities for CG FEM are div-conforming (i.e., in $H_0(\mathrm{div}, \Omega)$). Note that using the same bilinear forms without edge integrals the formulation above coincides with the standard variational formulation of incompressible Stokes flow in a CG FEM setting, see, e.g., [63, III.§6], [66, 12.2].

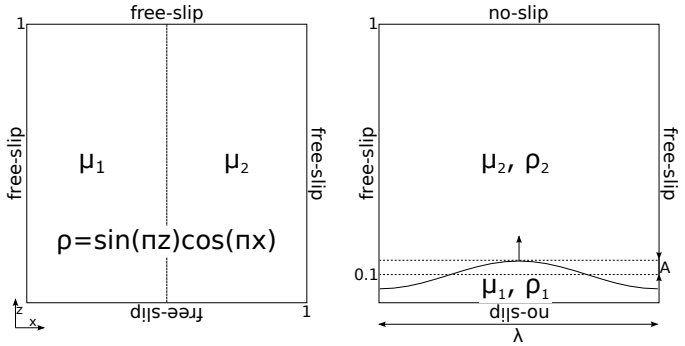

Figure 2.3: Benchmark setups SolCx (left) and Rayleigh-Taylor instability (right) with material viscosities μ_1, μ_2 and densities ϱ (SolCx setup), ϱ_1, ϱ_2 (Rayleigh-Taylor).

2.2.4 Benchmark Setups

SolCx Benchmark The analytic solution to this benchmark has been derived by Zhong [77] and our implementation follows [22]. We include a Matlab function (SolCx.m) to compute the analytic solution in the online supplement to this article that is based on the one provided in Underworld [33]. The setup resembles a simplified mantle convection model with a lateral viscosity jump caused by, e.g., a material interface. The flow is driven by a prescribed smooth density field.

Rayleigh-Taylor Instability This fluid-interface benchmark is used to test the velocity solution of gravity driven flows, see [12, 35, 78]. The boundary between the two fluids is perturbed by a sinusoidal perturbation of low, yet finite, amplitude A. By stretching the domain horizontally while keeping the relative shape of the perturbation we change its wavelength. This variation affects the maximal values for the vertical velocity at the interface. The analytic velocity solution is obtained for an infinitesimal amplitude and derived in detail in [78]. It is computed in a separate Matlab function (diapGrwth.m) in the online supplement to this article.

2.3 Numerical Experiments

In this section we describe the methodology for comparison of methods and discretizations for the above benchmarks and how to quantify computational costs of the different discretizations. All simulations using the RT_0P_0 element were done with $\sigma = 1$ while for all simulations using the BDM_1P_0 element σ was set to $\sigma = \frac{1}{h}$, where h denotes the edge length. This choice yielded the best results.

Note that the system was solved directly and that we did not investigate the performance of the method in larger scale simulations.

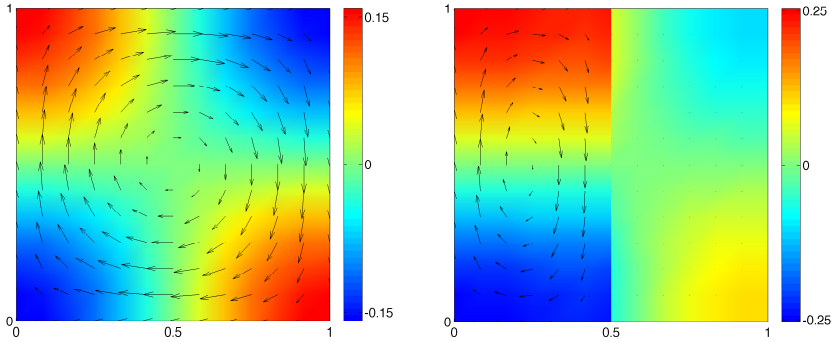

Figure 2.4: Analytic solution in SolCx benchmark as given by [77] for velocity (arrows) and pressure (color-coded). Left: Isoviscous setup, $\mu_1 = \mu_2 = 1$. Right: Viscosity jump of three orders of magnitude, $\mu_1 = 1$, $\mu_2 = 10^3$. The reference arrow lengths are 2.53×10^{-2} and 3.60×10^{-3}, respectively, for the arrow originating at the point $(x = 0, z = 0.5)$. Note that the pressure is discontinuous in the variable viscosity setup and the jump is aligned with the viscosity jump. The analytic solution for the isoviscous setup is $v = [-\sin(\pi x)\cos(\pi z); \cos(\pi x)\sin(\pi z)]/4\pi^2$, $p = -\cos(\pi x)\cos(\pi z)/2\pi$. The analytic solution of the variable-viscosity setup can be found in [77].

2.3.1 SolCx Benchmark

The flow in the SolCx Benchmark is driven by a prescribed density field $\varrho = -\sin(\pi z)\cos(\pi x)$ in the open domain $\Omega = (0,1) \times (0,1)$, the gravity $g = 1$ is normalized. The flow is subjected to free-slip boundary conditions as given in (2.3a), see Figure 2.3 (left).

Isoviscous Setup For the discretizations where the velocity is approximated with (bi-)linear basis functions (RT_0P_0, Q_1P_0, BDM_1P_0) we obtain second order convergence for the velocity measured in L^2 and H^1 norms. The L^2 error obtained with the RT_0P_0 element is slightly smaller than for Q_1P_0 and BDM_1P_0. Apparently, the RT_0P_0 element shows the superconvergence behavior mentioned in section 2.2.3, cf. [76]. The Q_1P_0 and BDM_1P_0 elements are on the same level. The higher order of the Q_2P_1 element yields fourth order convergence for the velocity measured in the L^2 norm. As the cross derivatives $\partial_x v_z$, $\partial_z v_x$ vanish locally for the RT_0P_0 element, it does not converge with respect to the H^1 norm and, hence, its plot is omitted. The other three elements yield H^1 errors on about the same level (BDM_1P_0 smallest, Q_2P_1 largest).

The L^2 pressure error differs only slightly for the RT_0P_0 and the Q_2P_1 element as well as for the Q_1P_0 and the BDM_1P_0 element. For the latter ones it is at least two orders of magnitude smaller and has higher rate of convergence, which seems to be influenced by superconvergence effects for this particular setup.

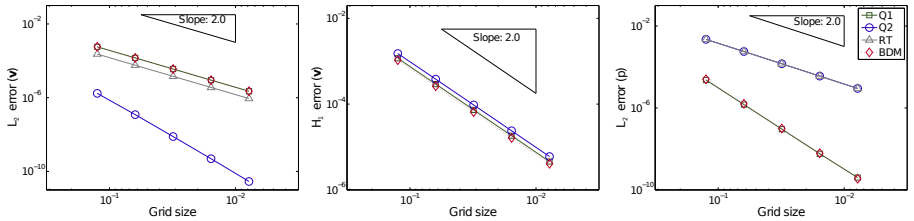

Figure 2.5: Isoviscous SolCx Benchmark: L^2 (left) and H^1 (center) errors for velocity and L^2 error for pressure (right) for the four discretizations Q_1P_0, Q_2P_1, RT_0P_0 and BDM_1P_0. The slope of the plots corresponds to the order of convergence towards the analytic solution when increasing the mesh resolution, i.e., decreasing the grid size.

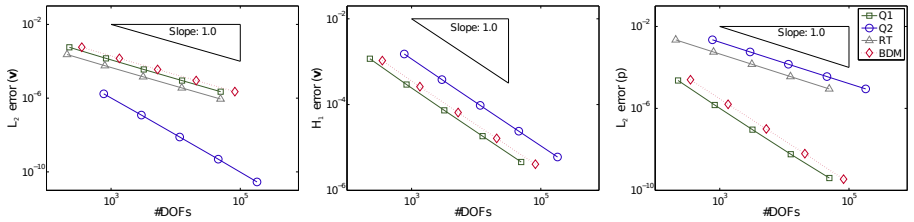

Figure 2.6: Isoviscous SolCx Benchmark: L^2 (left) and H^1 (center) errors for velocity and L^2 error for pressure (right) for the four discretizations Q_1P_0, Q_2P_1, RT_0P_0 and BDM_1P_0. The slope of the plots corresponds to the order of convergence towards the analytic solution when increasing the number of degrees of freedom.

Let us consider the errors with respect to the number of degrees of freedom (DOFs) needed to reach a certain accuracy. The Q_2P_1 element still yields the smallest velocity error in the L^2 norm. On the other hand, the Q_1P_0 element performs slightly better than the BDM_1P_0 element (and a lot better than the Q_2P_1 element) in terms of the H^1 error in the velocity and the pressure error.

For the velocity and pressure error in the isoviscous SolCx setup see Figures 2.5 and 2.6.

Lateral Viscosity Jump In this setup the velocity errors show a similar behavior as for the isoviscous case, i.e., the BDM_1P_0 and Q_1P_0 element converge with second order to the analytic solution with the error being at the same order of magnitude, while the Q_2P_1 element converges with fourth order and, therefore, reaches much higher accuracy at the same resolution. For the BDM_1P_0 element the convergence order measured in the H^1 norm is only 1.3, approximately, while the two conforming elements keep the order 2. The pressure errors for these three elements are of similar order and converge with second order.

Considering the number of degrees of freedom the elements' performance is similar to the isoviscous case. The Q_2P_1 element yields the best L^2 error for

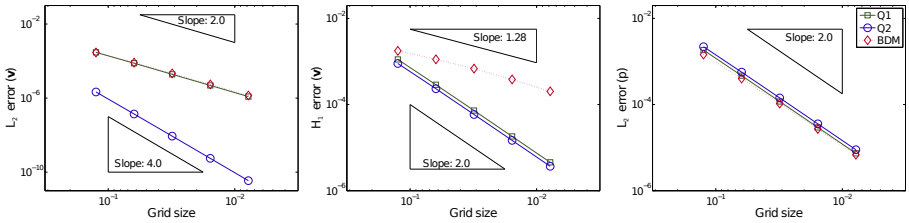

Figure 2.7: Variable Viscosity SolCx Benchmark: L^2 (left) and H^1 (center) errors for velocity and L^2 error for pressure (right) for the three discretizations Q_1P_0, Q_2P_1 and BDM_1P_0. The slope of the plots corresponds to the order of convergence towards the analytic solution when increasing the mesh resolution, i.e., decreasing the grid size.

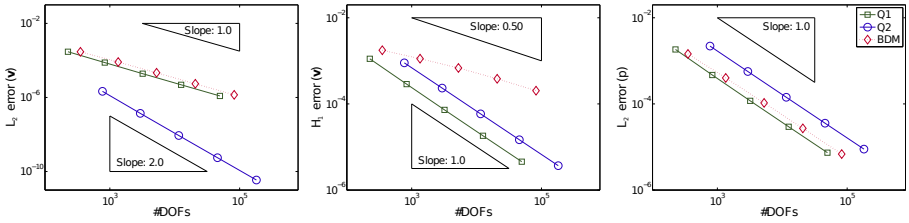

Figure 2.8: Variable Viscosity SolCx Benchmark: L^2 (left) and H^1 (center) errors for velocity and L^2 error for pressure (right) for the three discretizations Q_1P_0, Q_2P_1 and BDM_1P_0. The slope of the plots corresponds to the order of convergence towards the analytic solution when increasing the number of degrees of freedom.

the velocity while the Q_1P_0 element yields highest accuracy in terms of the H^1 error for the velocity and L^2 error for the pressure. For the velocity and pressure error in the SolCx setup with discontinuous viscosity see Figures 2.7 and 2.8.

We omit the RT_0P_0 element for this setup as it does not converge to the analytic solution. Due to the simple structure of this element no coupling of the two velocity components can be captured in the numerical scheme given in section 2.2.3. As the cross derivatives $\partial_x v_z$, $\partial_z v_x$ vanish element-wise, shear stress components are not taken into account in the discrete scheme. Shear stress is zero in the isoviscous SolCx setup but non-zero for discontinuous viscosity. This explains why the RT_0P_0 element converges in the isoviscous case but not in the discontinuous viscosity case. We aim to further investigate this problem in a future study.

We can deduce from Figures 2.5 and 2.7 that the BDM_1P_0 element has about the same accuracy (in terms of the L^2 errors) as the Q_1P_0 element for any fixed resolution. This is to be expected as both elements are of the same order, i.e. velocity is approximated with piecewise bilinear, pressure is approximated with piecewise constant shape functions. The RT_0P_0 element is computation-

ally cheaper, yielding similar accuracy in simple setups like the isoviscous SolCx setup but fails for setups with non-zero shear stress. The Q_2P_1 element, being of higher order, yields higher accuracy and higher order of convergence at the price of increased computational costs.

While the Q_1P_0 and Q_2P_1 element keep the L^2 order of convergence for the velocity when changing to the H^1 norm, the convergence order of the BDM_1P_0 element decreases.

2.3.2 Rayleigh-Taylor Instability

In the Rayleigh-Taylor instability benchmark the flow is driven by the density difference $\Delta\varrho = \varrho_2 - \varrho_1$ of the two material layers. Both, the density difference $\Delta\varrho = 1$ and the gravity $g = 1$ are normalized. The computational domain is set to be $\Omega = (0, \lambda) \times (0, z_{\max})$, where $z_{\max} = 1$, see Figure 2.3 (right). The material interface follows a mesh edge with a sinusoidal perturbation of amplitude A and wavelength λ, i.e., the elements adjacent to the perturbed edge are slightly deformed. Hence, the mesh is *not* globally regular anymore. We vary the viscosity contrast $10^{-3} \leq \mu_2/\mu_1 \leq 10^3$ and study the vertical velocity v_z at the tip of the sinusoidal perturbation. The magnitude of this velocity also depends on the wavelength λ, i.e., for every viscosity contrast there is one dominant wavelength λ^* that yields a maximal magnitude for the vertical velocity in this location. We vary the wavelength λ in a certain range around the dominant wavelength λ^*_{exp} that we determined experimentally, see the axis labels in Figure 2.9 for the ranges of $\phi = 2\pi(z_{\max} - z_{\text{jump}})/\lambda$, $z_{\max} = 1$, $z_{\text{jump}} = 0.1$.

In this setup, the free-slip condition is imposed at the vertical boundaries, no-slip at the horizontal boundaries, see (2.3). We run two sets of experiments. Firstly, we fix the resolution to 50 by 50 elements. Secondly, we choose the resolution such that for all elements it yields approximately the same number of non-zero entries in the system matrix. In both cases we compute the maximum vertical velocity v_z for different wavelengths λ of the sinusoidal perturbation by changing the width of the domain and we vary the viscosity contrasts between 10^{-3} and 10^3, fixing the perturbation amplitude at $A = 10^{-4}$. A non-dimensional growth factor $K_{\text{an}} = \frac{v_z}{A} \frac{2\mu_2}{\Delta\varrho\, z_{\text{jump}} g}$ can be analytically derived as given in [78, sec. 6] and [12, sec. 16.2]. We compare the numerically retrieved value of K to the analytic one. For the same reasons as in the previous section we omit the RT_0P_0 element here.

We shall first consider the case $\mu_2/\mu_1 \leq 1$, i.e., the top layer viscosity being less or equal to the bottom layer viscosity, with fixed resolution of 50 by 50 elements, see Figure 2.9, bottom left. The Q_2P_1 element, as in all other cases, very accurately resembles the analytic value of the maximum vertical velocity

Table 2.1: Relative errors $e_{\text{rel}} = \left|\frac{K-K_{\text{an}}}{K_{\text{an}}}\right|$ for the three elements at $\phi(\lambda^*_{\text{exp}})$ in the middle of the chosen range. Resolution for all elements fixed at 50 by 50 elements.

	$e_{\text{rel}}(\lambda^*_{\text{exp}})$		
μ_2/μ_1	Q_1P_0	Q_2P_1	BDM_1P_0
10^3	4.9×10^{-1}	1.5×10^{-3}	5.0×10^{-1}
10^1	2.8×10^{-1}	1.4×10^{-3}	2.6×10^{-1}
10^0	6.0×10^{-2}	8.4×10^{-4}	1.0×10^{-1}
10^{-3}	2.7×10^{-1}	3.6×10^{-4}	3.7×10^{-1}

Table 2.2: Relative errors $e_{\text{rel}} = \left|\frac{K-K_{\text{an}}}{K_{\text{an}}}\right|$ for the three elements at $\phi(\lambda^*_{\text{exp}})$ in the middle of the chosen range. Resolution for Q_1P_0, Q_2P_1, BDM_1P_0 element is 90 by 90, 40 by 40, 60 by 60 elements, respectively, yielding approximately the same memory usage for all three elements ($\approx 4.5 \times 10^5$ non-zero entries in system matrix).

	$e_{\text{rel}}(\lambda^*_{\text{exp}})$		
μ_2/μ_1	Q_1P_0	Q_2P_1	BDM_1P_0
10^3	1.6×10^{-1}	2.4×10^{-3}	3.5×10^{-1}
10^1	9.7×10^{-2}	2.5×10^{-3}	1.8×10^{-1}
10^0	1.6×10^{-2}	1.6×10^{-3}	7.7×10^{-2}
10^{-3}	9.0×10^{-2}	7.5×10^{-4}	2.6×10^{-1}

Table 2.3: Number of global degrees of freedom (DOFs) and of non-zero entries (NNZs) in the system matrix on a square 32-by-32-mesh for the four discretizations. Note that the Q_1P_0 and Q_2P_1 elements are used in the standard finite element framework while the RT_0P_0 and the BDM_1P_0 elements are used in the DG scheme derived in section 2.2.3.

Element	DOFs	NNZs
RT_0P_0	3136	2.6×10^4
Q_1P_0	3202	4.8×10^4
BDM_1P_0	5248	1.2×10^5
Q_2P_1	11 522	3.1×10^5

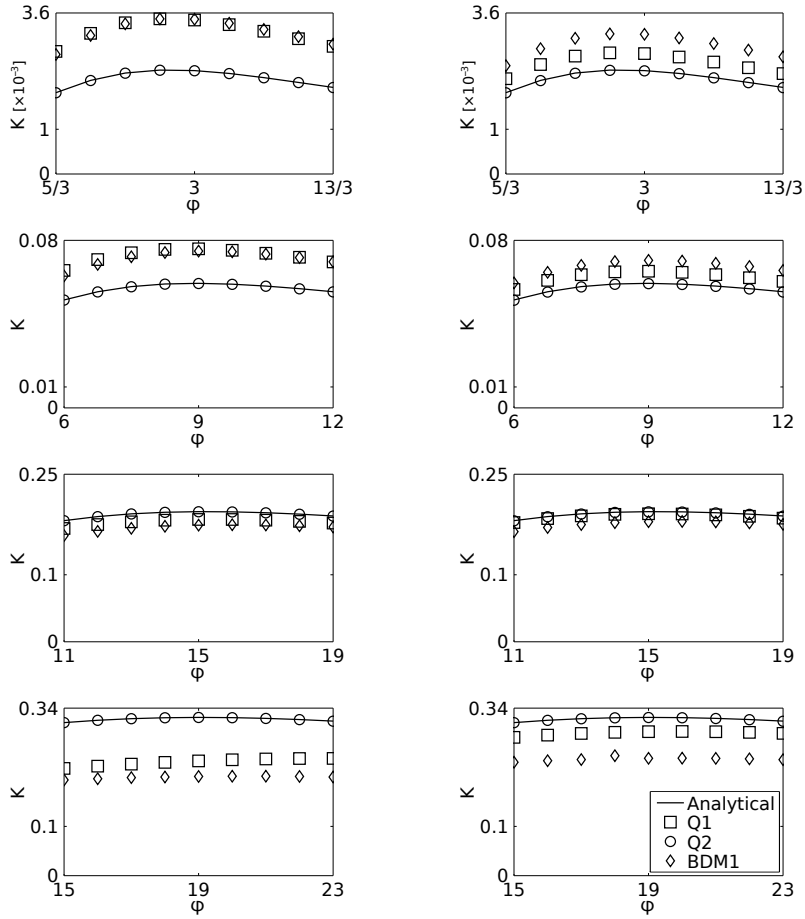

Figure 2.9: Rayleigh-Taylor Instability Benchmark: Non-dimensional growth factor K versus frequency $\phi = 2\pi(z_{\max} - z_{\text{jump}})/\lambda$, $z_{\max} = 1$, $z_{\text{jump}} = 0.1$. Solid lines give the analytically obtained value K_{an} at the tip of the sinusoidal perturbation (i.e., where vertical velocity is maximal). Top to bottom: Viscosity contrasts $\mu_2/\mu_1 = 10^3, 10^1, 10^0, 10^{-3}$. Left: Errors for Q_1P_0, Q_2P_1, BDM_1P_0 at fixed mesh resolution of 50 by 50. Right: Errors for Q_1P_0(mesh resolution 90 by 90), Q_2P_1(40 by 40), BDM_1P_0 (60 by 60), i.e., such that the system matrix has approximately 4.5×10^5 non-zero entries.

while the Q_1P_0 and the BDM_1P_0 elements deviate stronger, see Table 2.1. Yet, the relative errors for the latter two stay in the same range.

For the same viscosity contrasts, but roughly equivalent memory usage of all three elements (Figure 2.9, bottom right), the Q_2P_1 element is still the best choice. The relative error for the Q_1P_0 element is less than half of the error for the BDM_1P_0 element, see Table 2.2.

In the case $\mu_2/\mu_1 > 1$, i.e. the top layer being more viscous than the bottom layer, the BDM_1P_0 element yields a better approximation to the maximum vertical velocity than the Q_1P_0 element. Still, the Q_2P_1 element gives much higher accuracy, see Figure 2.9, top left, and Table 2.1. For equivalent memory usage (Figure 2.9, top right, Table 2.2), this behavior changes partially. For some wavelengths at viscosity contrast $\mu_2/\mu_1 = 10^3$ the BDM_1P_0 element yields a smaller error, for others the Q_1P_0 element does. For $\mu_2/\mu_1 = 10^1$ the Q_1P_0 error, all in all, is smaller than the error obtained with the BDM_1P_0 element.

Similar to the SolCx benchmark, using the Q_2P_1 element in the Rayleigh-Taylor instability benchmark, see Figure 2.9, we obtain very accurate approximations for any considered viscosity contrast. On the one hand, we can see the BDM_1P_0 and Q_1P_0 elements yielding an error of equal order of magnitude for the bottom layer viscosity being greater or equal to the top layer viscosity ($\mu_1 \geq \mu_2$). On the other hand, when the top layer viscosity exceeds the bottom layer viscosity, the BDM_1P_0 element yields better results than the Q_1P_0 element.

2.3.3 Computational Costs

Finally, we list the number of entries in the system matrix for the different discretizations as an indicator for computational costs of the solution and how much memory its assembly requires, see Table 2.3. It can be observed that the RT_0P_0 element is the cheapest one considered here. However, its drawbacks are obvious, as it fails to converge in relevant variable viscosity benchmark setups.

If one considers memory usage instead of mesh resolution one obtains different observations. For a fixed memory the Q_1P_0 element gives a higher accuracy than the BDM_1P_0 element that seemed to be competitive when fixing the mesh resolution, cf. Figures 2.6, 2.8.

In any case, regarding fixed memory limitations or fixed resolution, the Q_2P_1 element has best over-all performance.

2.4 Conclusions

The main aim of this paper was to study the behaviour of the DG finite element method based on using div-conforming elements to approximate Stokes flow with variable viscosity and examine how it compares in terms of accuracy and memory usage to the standard CG finite element method for some typical geodynamic benchmark setups. In the DG scheme we use the Raviart-Thomas (RT_0P_0) and the Brezzi-Douglas-Marini element (BDM_1P_0). In contrast to the Q_1P_0 finite element they fulfill the LBB stability condition, implying that they are more reliable.

We showed that the overall results are as accurate or more accurate than the ones obtained with the Q_1P_0 element in a standard finite element scheme considering a fixed mesh resolution. Yet, the Q_1P_0 CG method yields better results than the DG method using the BDM_1P_0 element when considering a fixed memory limitation. Secondly, being of first order both of them are computationally less expensive than the Q_2P_1 element. However, whenever a second-order FEM like Q_2P_1 is computationally feasible, higher accuracy can be obtained compared to the DG method based on the BDM_1P_0 element or the Q_1P_0 element in the classical FEM scheme.

The divergence-conforming property of the BDM_1P_0 and the RT_0P_0 element has been seen to be advantageous for, e.g., Navier-Stokes equations [55] or Darcy flow [56]. However, in the tested benchmark setups this does not produce noticeable benefits. We would like to investigate this point in our future study on different test cases.

The BDM_1P_0 element yields good results in all tested setups and offers an alternative to the LBB-unstable Q_1P_0 element. The setups presented in this article do not lead to common instabilities of the Q_1P_0 element. However, we want to point out that for the Stokes flow the reliability of the BDM_1P_0 element is its major advantage when being compared to the Q_1P_0 element. This could well be taken as justification to deploy this discretization.

Due to the flexibility of *hp*-refinement within the DG methods, it is possible to apply low order discretizations in the vicinity of viscosity jumps, but higher order polynomials in the areas with constant or smoothly varying viscosity. This might be a promising future direction for complex geodynamic simulations.

Acknowledgement This work has been funded and supported by the Computational Sciences Center and by the Max Planck Graduate Center with the Johannes Gutenberg-Universität Mainz (MPGC).

The deployed Matlab code is provided as an electronic supplement with the article web resource.

References

[1] P. A. Allen and J. R. Allen. *Basin Analysis: Principles and Applications*. Wiley-Blackwell, 2nd edition, 2005. ISBN 978-0-632-05207-3.

[2] C. J. Warren, C. Beaumont, and R. A. Jamieson. Modelling tectonic styles and ultra-high pressure (UHP) rock exhumation during the transition from oceanic subduction to continental collision. *Earth and Planetary Science Letters*, 267(1–2):129–145, 2008. DOI:10.1016/j.epsl.2007.11.025.

[3] B. J. P. Kaus, C. Steedman, and T. W. Becker. From passive continental margin to mountain belt: Insights from analytical and numerical models and application to Taiwan. *Physics of the Earth and Planetary Interiors*, 171(1–4):235–251, 2008. DOI:10.1016/j.pepi.2008.06.015.

[4] S. M. Lechmann, S. M. Schmalholz, G. Hetényi, D. A. May, and B. J. P. Kaus. Quantifying the impact of mechanical layering and underthrusting on the dynamics of the modern India-Asia collisional system with 3-D numerical models. *Journal of Geophysical Research: Solid Earth*, 119(1):616–644, 2014. DOI:10.1002/2012JB009748.

[5] L. Moresi, P. G. Betts, M. S. Miller, and R. A. Cayley. Dynamics of continental accretion. *Nature*, 508:245–248, 2014. DOI:10.1038/nature13033.

[6] F. Crameri, H. Schmeling, G. J. Golabek, T. Duretz, R. Orendt, S. J. H. Buiter, D. A. May, B. J. P. Kaus, T. V. Gerya, and P. J. Tackley. A comparison of numerical surface topography calculations in geodynamic modelling: An evaluation of the 'sticky air' method. *Geophysical Journal International*, 189(1):38–54, 2012. DOI:10.1111/j.1365-246X.2012.05388.x.

[7] G. Schubert, D. L. Turcotte, and P. Olson. *Mantle Convection in the Earth and Planets*. Cambridge University Press, 2001. ISBN 978-0-521-79836-5.

[8] Y. Deubelbeiss, B. J. P. Kaus, J. A. D. Connolly, and L. Caricchi. Potential causes for the non-Newtonian rheology of crystal-bearing magmas. *Geochemistry, Geophysics, Geosystems*, 12(5), 2011. DOI:10.1029/2010GC003485.

[9] T. Keller, D. A. May, and B. J. P. Kaus. Numerical modelling of magma dynamics coupled to tectonic deformation of lithosphere and crust. *Geophysical Journal International*, 195(3): 1406–1442, 2013. DOI:10.1093/gji/ggt306.

[10] T. E. Johnson, M. Brown, B. J. P. Kaus, and J. A. van Tongeren. Delamination and recycling of Archaean crust caused by gravitational instabilities. *Nature Geoscience*, 7(1):47–52, 2014. DOI:10.1038/ngeo2019.

[11] D. L. Turcotte and G. Schubert. *Geodynamics*. Cambridge University Press, 2nd edition, 2002. ISBN 978-0-521-66624-4.

[12] T. V. Gerya. *Introduction to Numerical Geodynamic Modelling*. Cambridge University Press, 2010. ISBN 978-0-521-88754-0.

[13] A. Ismail-Zadeh and P. Tackley. *Computational Methods for Geodynamics*. Cambridge University Press, 2010. ISBN 978-0-521-86767-2.

[14] T. W. Becker and B. J. P. Kaus. Numerical Geodynamics – An introduction to computational methods with focus on solid Earth applications of continuum mechanics, 2010. URL http://geodynamics.usc.edu/%7Ebecker/preprints/Geodynamics540.pdf.

[15] B. J. P. Kaus, H.-B. Mühlhaus, and D. A. May. A stabilization algorithm for geodynamic numerical simulations with a free surface. *Physics of the Earth and Planetary Interiors*, 181 (1–2):12–20, 2010. DOI:10.1016/j.pepi.2010.04.007.

[16] P. J. Tackley. Modelling compressible mantle convection with large viscosity contrasts in a three-dimensional spherical shell using the yin-yang grid. *Physics of the Earth and Planetary Interiors*, 171(1–4):7–18, 2008. DOI:10.1016/j.pepi.2008.08.005.

[17] M. Thielmann and B. J. P. Kaus. Shear heating induced lithospheric-scale localization: Does it result in subduction? *Earth and Planetary Science Letters*, 359–360:1–13, 2012. DOI:10.1016/j.epsl.2012.10.002.

[18] Y. Deubelbeiss and B. J. P. Kaus. Comparison of Eulerian and Lagrangian numerical techniques for the Stokes equations in the presence of strongly varying viscosity. *Physics of the Earth and Planetary Interiors*, 171(1–4):92–111, 2008. DOI:10.1016/j.pepi.2008.06.023.

[19] M. Thielmann, D. A. May, and B. J. P. Kaus. Discretization Errors in the Hybrid Finite Element Particle-in-cell Method. *Pure and Applied Geophysics*, 171(9):2165–2184, 2014. ISSN 0033-4553. DOI:10.1007/s00024-014-0808-9.

[20] P. J. Tackley. Effects of strongly temperature-dependent viscosity on time-dependent, three-dimensional models of mantle convection. *Geophysical Research Letters*, 20(20):2187–2190, 1993. DOI:10.1029/93GL02317.

[21] T. V. Gerya and D. A. Yuen. Characteristics-based marker-in-cell method with conservative finite-differences schemes for modeling geological flows with strongly variable transport properties. *Physics of the Earth and Planetary Interiors*, 140(4):293–318, 2003. DOI:10.1016/j.pepi.2003.09.006.

[22] D. A. May and L. Moresi. Preconditioned Iterative Methods for Stokes Flow Problems Arising in Computational Geodynamics. *Physics of the Earth and Planetary Interiors*, 171(1–4):33–47, 2008. DOI:10.1016/j.pepi.2008.07.036.

[23] T. Duretz, D. A. May, T. V. Gerya, and P. J. Tackley. Discretization errors and free surface stabilization in the finite difference and marker-in-cell method for applied geodynamics: A numerical study. *Geochemistry, Geophysics, Geosystems*, 12(7):1200–1225, 2011. ISSN 1525-2027. DOI:10.1029/2011GC003567.

[24] C. Hüttig and K. Stemmer. Finite volume discretization for dynamic viscosities on Voronoi grids. *Physics of the Earth and Planetary Interiors*, 171(1–4):137–146, 2008. DOI:10.1016/j.pepi.2008.07.007.

[25] S. A. Melchior, V. Legat, P. van Dooren, and A. J. Wathen. Analysis of preconditioned iterative solvers for incompressible flow problems. *International Journal for Numerical Methods in Fluids*, 68(3):269–286, 2012. DOI:10.1002/fld.2505.

[26] M. Benzi, G. H. Golub, and J. Liesen. Numerical solution of saddle point problems. *Acta Numerica*, 14:1–137, 2005. DOI:10.1017/S0962492904000212.

[27] C. Burstedde, O. Ghattas, M. Gurnis, G. Stadler, E. Tan, T. Tu, L. C. Wilcox, and S. Zhong. Scalable adaptive mantle convection simulation on petascale supercomputers. In *Proceedings of the 2008 ACM/IEEE Conference on Supercomputing*, SC '08, pages 62:1–62:15, Piscataway, NJ, USA, 2008. IEEE Press. ISBN 978-1-4244-2835-9. DOI:10.1109/SC.2008.5214248.

[28] C. Burstedde, G. Stadler, L. Alisic, L. C. Wilcox, E. Tan, M. Gurnis, and O. Ghattas. Large-scale adaptive mantle convection simulation. *Geophysical Journal International*, 192(3):889–906, 2013. DOI:10.1093/gji/ggs070.

[29] M. Furuichi, D. A. May, and P. J. Tackley. Development of a Stokes flow solver robust to large viscosity jumps using a Schur complement approach with mixed precision arithmetic. *Journal of Computational Physics*, 230(24):8835–8851, 2011. DOI:10.1016/j.jcp.2011.09.007.

[30] B. E. Griffith. An accurate and efficient method for the incompressible Navier-Stokes equations using the projection method as a preconditioner. *Journal of Computational Physics*, 228 (20):7565–7595, 2009. DOI:10.1016/j.jcp.2009.07.001.

[31] M. Cai, A. J. Nonaka, J. B. Bell, B. E. Griffith, and A. Donev. Efficient Variable-Coefficient Finite-Volume Stokes Solvers. *arXiv Numerical Analysis (math.NA)*, 1308.4605, 2013. URL http://arxiv.org/abs/1308.4605v2.

[32] S. Zhong. Constraints on thermochemical convection of the mantle from plume heat flux, plume excess temperature, and upper mantle temperature. *Journal of Geophysical Research: Solid Earth*, 111(B4), 2006. DOI:10.1029/2005JB003972.

[33] L. Moresi, S. Quenette, V. Lemiale, C. Mériaux, B. Appelbe, and H.-B. Mühlhaus. Computational approaches to studying non-linear dynamics of the crust and mantle. *Physics of the Earth and Planetary Interiors*, 163(1–4):69–82, 2007. DOI:10.1016/j.pepi.2007.06.009.

[34] M. Dabrowski, M. Krotkiewski, and D. W. Schmid. MILAMIN: MATLAB-based finite element method solver for large problems. *Geochemistry, Geophysics, Geosystems*, 9(4), 2008. ISSN 1525-2027. DOI:10.1029/2007GC001719.

[35] A. A. Popov and S. V. Sobolev. SLIM3D: A Tool for Three-dimensional Thermomechanical Modeling of Lithospheric Deformation with Elasto-visco-plastic Rheology. *Physics of the Earth and Planetary Interiors*, 171(1–4):55–75, 2008. DOI:10.1016/j.pepi.2008.03.007.

[36] Yury Mishin. *Adaptive multiresolution methods for problems of computational geodynamics*. PhD thesis, ETH Zürich, 2011.

[37] D. A. May, J. Brown, and L. Le Pourhiet. pTatin3D: High-Performance Methods for Long-Term Lithospheric Dynamics. In *SC14: International Conference for High Performance Computing, Networking, Storage and Analysis*, pages 274–284, 2014. ISBN 978-1-4799-5500-8. DOI:10.1109/SC.2014.28.

[38] L. C. Wilcox, G. Stadler, C. Burstedde, and O. Ghattas. A high-order discontinuous Galerkin method for wave propagation through coupled elastic-acoustic media. *Journal of Computational Physics*, 229(24):9373–9396, 2010. DOI:10.1016/j.jcp.2010.09.008.

[39] C. R. Dohrmann and P. B. Bochev. A stabilized finite element method for the Stokes problem based on polynomial pressure projections. *International Journal for Numerical Methods in Fluids*, 46(2):183–201, 2004. DOI:10.1002/fld.752.

[40] P. Bochev, C. Dohrmann, and M. Gunzburger. Stabilization of Low-order Mixed Finite Elements for the Stokes Equations. *SIAM Journal on Numerical Analysis*, 44(1):82–101, 2006. DOI:10.1137/S0036142905444482.

[41] C. Burstedde, O. Ghattas, G. Stadler, T. Tu, and L. C. Wilcox. Parallel scalable adjoint-based adaptive solution of variable-viscosity Stokes flow problems. *Computer Methods in Applied Mechanics and Engineering*, 198(21–26):1691–1700, 2009. DOI:10.1016/j.cma.2008.12.015.

[42] M. Feistauer, J. Felcman, and I. Straškraba. *Mathematical and Computational Methods for Compressible Flow*. Oxford University Press, 2003. ISBN 978-0-198-50588-4.

[43] B. Cockburn and C. Shu. The Local Discontinuous Galerkin Method for Time-Dependent Convection-Diffusion Systems. *SIAM Journal on Numerical Analysis*, 35(6):2440–2463, 1998. DOI:10.1137/S0036142997316712.

[44] M. J. Guillot, B. Rivière, and M. F. Wheeler. Discontinuous Galerkin methods for mass conservation equations for environmental modelling. In S. M. Hassanizadeh, R. J. Schotting, W. G. Gray, and G. F. Pinder, editors, *Computational Methods in Water Resources, Developments in Water Science*, volume 47, pages 939–946. Elsevier, 2002. ISBN 978-0-444-50975-8.

[45] M. Feistauer and V. Kučera. On a Robust Discontinuous Galerkin Technique for the Solution of Compressible Flow. *Journal of Computational Physics*, 224(1):208–221, 2007. DOI:10.1016/j.jcp.2007.01.035.

[46] J. Aarnes and B.-O. Heimsung. Multiscale Discontinuous Galerkin Methods for Elliptic Problems with Multiple Scales. In B. Engquist, P. Lötstedt, and O. Runborg, editors, *Multiscale Methods in Science and Engineering*, volume 44 of *Lecture Notes in Computational Science and Engineering*, pages 1–20. Springer, 2005. ISBN 978-3-540-26444-6. DOI:10.1007/3-540-26444-2_1.

[47] N. K. Burgess and D. J. Mavriplis. *hp*-Adaptive Discontinuous Galerkin Solver for the Navier-Stokes Equations. *AIAA J.*, 50(12):2682–2694, 2012. DOI:10.2514/1.J051340.

[48] S. Giani. High-order/*hp*-adaptive discontinuous Galerkin finite element methods for acoustic problems. *Computing*, 95(1):215–234, 2013. DOI:10.1007/s00607-012-0253-5.

[49] A. Baggag, H. Atkins, and D. Keyes. Parallel Implementation of the Discontinuous Galerkin Method. Technical report, Institute for Computer Applications in Science and Engineering (ICASE), 1999.

[50] H. Luo, L. Luo, A. Ali, R. Nourgaliev, and C. Cai. A Parallel, Reconstructed Discontinuous Galerkin Method for the Compressible Flows on Arbitrary Grids. *Communications in Computational Physics*, 9(2):363–389, 2011. DOI:10.2514/6.2010-366.

[51] B. Cockburn, G. E. Karniadakis, and C. W. Shu, editors. *Discontinuous Galerkin Methods: Theory, Computation, and Applications*, volume 11 of *Lecture Notes in Computational Science and Engineering*. Springer, 2000. ISBN 978-3-540-66787-2.

[52] D. N. Arnold, F. Brezzi, B. Cockburn, and L. D. Marini. Unified Analysis of Discontinuous Galerkin Methods for Elliptic Problems. *SIAM Journal on Numerical Analysis*, 39(5):1749–1779, 2002. DOI:10.1137/S0036142901384162.

[53] V. Etienne, E. Chaljub, J. Virieux, and N. Glinsky. An *hp*-adaptive discontinuous Galerkin finite-element method for 3-D elastic wave modelling. *Geophysical Journal International*, 183 (2):941–962, 2010. DOI:10.1111/j.1365-246X.2010.04764.x.

[54] D. Pageot, S. Operto, M. Vallée, R. Brossier, and J. Virieux. A parametric analysis of two-dimensional elastic full waveform inversion of teleseismic data for lithospheric imaging. *Geophysical Journal International*, 193(3):1479–1505, 2013. DOI:10.1093/gji/ggs132.

[55] B. Cockburn, G. Kanschat, and D. Schötzau. A Note on Discontinuous Galerkin Divergence-free Solutions of the Navier-Stokes Equations. *Journal of Scientific Computing*, 31(1–2):61–73, 2007. DOI:10.1007/s10915-006-9107-7.

[56] V. J. Ervin. Computational bases for RT_k and BDM_k on triangles. *Computers & Mathematics with Applications*, 64(8):2765–2774, 2012. DOI:10.1016/j.camwa.2012.08.011.

[57] Z. Cai and S. Zhang. Mixed methods for stationary Navier-Stokes equations based on pseudostress-pressure-velocity formulation. *Mathematics of Computation*, 81(280):1903–1927, 2012. DOI:10.1090/S0025-5718-2012-02585-3.

[58] D. Griffiths and D. Silvester. Unstable modes of the Q1-P0 element. MIMS EPrint 2011.44, Manchester Institute for Mathematical Sciences, University of Manchester, Manchester, UK, 2011. This item originally appeared as MCCM Report 257 in 1994.

[59] P. Raviart and J. Thomas. A Mixed Finite Element Method for 2-nd Order Elliptic Problems. In I. Galligani and E. Magenes, editors, *Mathematical Aspects of Finite Element Methods*, volume 606 of *Lecture Notes in Mathematics*, chapter 19, pages 292–315. Springer, 1977. ISBN 978-3-540-08432-7. DOI:10.1007/bfb0064470.

[60] G. Kanschat. Divergence-free Discontinuous Galerkin Schemes for the Stokes Equations and the MAC Scheme. *International Journal for Numerical Methods in Fluids*, 56(7):941–950, 2008. DOI:10.1002/fld.1566.

[61] F. Brezzi, J. Douglas, Jr., and L. D. Marini. Two Families of Mixed Finite Elements for Second Order Elliptic Problems. *Numerische Mathematik*, 47(2):217–235, 1985. DOI:10.1007/BF01389710.

[62] F. Brezzi and M. Fortin. *Mixed and Hybrid Finite Element Methods*. Springer, New York, NY, USA, 1991. ISBN 978-3-540-97582-3.

[63] D. Braess. *Finite elements: Theory, fast solvers, and applications in solid mechanics*. Cambridge University Press, 3rd edition, 2007. ISBN 978-0-521-70518-9. DOI:10.1017/CBO9780511618635.

[64] M. F. Wheeler. An Elliptic Collocation-Finite Element Method with Interior Penalties. *SIAM Journal on Numerical Analysis*, 15(1):152–161, 1978. DOI:10.1137/0715010.

[65] D. A. Di Pietro and A. Ern. *Mathematical Aspects of Discontinuous Galerkin Methods*, volume 69 of *Mathématiques et Applications*. Springer, Berlin, 2012. ISBN 978-3-642-22980-0.

[66] M. Larson and F. Bengzon. *The Finite Element Method: Theory, Implementation and Applications*. Springer, 2013. ISBN 978-3-642-33286-9.

[67] J. Nečas. *Direct Methods in the Theory of Elliptic Equations*. Springer, 2nd edition, 2012. ISBN 978-3-642-10455-8.

[68] J. T. Oden, I. Babuška, and C. E. Baumann. A Discontinuous *hp* Finite Element Method for Diffusion Problems. *Journal of Computational Physics*, 146(2):491–519, 1998. DOI:10.1006/jcph.1998.6032.

[69] C. Dawson, S. Sun, and M. F. Wheeler. Compatible algorithms for coupled flow and transport. *Computer Methods in Applied Mechanics and Engineering*, 193(23–26):2565–2580, 2004. DOI:10.1016/j.cma.2003.12.059.

[70] D. N. Arnold. An interior penalty finite element method with discontinuous elements. *SIAM Journal on Numerical Analysis*, 19(4):742–760, 1982. DOI:10.1137/0719052.

[71] B. Rivière, M. F. Wheeler, and V. Girault. Improved energy estimates for interior penalty, constrained and discontinuous Galerkin methods for elliptic problems. Part I. *Computational Geosciences*, 3(3-4):337–360, 1999. DOI:10.1023/A:1011591328604.

[72] F. Brezzi, G. Manzini, D. Marini, P. Pietra, and A. Russo. Discontinuous Galerkin approximations for elliptic problems. *Numerical Methods for Partial Differential Equations*, 16(4):365–378, 2000. DOI:10.1002/1098-2426(200007)16:4<365::AID-NUM2>3.0.CO;2-Y.

[73] Z. Chen and H. Chen. Pointwise Error Estimates of Discontinuous Galerkin Methods with Penalty for Second-Order Elliptic Problems. *SIAM Journal on Numerical Analysis*, 42(3):1146–1166, 2004. DOI:10.1137/S0036142903421527.

[74] B. Rivière. *Discontinuous Galerkin Methods For Solving Elliptic And Parabolic Equations: Theory and Implementation*. Society for Industrial and Applied Mathematics, Philadelphia, PA, USA, 2008. ISBN 978-0-898-71656-6.

[75] B. Cockburn, G. Kanschat, and D. Schötzau. A locally conservative LDG method for the incompressible Navier-Stokes equations. *Mathematics of Computation*, 74(251):1067–1095, 2005. DOI:10.1090/S0025-5718-04-01718-1.

[76] J. Li and S. Sun. The Superconvergence Phenomenon and Proof of the MAC Scheme for the Stokes Equations on Non-uniform Rectangular Meshes. *Journal of Scientific Computing*, pages 1–22, 2014. DOI:10.1007/s10915-014-9963-5.

[77] S. Zhong. Analytic Solutions for Stokes' Flow with Lateral Variations in Viscosity. *Geophysical Journal International*, 124(1):18–28, 1996. DOI:10.1111/j.1365-246X.1996.tb06349.x.

[78] H. Ramberg. Instability of Layered Systems in the Field of Gravity. *Physics of the Earth and Planetary Interiors*, 1(7):427–447, 1968. DOI:10.1016/0031-9201(68)90014-9.

CHAPTER 3

Coupling Stokes and Darcy Flow in Melt Migration Modelling

3.1 Introduction

On the one hand, Stokes flow is a flow regime where advective inertial forces are negligible compared to viscous forces. It is considered to describe slowly creeping motion in settings of, e.g., tectonic deformation and it is, therefore, *the* major regime being considered in the young field of geodynamic numerical modelling. On the other hand, the propagation of partially molten material in a crystallized host rock is described best as flow in porous media, i.e., following Darcy's law.

In the geodynamics context Darcy flow has been considered, particularly, in modelling groundwater flow [1–3]. Numerically more advanced methods have been presented, using, e.g., a stabilized mixed finite element approach [4–6], (stabilized) discontinuous Galerkin methods [7–10], coupled mixed finite elements and a discontinuous Galerkin method [11], pressure projection stabilization [12], or the novel weak Galerkin finite element method [13].

The need to solve systems of coupled (Navier-)Stokes and Darcy flow arises in fields of applications as different as studying permeability in carbonate reservoirs [14], modelling the interaction of surface water (rivers) and groundwater (aquifers) [15, 16], blood flow problems [17, 18], or fuel cell dynamics [19, 20]. Consequently, there has been a lot of active research in finding stable, robust and accurate numerical methods.

There are generally two ways of coupling the two flow regimes. The Stokes-Darcy-Brinkman approach merges the flow regimes into a single momentum

equation that reduces to the end-member cases Stokes or Darcy flow for suitable coefficients [14, 20–23]. The second approach is known as Robin-Robin domain decomposition and enforces either the Stokes or Darcy equations locally on subdomains, coupled with appropriate interface conditions [24, 25]. There are two major classes of numerical methods for this system: iteratively solving the Stokes and Darcy problem separately [24, 26], or solving a monolithic system in a single step, see below. Approaches similar to the latter one have also been investigated for coupled *Navier*-Stokes/Darcy problems [17, 27–29].

In the class of monolithic methods the coupled Stokes/Darcy system has for example been tackled with continuous finite elements [15, 30–33]. As these lead to unbalanced rates of convergence for the two subproblems different approaches were presented, such as the combination of mixed finite elements (for Darcy region) and a discontinuous Galerkin method (for Stokes region) [34–36], or a reformulation of discretized Darcy flow combined with arbitrary stable Galerkin finite element methods for Stokes flow [37]. Egger and Waluga [38] presented a hybridized discontinuous Galerkin method that is capable of solving the Stokes equations, the Darcy equations or the coupled problem in a unified manner. An adaptive continuous-discontinuous Galerkin method is presented in [39].

In melt migration modelling the partially molten rock as second (fluid) phase cannot easily be handled in the presented approaches. Also, we fail to identify obvious boundaries of where to apply one or the other flow regime. In his work on the generation and compaction of partially molten rock McKenzie [40] incorporated Darcy's law into the standard conservation equations and included a model of a compacting solid matrix. Since then, most models of melt migration in the last 30 years have been following this path. Based on this, and on others' work on two-phase flow, e.g., [41–44], Bercovici et al. [45] derived model equations for the dynamics of a two-phase mixture.

Recently, Keller et al. [46] reformulated this model in the context of melt migration on the lithospheric scale advancing it in multiple ways: they introduced visco-elasto-plastic rheologies to the system via appropriate constitutive equations, presented it as an extension to the well understood Stokes flow the way it is implemented in many geodynamic numerical modelling softwares, and formulated it symmetrically such that discretizations lead to symmetric matrices that are faster to solve for. In particular, they derived the so-called three-field formulation referring to the major unknowns solid velocity, fluid pressure and compaction pressure, which proved to be superior to previous formulations, especially in terms of numerical stability when being discretized [47].

We build upon the work of Keller et al., repeat and describe in detail their mathematical model in section 3.2, and derive a stable and robust numerical method in a mathematically thorough manner in section 3.3. Section 3.4 is dedicated to a small series of numerical experiments to investigate the convergence order of the proposed method and prove validity for important deformational regimes. Finally, we discuss the results in section 3.5 and draw conclusions about the work and its possible future implications in section 3.6.

3.2 Governing Equations

In this section we present the equations for the conservation of momentum and mass as they are known for incompressible Stokes flow. This system is substantiated by Darcy flow to capture the physics of a coupled lithosphere and magma dynamics system. We recap the derivation of the rheological constitutive equations presented in [46] to arrive at the full system of governing equations in section 3.2.4. At the end of this section we describe other physical material properties, see section 3.2.5.

3.2.1 Notation

First, we introduce some notation to handle the two phases present in the considered system. Crystallized (host rock) material is referred to as the solid phase and melt material is referred to as the fluid phase with its properties being denoted with subscripts s and f, respectively. The porosity φ is defined as the volume melt fraction of the two-phase mixture. Porosity-averaged properties a are denoted as $\bar{a} := (1-\varphi)a_s + \varphi a_f$, the difference is denoted as $\Delta a := a_s - a_f$, not to be confused with the Laplacian operator that we do not use in this work.

3.2.2 Conservation Equations

Conservation of Mass The equations for conservation of (fluid and solid) mass are given by, see, e.g., [40, 45],

$$\frac{\partial \varphi}{\partial t} + \nabla \cdot (\varphi \boldsymbol{v}_f) = 0, \tag{3.1a}$$

$$\frac{\partial (1-\varphi)}{\partial t} + \nabla \cdot ((1-\varphi)\boldsymbol{v}_s) = 0, \tag{3.1b}$$

where φ, t, $\boldsymbol{v}$ denote porosity, time and velocity, respectively. Adding them up yields the total mass conservation equation,

$$\nabla \cdot \bar{\boldsymbol{v}} = 0. \tag{3.2}$$

Introducing the solid material derivative $\mathrm{D_s}/\mathrm{D}t := \partial/\partial t + \boldsymbol{v}_\mathrm{s} \cdot \nabla$ and the phase separation flux $\boldsymbol{q} := -K_D \left(\nabla p_\mathrm{f} + \varrho_\mathrm{f} \boldsymbol{g}\right)$, that can be interpreted as a porosity-weighted velocity difference $\boldsymbol{q} = -\varphi \Delta \boldsymbol{v}$, we can rewrite the equations (3.1) and (3.2), cp. [40, 46, 47],

$$-\nabla \cdot \boldsymbol{v}_\mathrm{s} + K_D \nabla p_\mathrm{f} = -\nabla \cdot K_D \varrho_\mathrm{f} \boldsymbol{g}, \tag{3.3a}$$

$$\frac{\mathrm{D_s}\varphi}{\mathrm{D}t} - (1-\varphi)\nabla \cdot \boldsymbol{v}_\mathrm{s} = 0, \tag{3.3b}$$

where the Darcy coefficient $K_D := \kappa_\varphi / \eta_\mathrm{f}$ is defined as the permeability to fluid viscosity ratio. Note that the fluid velocity $\boldsymbol{v}_\mathrm{f}$ is no longer explicitly included in this system. Numerically, it is to be recovered from the phase separation flux in a post-processing step.

Conservation of Momentum For slowly creeping viscous flow inertial terms are negligible and, therefore, the equation for conservation of (total) momentum is given by,

$$-\nabla \cdot \bar{\boldsymbol{\tau}} + \nabla \bar{p} = -\bar{\varrho} \boldsymbol{g}, \tag{3.4}$$

where $\boldsymbol{\tau}$, p, ϱ, $\boldsymbol{g}$, denote deviatoric stress, pressure, density and gravitational acceleration, respectively. Deviatoric stress $\boldsymbol{\tau}$ and density ϱ are functions of the material composition c, see below. Note that there is no explicit time-dependence in the momentum equation. However, as deviatoric stress $\bar{\boldsymbol{\tau}}$ and bulk density $\bar{\varrho}$ depend on the porosity φ, they implicitly inherit its time-dependence.

Splitting the total pressure p into fluid pressure p_f and compaction pressure $p_\mathrm{c} := \bar{p} - p_\mathrm{f}$, we can rewrite equation (3.4), cp. [46, 47],

$$-\nabla \cdot \bar{\boldsymbol{\tau}} + \nabla p_\mathrm{f} + \nabla p_\mathrm{c} = -\bar{\varrho} \boldsymbol{g}, \tag{3.5}$$

Material Evolution The evolution of the material composition c in Eulerian frame of reference is given as [48–50],

$$\frac{\mathrm{D_s} c}{\mathrm{D}t} = 0, \tag{3.6}$$

where c represents the (lithologic) material phase. The Lagrangian form of this equation can be written as follows, denoting the advection of phase c in location $\boldsymbol{x}$,

$$\frac{\mathrm{d}\boldsymbol{x}}{\mathrm{d}t} = \boldsymbol{v}_\mathrm{s}, \qquad \frac{\mathrm{d}c}{\mathrm{d}t} = 0. \tag{3.7}$$

SUMMARY We summarize the equations (3.3), (3.5), (3.6) (in Eulerian form). The full system of governing equations is given in section 3.2.4, p. 42f.,

$$-\nabla \cdot \bar{\boldsymbol{\tau}} + \nabla p_\mathrm{f} + \nabla p_\mathrm{c} = -\bar{\varrho}\boldsymbol{g}, \tag{3.8a}$$

$$-\nabla \cdot \boldsymbol{v}_\mathrm{s} + K_D \nabla p_\mathrm{f} = -\nabla \cdot K_D \varrho_\mathrm{f} \boldsymbol{g}, \tag{3.8b}$$

$$\frac{\mathrm{D}_\mathrm{s}\varphi}{\mathrm{D}t} - (1-\varphi)\nabla \cdot \boldsymbol{v}_\mathrm{s} = 0, \tag{3.8c}$$

$$\frac{\mathrm{D}_\mathrm{s}c}{\mathrm{D}t} = 0. \tag{3.8d}$$

The system (3.8) is closed by constitutive relations for the deviatoric stress and for the compaction pressure,

$$\bar{\boldsymbol{\tau}} = f(\dot{\boldsymbol{\varepsilon}}'_\mathrm{s}), \qquad p_\mathrm{c} = f(\dot{v}_\mathrm{s}), \tag{3.9}$$

as described in section 3.2.3. Here, $\dot{\boldsymbol{\varepsilon}}'_\mathrm{s}$ and $\dot{v}_\mathrm{s}$ denote deviatoric and volumetric strain rates of the solid phase, respectively. The strain rate tensor is defined as

$$\dot{\boldsymbol{\varepsilon}}_\mathrm{s} = \tfrac{1}{2}\left(\nabla \boldsymbol{v}_\mathrm{s} + (\nabla \boldsymbol{v}_\mathrm{s})^\mathsf{T}\right). \tag{3.10}$$

We define the volumetric strain rate $\dot{v}_\mathrm{s} := \mathrm{tr}(\dot{\boldsymbol{\varepsilon}}_\mathrm{s}) = \nabla \cdot \boldsymbol{v}_\mathrm{s}$ as the trace of the strain rate tensor, and the deviatoric strain rate $\dot{\boldsymbol{\varepsilon}}'_\mathrm{s} := \dot{\boldsymbol{\varepsilon}}_\mathrm{s} - \frac{1}{3}\dot{v}_\mathrm{s}\boldsymbol{I}_d$ as the difference of the total strain rate and its volumetric part.

3.2.3 Constitutive Equations and Rheology

We consider visco-elasto-plastic rheologies that are to be captured in constitutive equations (3.9). For a more detailed derivation we refer to [46].

ELASTICITY Shear elasticity of the solid phase is modelled as a Maxwell body with the following visco-elastic deviatoric strain rate tensor

$$\dot{\boldsymbol{\varepsilon}}'_{\mathrm{s,ve}} = \frac{1}{2\eta}\boldsymbol{\tau}_\mathrm{s} + \frac{1}{2G}\frac{\widetilde{\mathrm{D}}_\mathrm{s}\boldsymbol{\tau}_\mathrm{s}}{\mathrm{D}t}, \tag{3.11}$$

where η and G denote shear viscosity and elastic shear modulus, respectively, and $\widetilde{\mathrm{D}}_\mathrm{s}/\mathrm{D}t$ denotes the Jaumann objective derivative to account for stress rotation, see [51, sec. 10.7.4], [52, 53],

$$\frac{\widetilde{\mathrm{D}}_\mathrm{s}\boldsymbol{\tau}_\mathrm{s}}{\mathrm{D}t} = \frac{\partial \boldsymbol{\tau}_\mathrm{s}}{\partial t} + \boldsymbol{v}_\mathrm{s} \cdot \nabla \boldsymbol{\tau}_\mathrm{s} - \boldsymbol{\omega}\boldsymbol{\tau}_\mathrm{s} + \boldsymbol{\tau}_\mathrm{s}\boldsymbol{\omega}, \tag{3.12}$$

where $\boldsymbol{\omega} = \frac{1}{2}\left(\nabla \boldsymbol{v}_\mathrm{s} - \nabla \boldsymbol{v}_\mathrm{s}^\mathrm{T}\right)$ denotes the vorticity tensor. The advection term in (3.12) is dropped here as advection is handled explicitly on Lagrangian markers in the method that we present below.

Integrating (3.11) in time yields a representation of the deviatoric stress $\boldsymbol{\tau}_\mathrm{s}$ in terms of the visco-elastic solid deviatoric strain rate $\dot{\boldsymbol{\varepsilon}}'_{\mathrm{s,ve}}$. In this way a time integral term arises in the system. For simplification we assume a discrete implicit first-order representation of the objective derivative as follows,

$$\frac{\widetilde{\mathrm{D}}_\mathrm{s}\boldsymbol{\tau}_\mathrm{s}}{\mathrm{D}t} \approx \frac{\boldsymbol{\tau}_\mathrm{s} - \tilde{\boldsymbol{\tau}}_\mathrm{s}^o}{\Delta t}, \tag{3.13}$$

with $\tilde{\boldsymbol{\tau}}_\mathrm{s}^o := \boldsymbol{\tau}_\mathrm{s}^o + \Delta t(\boldsymbol{\omega}\boldsymbol{\tau}_\mathrm{s}^o - \boldsymbol{\tau}_\mathrm{s}^o\boldsymbol{\omega})$ the rotated deviatoric stress tensor from the previous time step. Now we can rewrite (3.11) in terms of the deviatoric stress as follows,

$$\boldsymbol{\tau}_\mathrm{s} = \frac{2}{\frac{1}{\eta} + \frac{1}{G\Delta t}}\dot{\boldsymbol{\varepsilon}}'_{\mathrm{s,ve}} + \frac{1}{1 + \frac{G\Delta t}{\eta}}\tilde{\boldsymbol{\tau}}_\mathrm{s}^o. \tag{3.14}$$

By defining the effective viscoelasticity η_ve and the elastic stress evolution parameter χ_τ,

$$\eta_\mathrm{ve} = \frac{1-\varphi}{\frac{1}{\eta} + \frac{1}{G\Delta t}}, \qquad \chi_\tau = \frac{1-\varphi}{1 + \frac{G\Delta t}{\eta}}, \tag{3.15}$$

we can summarize the constitutive equation for the deviatoric stress tensor $\bar{\boldsymbol{\tau}}$ (neglecting fluid deviatoric stresses) as

$$\bar{\boldsymbol{\tau}} \approx (1-\varphi)\boldsymbol{\tau}_\mathrm{s} = 2\eta_\mathrm{ve}\dot{\boldsymbol{\varepsilon}}'_{\mathrm{s,ve}} + \chi_\tau\tilde{\boldsymbol{\tau}}_\mathrm{s}^o. \tag{3.16}$$

Note that η is defined below in equation (3.32).

Analogously, for decompaction we arrive at

$$p_\mathrm{c} = -\zeta_\mathrm{ve}\dot{v}_{\mathrm{s,ve}} + \chi_p\Delta p^o, \tag{3.17}$$

where ζ_ve denotes the viscoelastic compaction viscosity, Δp^o contains historical compaction pressure data and

$$\zeta_\mathrm{ve} = \frac{1-\varphi}{\frac{1}{\zeta} + \frac{1}{K_\varphi\Delta t}}, \qquad \chi_p = \frac{1-\varphi}{1 + \frac{K_\varphi\Delta t}{\zeta}}, \tag{3.18}$$

introducing the elastic pore modulus K_φ.

PLASTICITY Following Terzaghi's principle of effective stress [54] we introduce the effective pressure p_{eff},

$$p_{\text{eff}} := \bar{p} - \chi_\varphi p_{\text{f}}, \quad \chi_\varphi \in \{0, 1\}, \tag{3.19}$$

where χ_φ is the characteristic function indicating whether or not a significant amount of fluid phase ($\varphi \geq \varphi_{\text{crit}}$) is present, hence,

$$p_{\text{eff}} = \begin{cases} \bar{p}, & 0 \leq \varphi \leq \varphi_{\text{crit}} \\ p_{\text{c}}, & \varphi \geq \varphi_{\text{crit}}. \end{cases} \tag{3.20}$$

We apply two different criteria to obtain a failure envelope for the pressure-stress state in the model. First, the Drucker-Prager criterion for shear failure, see [55], and, second, the Griffith-Murrell criterion for tensile failure that may occur when effective pressure is negative, see [56]. Both criteria define a joint failure envelope in the $(p_{\text{eff}}, \boldsymbol{\tau}_{\text{II}})$ plane as follows,

$$\bar{\boldsymbol{\tau}}_{\text{II}} \leq \tau_y = \begin{cases} C\cos(\phi) + p_{\text{eff}}\sin(\phi), & p_{\text{eff}} \geq {p_{\text{eff}}}^*, \\ p_{\text{eff}} + \sigma_T, & p_{\text{eff}} < {p_{\text{eff}}}^*, \end{cases} \tag{3.21}$$

where the subscript $\bar{\boldsymbol{\tau}}_{\text{II}} = \sqrt{\frac{1}{2}\bar{\boldsymbol{\tau}}_{ij}\bar{\boldsymbol{\tau}}_{ij}}$ denotes the square root of the second invariant of shear stress, τ_y the yield stress, C cohesion, ϕ friction angle and $\sigma_T = C/R$, $R \in [2, 8]$, the tensile strength of the rock, [57]. Analogously, the effective pressure is limited by the yield pressure $p_{\text{eff}} \geq p_y = \bar{\boldsymbol{\tau}}_{\text{II}} - \sigma_T$.

The implementation is based on an effective viscosity approach, i.e., effective viscosities η_{eff}, ζ_{eff} are iteratively chosen such that the stress state $(p_{\text{eff}}, \bar{\boldsymbol{\tau}}_{\text{II}})$ is kept on the yield surface (p_y, τ_y), see [52, 58].

We rewrite a scalar version of equation (3.16) including plastic deformation in the strain rate,

$$\tau_y = 2\eta_{\text{eff}}\dot{\boldsymbol{\varepsilon}}'_{\text{s,II}} + \chi_\tau \tilde{\boldsymbol{\tau}}^o_{\text{s,II}}, \tag{3.22}$$

which applies in the case of plastic failure. This yields the effective shear viscosity η_{eff},

$$\eta_{\text{eff}} = \begin{cases} \frac{\tau_y - \chi_\tau \tilde{\boldsymbol{\tau}}^o_{\text{s,II}}}{2\dot{\boldsymbol{\varepsilon}}_{\text{s,II}}}, & \bar{\boldsymbol{\tau}}_{\text{II}} = \tau_y, \\ \eta_{\text{ve}}, & \bar{\boldsymbol{\tau}}_{\text{II}} < \tau_y. \end{cases} \tag{3.23}$$

Analogously, we arrive at the equation for yield pressure p_y by rewriting equation (3.17) including plastic deformation in the volumetric strain rate $\dot{v}_s$,

$$p_y = -\zeta_{\text{eff}}\, \dot{v}_s + \chi_p \Delta p^o. \tag{3.24}$$

This can be rewritten in terms of effective compaction viscosity ζ_{eff},

$$\zeta_{\text{eff}} = \begin{cases} -\frac{p_y - \chi_p \Delta p^o}{\dot{v}_s}, & p_c = p_y, \\ \zeta_{ve}, & p_c > p_y. \end{cases} \tag{3.25}$$

Hence, the visco-elasto-plastic constitutive equations for shear stress and compaction pressure are the following,

$$\bar{\boldsymbol{\tau}} = 2\eta_{\text{eff}}\, \dot{\boldsymbol{\varepsilon}}'_s + \chi_\tau \tilde{\boldsymbol{\tau}}^o_{s,\text{II}}, \tag{3.26a}$$

$$p_c = -\zeta_{\text{eff}}\, \dot{v}_s + \chi_p \Delta p^o. \tag{3.26b}$$

3.2.4 Governing Equations

In what follows we consider a bounded and connected domain $\Omega \subset \mathbf{R}^d$, $d \in \{2, 3\}$, with a Lipschitz continuous boundary $\partial\Omega$. By adding (3.26b) to the system (3.8), we arrive at the following system of equations that we consider as the combination of a quasi-static fluid flow problem with the unknowns solid velocity $\boldsymbol{v}_s$, fluid pressure p_f and compaction pressure p_c (3.27), the porosity evolution equation (3.28), and the material advection (3.29). Remember that $\bar{\boldsymbol{\tau}} \equiv \boldsymbol{\tau}_s(\boldsymbol{v}_s, \varphi, \eta_{\text{eff}}, \ldots)$.

$$-\nabla \cdot \bar{\boldsymbol{\tau}} + \nabla p_f + \nabla p_c = -\bar{\varrho}\boldsymbol{g} \tag{3.27a}$$

$$-\nabla \cdot \boldsymbol{v}_s + \nabla \cdot K_D \nabla p_f = -\nabla \cdot K_D \varrho_f \boldsymbol{g} \tag{3.27b}$$

$$-\nabla \cdot \boldsymbol{v}_s - \frac{p_c}{\zeta_{\text{eff}}} = -\frac{\chi_p \Delta p^o}{\zeta_{\text{eff}}}, \tag{3.27c}$$

$$\frac{\mathrm{D}_s \varphi}{\mathrm{D}t} - (1 - \varphi)\nabla \cdot \boldsymbol{v}_s = 0, \tag{3.28}$$

$$\frac{\mathrm{D}_s c}{\mathrm{d}t} = 0. \tag{3.29}$$

The system is closed by the constitutive equations (3.26a), (3.23) and (3.25) for deviatoric stress $\bar{\boldsymbol{\tau}}$, effective shear viscosity η_{eff} and effective compaction viscosity ζ_{eff}, respectively. It is complemented by an initial condition for the porosity $\varphi(t_0) = \varphi_0$ and the material composition $c(t_0) = c_0$, and the following boundary conditions, see [47].

Let the boundary $\partial\Omega = \Gamma_D \cup \Gamma_N$, where $\Gamma_D \cap \Gamma_N = \emptyset$, and denote the outward unit normal vector on $\partial\Omega$ as $\boldsymbol{n}$,

$$\boldsymbol{v}_\mathrm{s} = \boldsymbol{b}_D \qquad \text{on } \Gamma_D, \tag{3.30a}$$

$$\boldsymbol{\tau}_\mathrm{s}\boldsymbol{n} - (p_\mathrm{f} + p_\mathrm{c})\,\boldsymbol{n} = \boldsymbol{b}_N \qquad \text{on } \Gamma_N, \tag{3.30b}$$

$$-K_D(\nabla p_\mathrm{f} + \varrho_\mathrm{f}\boldsymbol{g}) \cdot \boldsymbol{n} = 0 \qquad \text{on } \partial\Omega, \tag{3.30c}$$

where $\boldsymbol{b}_D : \Gamma_D \to \mathbf{R}^d$, $\boldsymbol{b}_N : \Gamma_N \to \mathbf{R}^d$ are given boundary data.

In the case of $\partial\Omega = \Gamma_D$ the boundary data $\boldsymbol{b}_D$ is required to comply with the compatibility condition,

$$\int_{\partial\Omega} \boldsymbol{b}_D \,\mathrm{d}s = 0, \tag{3.31}$$

which implies $\int_\Omega p_\mathrm{c}/\zeta_\mathrm{eff} \,\mathrm{d}x = 0$.

A tuple $(\boldsymbol{v}, p_\mathrm{f}, p_\mathrm{c}) \in \left(C^2(\mathrm{cl}(\Omega))\right)^d \times C^2(\mathrm{cl}(\Omega)) \times C^1(\mathrm{cl}(\Omega))$ fulfilling the equations (3.27) and (3.30) is called a classical solution to the coupled two-phase and Stokes problem, where $\mathrm{cl}(\cdot)$ denotes the closure of a set and C^k denotes the space of functions with k continuous derivatives. In what follows, we refer to (3.27) as the three-field system, see [47].

In the limit case of zero porosity φ the system reduces to the well-known Stokes system with the fluid pressure p_f taking the role of the total pressure and the compaction pressure p_c vanishing.

3.2.5 Material Properties

Completing the system above we describe in this section how the initial shear and compaction viscosities, fluid viscosity, permeability, density, cohesion, friction angle, tensile strength, and the elastic moduli are determined.

The viscous shear viscosity η that enters (3.15) is the product of an assumed intrinsic shear viscosity of the rock η_0 and an exponential melt-weakening factor. This has been examined experimentally, e.g., [59], theoretically [60, 61] and numerically [62–64],

$$\eta = \eta_0 \exp(-\alpha\varphi). \tag{3.32}$$

In the numerical experiments performed in section 3.4, the reference shear viscosity η_0 varies from 10^{18} to 10^{25} Pa s. In chapter 4 we determine the shear viscosity η from experimentally constrained viscous creep laws.

The compaction viscosity is proportional to the reference shear viscosity and inversely proportional to the porosity, see [61, 65],

$$\zeta = r_\zeta \eta_0 \varphi^{-1}, \tag{3.33}$$

where r_ζ is a constant of proportionality of order 1. In the numerical experiments presented in section 3.4 we set $r_\zeta = 1$.

Throughout this chapter, the fluid viscosity η_f is assumed to be constant, $\eta_f = 10^2$ Pa s. This corresponds to a low-viscosity basaltic melt [66, 67], see also [63, 68].

Permeability follows a power-law as described in [46], see also [69, 70],

$$\kappa_\varphi = \kappa_0 (1-\varphi)^2 \varphi^3. \tag{3.34}$$

Density is constant per phase, i.e., we set solid and fluid density ϱ_s, ϱ_f, and compute their porosity-based average $\bar{\varrho}$ on the integration points for the system matrix assembly.

Plasticity parameters such as the cohesion C, the friction angle ϕ and the tensile strength σ_T are constant for each simulation. The tensile strength is varied by choosing a reduction parameter for the resistance of the host rock to fail under tensile stress, $\sigma_T = C/R$, $R \in \{2, 4, 8\}$. Throughout this chapter, we set $R = 2$.

The shear modulus G is chosen to be constant. The pore modulus K_φ varies with porosity in consistency with previous studies [71, 72],

$$K_\varphi = K_0 \varphi^{-\frac{1}{2}}, \tag{3.35}$$

where the reference pore modulus K_0 varies mostly in the range 1 to 100 GPa.

3.3 Numerical Method and Implementation

In this section we present the weak form of the three-field system (3.27) (in contrast to the two-field system presented in, e.g., [47, 73]). We define the finite element spaces that we use for the simulations and we outline the algorithmic implementation of the method.

Let us first introduce the required function spaces. The standard notation $L^p(\cdot)$, $H_0^k(\cdot)$ refers to Lebesgue and Sobolev spaces, respectively, $1 \leq p < \infty$, $k \geq 1$. Let $\beta = (\beta_1, \beta_2, \ldots, \beta_n) \in \mathbf{N}^n$ denote a multi-index of directions of the partial derivative, its absolute value defined by $|\beta| := \sum_i \beta_i$. The Lebesgue and Sobolev norms and semi-norms are defined as usual,

$$\|f\|_{L^p(\Omega)} = \left(\int_\Omega |f|^p \, \mathrm{d}\boldsymbol{x} \right)^{1/p}, \qquad 1 \leq p < \infty, \tag{3.36a}$$

$$|f|_{H^k(\Omega)} = \left(\sum_{|\beta|=k} \|\partial^\beta f\|^2_{L^2(\Omega)} \right)^{1/2}, \quad k \geq 1, \tag{3.36b}$$

$$\|f\|_{H^k(\Omega)} = \left(\sum_{|\beta|\leq k} \|\partial^\beta f\|^2_{L^2(\Omega)} \right)^{1/2}, \quad k \geq 1. \tag{3.36c}$$

3.3.1 Overview

The system of governing equations (3.27)–(3.29) is split as follows, cp. [46, 50]. The quasi-static three-field system is solved for solid velocity $\boldsymbol{v}_\mathrm{s}$, fluid pressure p_f and compaction pressure p_c with a finite element method, where the term *quasi-static* refers to the fact that the equations are not explicitly time-dependent. The porosity is updated on the finite element mesh nodes using the divergence of the obtained solid velocity. These two steps are iteratively repeated to resolve nonlinearities until the solution to the three-field system has reached the desired tolerance. Now, the advection equation (3.29) is solved in an explicit Euler manner to advect phase properties such as density and viscosities. Then, the procedure starts over for the next time step, see section 3.3.7 for algorithmic details.

3.3.2 Weak Formulation of the Three-Field System

Let $\boldsymbol{\alpha} : \boldsymbol{\beta} = \sum_{i,j} \boldsymbol{\alpha}_{ij} \boldsymbol{\beta}_{ij}$ denote the so-called Frobenius product for tensors $\boldsymbol{\alpha}, \boldsymbol{\beta}$. Furthermore, let $(\boldsymbol{v}_\mathrm{s}, p_\mathrm{f}, p_\mathrm{c})$ be a classical solution to (3.27), (3.30) and assume, without loss of generality, homogeneous Dirichlet boundary conditions on $\Gamma_D = \partial\Omega$. First, we multiply the three-field system (3.27) with arbitrary test functions $\boldsymbol{w} \in \boldsymbol{H} := \left(H^1_0(\Omega)\right)^2$, $q_\mathrm{f} \in H^1(\Omega)$, $q_\mathrm{c} \in L^2(\Omega)$, respectively, integrate over the domain Ω and apply Green's theorem,

$$\int_\Omega \boldsymbol{\tau}_\mathrm{s} : \dot{\boldsymbol{\varepsilon}}(\boldsymbol{w}) \, \mathrm{d}\boldsymbol{x} - \int_\Omega p_\mathrm{f} \nabla \cdot \boldsymbol{w} \, \mathrm{d}\boldsymbol{x} - \int_\Omega p_\mathrm{c} \nabla \cdot \boldsymbol{w} \, \mathrm{d}\boldsymbol{x} = \\ = - \int_\Omega \bar{\varrho} \boldsymbol{g} \cdot \boldsymbol{w} \, \mathrm{d}\boldsymbol{x}, \tag{3.37a}$$

$$- \int_\Omega q_\mathrm{f} \nabla \cdot \boldsymbol{v}_\mathrm{s} \, \mathrm{d}\boldsymbol{x} - \int_\Omega K_D \nabla p_\mathrm{f} \cdot \nabla q_\mathrm{f} \, \mathrm{d}\boldsymbol{x} = - \int_\Omega K_D \varrho_\mathrm{f} \boldsymbol{g} \cdot \nabla q_\mathrm{f} \, \mathrm{d}\boldsymbol{x}, \tag{3.37b}$$

$$- \int_\Omega q_\mathrm{c} \nabla \cdot \boldsymbol{v}_\mathrm{s} \, \mathrm{d}\boldsymbol{x} - \int_\Omega \frac{p_\mathrm{c} q_\mathrm{c}}{\zeta_\mathrm{eff}} \, \mathrm{d}\boldsymbol{x} = - \int_\Omega \frac{\chi_p \Delta p^o}{\zeta_\mathrm{eff}} q_\mathrm{c}. \tag{3.37c}$$

We call (v_s, p_f, p_c) a weak solution of the three-field formulation (3.27) if it fulfills (3.37) for all $(w, q_f, q_c) \in \left(\boldsymbol{H} \times H^1(\Omega) \times L^2(\Omega)\right)$. We remind ourselves of the fact that the shear viscosity η_{eff} (and hence, the solid deviatoric stress $\boldsymbol{\tau}_s$), the bulk density $\bar{\varrho}$, the compaction viscosity ζ_{eff}, and the elastic stress build-up parameters χ_τ, χ_p depend on the porosity φ, and, therefore, implicitly inherit its time-dependence.

3.3.3 Comment on the Existence and Uniqueness of a Solution to the Three-Field System

Previous Results for Stokes Flow The structure of the three-field system keeps similarities of the Stokes system, cp., e.g., [74–76]. Under the assumption of K_D, p_c vanishing (i.e., zero porosity), the first two equations of (3.37) exactly recover the weak formulation of the Stokes system with fluid pressure p_f taking the role of total pressure. It is well-known that the Stokes system has a unique weak solution $(v, p) \in \boldsymbol{H} \times L^2(\Omega)$ (up to an additive constant for pressure), see, e.g., [74, 75].

Previous Results for Darcy Flow Most commonly, Darcy flow is an interpretation of two-phase flow in porous media. It has been investigated over the last decades and has been solved with numerous methods, most of which are based on mixed finite element and, more recently, discontinuous Galerkin approaches [4, 6–9]. When Darcy flow is considered as a mixed finite element formulation, it is known that the resulting weak formulation has a unique (v, p) solution in $H(\text{div}; \Omega) \times L^2(\Omega)$, where v and p denote Darcy velocity and pressure, respectively, see, e.g., [5, 6, 77]. Here, $H(\text{div}; \Omega)$ denotes the space of L^2 functions with divergence in L^2,

$$H(\text{div}; \Omega) := \left\{ v \in (L^2(\Omega))^d \,\middle|\, \nabla \cdot v \in L^2(\Omega) \right\}. \tag{3.38}$$

Three-Field System Based on what has been discussed so far, we suppose that a solution to (3.37) exists in the considered function spaces. However, we need to record that the three-field system has only very recently been proposed for the first time by Keller et al. [46], its weak form has only been formulated in [47, 78]. Hence, there are no theoretical results yet on whether or not a solution to the three-field system exists and, if so, whether or not this solution is unique. We note that the investigation of this question is not part of this work.

3.3.4 Discretization of the Three-Field System

Finite Element Spaces We choose to discretize the three-field system with a finite element method (FEM) that is known to be very flexible. It has also been used for the three-field system (with triangular elements) by Rhebergen et al. [47] and (with quadrilaterals) by Dannberg and Heister [78].

For what follows we confine ourselves to polygonal domains $\Omega_h \subset \mathbf{R}^2$ in the 2-dimensional case, $d = 2$, and a regular triangulation $\mathcal{T}_h$ thereof. We denote a general mesh element by E and set $\mathcal{T}_h := \{E_i\}_{i\in I}$, I a suitable index set, with $\Omega_h \subset \bigcup_{i\in I} \mathrm{cl}(E_i)$ and we require two elements E_i, E_j, $i \neq j$, to be either disjoint $E_i \cap E_j = \emptyset$, or to share a common edge or vertex. Furthermore, we denote the space of polynomials of (total) degree $\leq k$ on a mesh element E by $\mathrm{P}_k(E)$ and set $\mathrm{Q}_k(E) := \mathrm{P}_{k,k}(E)$, where

$$\mathrm{P}_{k_1,k_2}(E) := \left\{ p(x,z) \,\middle|\, p(x,z) = \textstyle\sum_{i\leq k_1, j\leq k_2} a_{ij}\, x^i z^j \right\}. \tag{3.39}$$

Now we can define approximation spaces of conforming biquadratic and bilinear finite elements,

$$\boldsymbol{X}_h = \left\{ \boldsymbol{v}_h \in \left(H_0^1(\Omega_h)\right)^2 \,\middle|\, \boldsymbol{v}_h|_E \in \left(\mathrm{Q}_2(E)\right)^2 \,\forall E \in \mathcal{T}_h \right\}, \tag{3.40a}$$

$$Q_h^1 = \left\{ q_h \in H^1(\Omega_h) \,\middle|\, q_h|_E \in \mathrm{Q}_1(E) \forall E \in \mathcal{T}_h \right\}, \tag{3.40b}$$

$$Q_h = \left\{ q_h \in L^2(\Omega_h) \,\middle|\, q_h|_E \in \mathrm{Q}_1(E) \forall E \in \mathcal{T}_h \right\}. \tag{3.40c}$$

We use the notation $\mathrm{Q}_2\mathrm{Q}_1\mathrm{Q}_1$ for this mixed finite element. On triangular meshes we use $\mathrm{P}_2\mathrm{P}_1\mathrm{P}_1$ analogously. An element of this kind is known as Taylor-Hood element (of 2nd order). It is commonly used in incompressible flow settings, see, e.g., [79–83].

Note that for Stokes flow the Scott-Vogelius element $\mathrm{Q}_2\mathrm{P}_{-1}$ using continuous, piecewise biquadratic velocity and discontinuous linear pressure shape functions is even more common [84–86] as it more strictly enforces local mass conservation for incompressible flows. It has been shown to be inf-sup stable [87, 88].

Variational Formulation Now we can state the variational formulation of the three-field system. Find $(\boldsymbol{v}_{\mathrm{s},h}, p_{\mathrm{f},h}, p_{\mathrm{c},h}) \in \boldsymbol{X}_h \times Q_h^1 \times Q_h$ such that for all $(\boldsymbol{w}, q_\mathrm{f}, q_\mathrm{c}) \in \boldsymbol{X}_h \times Q_h^1 \times Q_h$,

$$a_h(\boldsymbol{v}_{\mathrm{s},h}, \boldsymbol{w}) + b_h(p_{\mathrm{f},h}, \boldsymbol{w}) + b_h(p_{\mathrm{c},h}, \boldsymbol{w}) = -\int_\Omega \bar{\varrho}\boldsymbol{g}\cdot\boldsymbol{w} + \chi_\tau \tilde{\boldsymbol{\tau}}_\mathrm{s}^o : \nabla \boldsymbol{w}\, \mathrm{d}\boldsymbol{x}, \tag{3.41a}$$

$$b_h(q_\mathrm{f}, \boldsymbol{v}_{\mathrm{s},h}) - d_h(p_{\mathrm{f},h}, q_\mathrm{f}) = -\int_\Omega K_D \varrho_\mathrm{f} \boldsymbol{g}\cdot\nabla q_\mathrm{f}\, \mathrm{d}\boldsymbol{x}, \tag{3.41b}$$

$$b_h(q_\mathrm{c}, \boldsymbol{v}_{\mathrm{s},h}) - c_h(p_{\mathrm{c},h}, q_\mathrm{c}) = -\int_\Omega \frac{\chi_p \Delta p^o}{\zeta_\mathrm{eff}} q_\mathrm{c}\, \mathrm{d}\boldsymbol{x}, \tag{3.41c}$$

where

$$a_h(\boldsymbol{v}, \boldsymbol{w}) = \int_\Omega 2\eta_{\text{eff}} \left(\dot{\boldsymbol{\varepsilon}}(\boldsymbol{v}) : \dot{\boldsymbol{\varepsilon}}(\boldsymbol{w}) - \frac{1}{3}(\nabla \cdot \boldsymbol{v})(\nabla \cdot \boldsymbol{w}) \right) \mathrm{d}x, \tag{3.42a}$$

$$b_h(p, \boldsymbol{v}) = -\int_\Omega p(\nabla \cdot \boldsymbol{v}) \, \mathrm{d}x, \tag{3.42b}$$

$$d_h(p, q) = \int_\Omega K_D \nabla p \cdot \nabla q \, \mathrm{d}x, \tag{3.42c}$$

$$c_h(p, q) = \int_\Omega \frac{pq}{\zeta_{\text{eff}}} \, \mathrm{d}x. \tag{3.42d}$$

For these bilinear functions, the element $\mathrm{Q_2Q_1Q_1}$ fulfills a Babuška-Brezzi stability condition, cp. [89], [90, sec. III.§7], [91, sec. 12.2], i.e.,

$$\inf_{p \in Q_h} \sup_{\boldsymbol{v} \in \boldsymbol{X}_h} \frac{b_h(p, \boldsymbol{v})}{\|p\|_{L^2(\Omega)} \|\boldsymbol{v}\|_{\boldsymbol{H}}} = \beta_h > 0, \tag{3.43}$$

which follows directly from equivalent statements about the discretized weak Stokes flow equations, see, e.g., [74, 89, 92].

For the vector u containing the discrete velocity and pressure components in the space $\boldsymbol{X}_h \times Q_h^1 \times Q_h$ the system can be written in block matrix form as

$$\begin{bmatrix} K & G^\mathsf{T} & G^\mathsf{T} \\ G & -D & 0 \\ G & 0 & -C \end{bmatrix} u = \begin{bmatrix} f_1 \\ f_2 \\ f_3 \end{bmatrix}, \tag{3.44}$$

where the matrix blocks $K \equiv K(\eta_{\text{eff}})$, G, $D \equiv D(K_D)$, $C \equiv C(\zeta_{\text{eff}})$ are obtained from discretizing the bilinear forms $a_h(\cdot,\cdot)$, $b_h(\cdot,\cdot)$, $d_h(\cdot,\cdot)$, $c_h(\cdot,\cdot)$, respectively.

Rhebergen et al. [47] have presented a study on optimal preconditioners for the resulting linearized system. As we consider only 2D setups, we opt not to use a sophisticated preconditioner. Instead we use simple left and right preconditioner matrices of Jacobi type, see, e.g., [93–95]. The preconditioned system is solved directly using the MA57 solver for sparse matrices [96]. We note that for larger scale (3D) experiments it is likely that more advanced preconditioners would be required.

Error Estimates Verfürth [89] has shown optimal convergence of the Taylor-Hood element. From previous results on the application of finite element methods for Stokes or Darcy flow, we know that the following estimate holds for a velocity-pressure approximation $(\boldsymbol{v}_h, p_h)$ obtained with the Taylor-Hood finite element, given a sufficiently regular solution $(\boldsymbol{v}, p) \in \left(H^{k+1}(\Omega)\right)^d \times H^{l+1}(\Omega)$, see, e.g., [5, 91, 97],

$$\|\boldsymbol{v}-\boldsymbol{v}_h\|_{\boldsymbol{H}}+\|p-p_h\|_{L^2(\Omega)} \leq c^*\left(h^k\,|\boldsymbol{v}|_{(H^{k+1}(\Omega))^d}+h^{l+1}\,|p|_{H^{l+1}(\Omega)}\right), \tag{3.45}$$

where $c^* > 0$ is a generic constant. Additionally, for convex polygonal domains Ω the following estimate holds,

$$\|\boldsymbol{v}-\boldsymbol{v}_h\|_{L^2(\Omega)} \leq c^*\left(h^{k+1}\,|\boldsymbol{v}|_{(H^{k+1}(\Omega))^d}+h^{l+2}\,|p|_{H^{l+1}(\Omega)}\right). \tag{3.46}$$

As the coupled three-field system we consider is more complex than the Stokes or Darcy flow, we cannot directly deduce convergence orders from these results. However, we note that we do not expect more than third order convergence of the L^2 velocity error (depending on the regularity of the solution rather second order). Furthermore, we expect not more than first to second order convergence for the H^1 velocity error and the L^2 fluid pressure error. Experimental orders of convergence (EOC) of L^2 and H^1 errors of velocity, fluid pressure and compaction pressure are presented in section 3.4.1. Note that this is one of the first reports on the EOC for the three-field system, only predated by [47].

3.3.5 Porosity Evolution

For the porosity update equation (3.28) we choose a Crank-Nicolson finite difference approach to obtain $\varphi_{i+1}(t_{n+1})$ in iteration $(i+1)$ of time step t_{n+1} as follows,

$$\begin{aligned} 0 &= \frac{\partial\varphi_{i+1}}{\partial t}-\nabla\cdot\left((1-\varphi_{i+1})\boldsymbol{v}_{\mathrm{s},i+1}\right) \\ &\approx \frac{\varphi_{i+1}^{(n+1)}-\varphi^{(n)}}{\Delta t}-\frac{1}{2}\left((1-\varphi^{(n)})\nabla\cdot\boldsymbol{v}_{\mathrm{s}}^{(n)}+(1-\varphi_i^{(n+1)})\nabla\cdot\boldsymbol{v}_{\mathrm{s},i+1}^{(n+1)}\right), \end{aligned} \tag{3.47}$$

where $\varphi_i^{(n)}$ denotes the numerically obtained value of porosity in iteration i of time step n, analogously for solid velocity $\boldsymbol{v}_{\mathrm{s}}$. Note that the advective term $\boldsymbol{v}_{\mathrm{s}}\cdot\nabla\varphi$ is not included in this as the advection is explicitly handled on the Lagrangian markers, see below.

3.3.6 Material Advection

The velocity solution obtained on mesh nodes is interpolated to the marker locations using the (quadratic) finite element shape functions. Then, each

marker is moved at its respective velocity. The Lagrangian form of the material advection equation is solved with an explicit Euler method, where the superscript (n) denotes the quantity after the nth time step,

$$\boldsymbol{x}^{(n+1)} = \boldsymbol{x}^{(n)} + \Delta t \, \boldsymbol{v}_{\mathrm{s}}^{(n)}. \tag{3.48}$$

3.3.7 Implementation

The implementation of MVEP2 follows a marker-and-cell approach that has been introduced in the 1960's for viscous incompressible flows [98–100] but remains popular up to the present day, see, e.g., [101–104]. The reference frame is arbitrary Lagrangian-Eulerian as the fluid flow equations are solved on a Eulerian mesh but phase markers and mesh nodes are advected in a Lagrangian fashion. MVEP2 uses functionality from finite element utilities *mutils* and applies the MILAMIN-style vectorized matrix assembly [105]. Its algorithmic outline is setup as follows, see also [58, 106, 107].

1. Define initial conditions on markers.
2. Start time step loop:
   a) Create mesh.
   b) Interpolate properties from markers to mesh and quadrature integration points.
   c) Solve non-linear system iteratively:
      i. Update material properties (density, viscosity,…) on integration points using current solution guess.
      ii. Assemble block matrices and right-hand side vectors for three-field system.
      iii. Solve linearized system for solid velocity, fluid pressure and compaction pressure.
      iv. Determine stresses and strain rates on integration points.
      v. Update porosity according to current divergence field.
      vi. Check convergence criterion and loop back to step 2c if necessary.
   d) If convergence criterion is reached determine fluid velocity.
   e) Interpolate properties from mesh nodes to markers.
   f) Advect mesh nodes with solid velocity, markers with their respective (solid or fluid) velocity.
3. Compute new CFL time step and loop to step 2 for next time step.

The porosity update in step 2(c)v is done as described in section 3.3.5. The advection in step 2f is done with an explicit first-order Euler scheme and we

apply a Courant-Friedrichs-Lewy (CFL) condition taking into account solid as well as fluid velocities to determine the size of the time step, cp. section 3.3.6,

$$\Delta t = \min_{i \in I} \left(\frac{h_i}{2 v_i} \right), \tag{3.49}$$

where h_i denotes a characteristic length scale for the mesh element E_i, and v_i denotes the maximum of the fluid and solid velocity obtained in nodes of the mesh element E_i.

For numerical stability we introduced cut-offs for certain physical properties, namely, the shear and compaction viscosity. For the effective shear viscosity η_{eff} we allow for six to nine orders of magnitude around the reference viscosity, e.g., $\eta_{\text{eff}} \in [10^{18}, 10^{25}]$ Pa s. The compaction viscosity is limited by a prescribed maximum compaction-to-shear-viscosity ratio of 10^6, cp. [46, 65]. Keller et al. [46] also employ a lower cut-off for permeability to avoid an instability that is related to the chosen finite element discretization. Hence, we do not need it in the framework we described.

3.4 Numerical Experiments

In this section we present a small set of numerical experiments. First, we describe a 2D setup to obtain the experimental order of convergence, see section 3.4.1. In section 3.4.2 we present three different benchmarks to showcase poro-elastic as well as visco-elastic effects and plastic failure. A solitary wave benchmark is provided in section 3.4.3.

3.4.1 Experimental Order of Convergence

In this section we present a synthetic benchmark setup that we use to obtain the experimental order of convergence (EOC) of the described FEM. As initial condition we introduce a Gaussian melt pulse with a maximum porosity of 10 % into an otherwise homogeneous domain of size 20 km by 20 km centered around $(x_c, z_c) = (0\,\text{km}, -10\,\text{km})$,

$$\varphi(t_0) = \varphi_0 = 0.1 \exp\left(-10^{-7}((x - x_c)^2 + (z - z_c))\right). \tag{3.50}$$

The host rock behaves elastically with realistic elastic moduli G, K_0, but does not undergo plastic failure. We run the setup for a single time step of 100 yrs at different spatial resolutions. Maximum resolution on a square grid is 512 by 512 $Q_2Q_1Q_1$ elements resulting in more than 2.6×10^6 degrees of freedom.

Table 3.1: The table below lists the material parameters that are used in the setup to determine the experimental order of convergence for the three-field system, see section 3.4.1. If not otherwise mentioned, the values remain valid for the following setups. Please note that the plasticity parameters C, ϕ, σ_T do not have an effect since there is no sufficient stress build-up in a single time step.

Symbol	Name	Value
ϱ_s	solid density	$3.0 \times 10^3\,\mathrm{kg\,m^{-3}}$
ϱ_f	fluid density	$2.5 \times 10^3\,\mathrm{kg\,m^{-3}}$
η_0	reference shear viscosity	$10^{18}\,\mathrm{Pa\,s}$
η_f	fluid viscosity	$10^2\,\mathrm{Pa\,s}$
r_ζ	compaction viscosity factor	1
κ_0	reference permeability	$10^{-8}\,\mathrm{m^2}$
K_0	reference pore modulus	5 GPa
G	reference shear modulus	50 GPa
α	melt weakening parameter	27
C	cohesion	40 MPa
ϕ	friction angle	30°
σ_T	tensile strength	20 MPa
g	gravitational acceleration	$10\,\mathrm{m\,s^{-2}}$

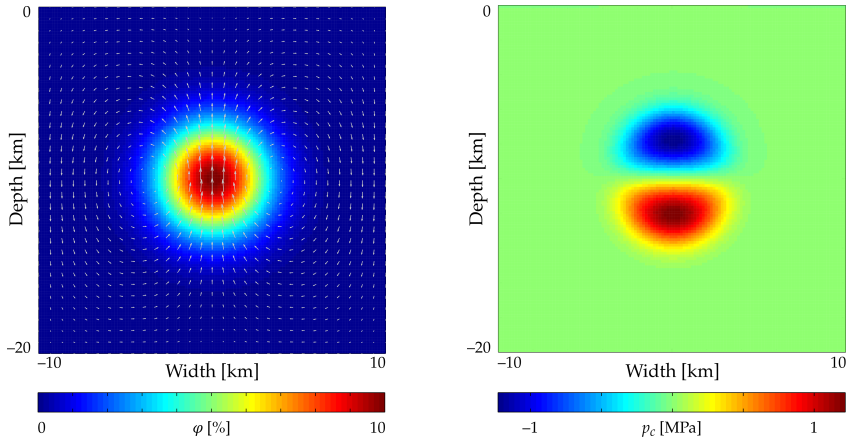

Figure 3.1: Porosity field with solid velocity arrows (left) and compaction pressure (right) after one time step. The negative compaction pressure values lead to positive divergence which leads to an increase in porosity. In a longer simulation, this interaction would cause the porosity pulse to rise upwards. The lateral free-slip boundary conditions lead to two convection cells in the domain. The maximum velocity magnitude is about $5\,\mathrm{cm\,yr^{-1}}$.

Table 3.2: For the benchmark setup presented in section 3.4.1 the table lists the number of elements, the resulting grid size, and the L^2 (top) and H^1 errors (bottom) of the three independent variables solid velocity v_s, fluid pressure p_f and compaction pressure p_c (left to right), as well as the rate of convergence, see equations (3.51) and (3.52). Errors are obtained by comparison with the approximate solution obtained at high resolution (512 by 512 elements). As the bottom lines correspond to a resolution relatively close to the reference resolution we consider them less significant, but include them for completeness.

N	h [m]	$e^0(\boldsymbol{v}_{s,h})$	$\mathrm{rt}(\boldsymbol{v}_{s,h})$	$e^0(p_{f,h})$	$\mathrm{rt}(p_{f,h})$	$e^0(p_{c,h})$	$\mathrm{rt}(p_{c,h})$
16^2	1.25×10^3	2.8×10^{-2}		5.0×10^{-5}		6.8×10^{-2}	
32^2	6.25×10^2	7.2×10^{-3}	1.95	1.8×10^{-5}	1.46	2.6×10^{-2}	1.41
64^2	3.13×10^2	1.7×10^{-3}	2.05	9.5×10^{-6}	0.94	1.4×10^{-2}	0.89
128^2	1.56×10^2	4.0×10^{-4}	2.13	5.8×10^{-6}	0.71	8.6×10^{-3}	0.69
256^2	7.81×10^1	7.6×10^{-5}	2.38	4.9×10^{-6}	0.26	7.2×10^{-3}	0.25

N	h [m]	$e^1(\boldsymbol{v}_{s,h})$	$\mathrm{rt}(\boldsymbol{v}_{s,h})$	$e^1(p_{f,h})$	$\mathrm{rt}(p_{f,h})$	$e^1(p_{c,h})$	$\mathrm{rt}(p_{c,h})$
16^2	1.25×10^3	3.8×10^{-2}		8.8×10^{-4}		9.9×10^{-1}	
32^2	6.25×10^2	1.1×10^{-2}	1.77	5.9×10^{-4}	0.57	6.7×10^{-1}	0.56
64^2	3.13×10^2	3.8×10^{-3}	1.57	3.9×10^{-4}	0.60	4.4×10^{-1}	0.60
128^2	1.56×10^2	1.7×10^{-3}	1.15	2.5×10^{-4}	0.67	2.8×10^{-1}	0.67
256^2	7.81×10^1	1.2×10^{-3}	0.48	1.7×10^{-4}	0.52	1.9×10^{-1}	0.52

In Table 3.2 we present relative L^2 errors e^0 and H^1 errors e^1 with respect to the solid velocity $\boldsymbol{v}_s^*$, fluid pressure p_f^* and compaction pressure p_c^* on the finest grid level,

$$e^0(\psi_h) := \frac{\|\psi_h - \psi^*\|_{L^2}}{\|\psi^*\|_{L^2}}, \qquad e^1(\psi_h) := \frac{\|\psi_h - \psi^*\|_{H^1}}{\|\psi^*\|_{H^1}}, \tag{3.51}$$

and the experimental order of convergence rt,

$$\mathrm{rt}(\psi_h) := \log_{2h/h}\left(e^{\{0,1\}}(\psi_{2h})/e^{\{0,1\}}(\psi_h)\right). \tag{3.52}$$

We observe that the L^2 error of the solid velocity $\boldsymbol{v}_s$ converges with approximately second order. The pressure terms converge rapidly first, but the rate decreases and we expect the error to stagnate for higher resolutions, similar to what Rhebergen et al. [47] observed. Improved convergence behavior might be retrieved for a fine-tuned criterion for iterative solver termination.

As expected, the H^1 error of the solid velocity decreases more slowly than the L^2 error. The rate of convergence decreases indicating that the derivatives might reach a point where higher resolutions do not improve the approximate solution. Yet, the H^1 errors of the pressure terms decrease at a more or less constant rate of $\sim$0.6, although the compaction pressure p_c was assumed to be in $L^2(\Omega)$ only.

3.4.2 Elasticity and Plasticity Benchmarks

In this section we present qualitative benchmark models that are common in testing visco-elasto-plastic as well as poro-elasto-plastic rheologies. First, we show 0-D models that are subjected to extensional or shear boundary conditions to test compaction and shear stress build-up, respectively, and plastic failure, see [46]. Additionally, we show a 2-D model with a viscosity heterogeneity that is subjected to either compressional or extensional boundary conditions until it develops localized shear zones, see, e.g., [108–110].

Visco-Elasto-Plastic Evolution of Compaction Stress We consider an initially homogeneous model domain $(-1,1) \times (-1,1)$ discretized into 2 by 2 elements. We apply extensional boundary conditions in horizontal direction with a volumetric strain rate of $\dot{v}_{BG} = 10^{-15}\,\mathrm{s}^{-1}$, free-slip on the top and bottom boundary. Due to the incompressibility constraint in typical Stokes flow systems this setup cannot be solved without the additional two-phase equations. The material parameters are given in Table 3.3 (top). Shear elasticity and shear failure are switched off for this setup.

Table 3.3: The tables below list the material parameters different from Table 3.1 that are used in the 0D setups to investigate the evolution of compaction stress (top), and the evolution of shear stress (bottom).

Symbol	Name	Value
η_0	reference shear viscosity	10^{21} Pa s
K_0	reference pore modulus	10 GPa
C	cohesion	100 MPa
σ_T	tensile strength	50 MPa
φ_0	initial porosity	1 %
g	gravitational acceleration	0 m s^{-2}
η_0	reference shear viscosity	10^{22} Pa s
G	reference shear modulus	10 GPa
C	cohesion	17 MPa
ϕ	friction angle	30°
α	melt weakening parameter	0
g	gravitational acceleration	0 m s^{-2}

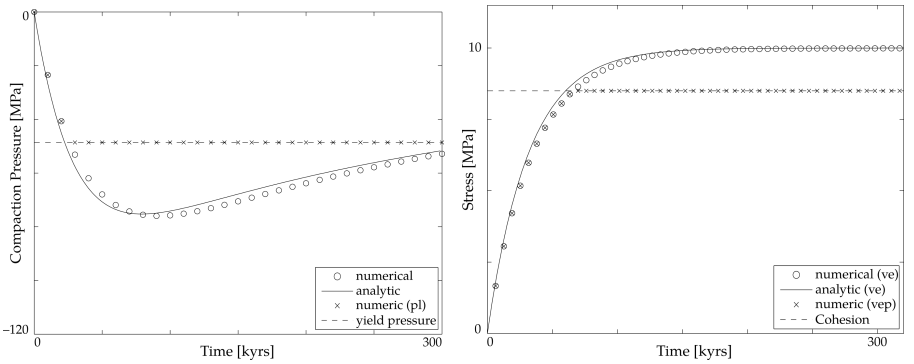

Figure 3.2: Left: Compaction stress evolution with time for a 0D benchmark under constant volumetric expansion. The solid line shows the analytically determined value for *deactivated* tensile plasticity, the dashed line indicates the failure criterion in case tensile plasticity is *activated*. Circle and X markers (○, ×) show numerically obtained values of the compaction pressure p_c.

Right: Shear stress evolution with time under pure shear deformation. Analogously, the solid line shows the analytically expected shear stress evolution if shear plasticity is *deactivated*, the dashed line indicates the failure criterion (cohesion). Circle and X markers (○, ×) show numerically obtained values of the square root of the second invariant of the deviatoric stress tensor τ_{II}.

The compaction pressure p_c is expected to comply with the analytically obtained value,

$$p_c = -(1-\varphi)\zeta\dot{v}_{BG}(1-\exp(-K_\varphi t/\zeta)). \tag{3.53}$$

The yield criterion is derived from the tensile strength and the arising stress,

$$p_y = \tau - \sigma_T = 49\,\text{MPa}. \tag{3.54}$$

Figure 3.2 (left) shows the compaction stress evolution versus time with plasticity activitated (× markers) and deactivated (○ markers) as well as the analytic stress prediction (solid line) and the failure criterion (dashed line).

Visco-Elasto-Plastic Evolution of Shear Stress Let us now consider a homogeneous model domain $(-1,1)\times(-1,1)$ discretized into 2 by 2 elements. The material parameters are listed in Table 3.3 (bottom). We prescribe a (low) constant porosity $\varphi = 0.1\,\%$, and apply a shear boundary condition by extending the domain in horizontal direction and compressing it by the same amount in vertical direction with the background strain rate $\dot{\varepsilon}'_{BG} = 10^{-15}\,\text{s}^{-1}$.

This system (and the one in the following section) would usually be solved as a Stokes flow system only and, accordingly, we switch off the melt-weakening effect of the porosity ($\alpha = 0$). Hence, this test shows that in the case of a more complex system of equations (with additional rheological constitutive equations), the shear stress evolution and the shear failure are still modelled appropriately.

For a Maxwell fluid we can determine the shear stress evolution analytically given the above parameters [111, sec. 7–10],

$$\tau = 2\eta\dot{\varepsilon}'_{BG}(1-\exp(-tG/\eta)). \tag{3.55}$$

If a plasticity criterion is applied, the shear stress is effectively cut off for values above the failure criterion, in this case cohesion $C = 17\,\text{MPa}$.

Figure 3.2 (right) shows the shear stress evolution versus time with plasticity activitated (× markers) and deactivated (○ markers) as well as the analytic stress prediction (solid line) and the failure criterion (dashed line).

Visco-Elasto-Plastic Shear Localization The numerical initiation of shear bands has become a common test for implementations of numerical methods in the context of lithosphere dynamics. Kaus [58] has performed a detailed study on this using the previous version of MVEP2. Therefore, we only present a brief example showing that numerical modelling of the brittle crust remains valid when two-phase flow is introduced, i.e., when the coupled three-field system is solved.

Table 3.4: The table below lists the material parameters different from Table 3.1 that are used in the shear localization benchmark setup.

Symbol	Name	Value
ϱ_s	solid density	$2.7 \times 10^3\,\mathrm{kg\,m^{-3}}$
η_0	reference shear viscosity	$10^{25}\,\mathrm{Pa\,s}$
η^*	viscosity heterogeneity	$10^{20}\,\mathrm{Pa\,s}$
G	reference shear modulus	10 GPa
C	cohesion	40 MPa
ϕ	friction angle	30°
α	melt weakening parameter	0

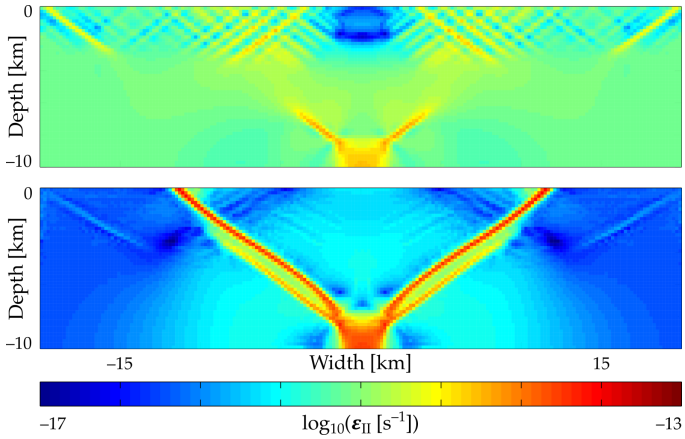

Figure 3.3: Snapshots showing the square root of the second invariant of the strain rate tensor $\dot{\varepsilon}_{II}$ from the shear localization benchmark setup after 12 (top) and 20 (bottom) time steps, $\Delta t = 20\,\mathrm{kyrs}$. We observe that the localization is initiated at the viscosity heterogeneity at the bottom center of the domain. Additionally, small shear zones develop at the top of the domain where the pressure is low and, therefore, the Drucker-Prager yield criterion is reached earlier. Ultimately, the shear deformation localizes in a single narrow shear zone.

The parameters for this setup are presented in Table 3.4. The shear localization is initiated at the prescribed viscosity heterogeneity at the bottom center of the domain.

The domain is 40 km wide and 10 km deep with a viscosity heterogeneity at the bottom center domain with dimensions 3.2 km by 0.8 km. We compress the domain laterally at a background strain rate of $\dot{\varepsilon}'_{\mathrm{BG}} = 10^{-15}\,\mathrm{s}^{-1}$ for 20 time steps, $\Delta t = 20\,\mathrm{kyrs}$. It is spatially discretized into 200 by 50 $\mathrm{Q_2Q_1Q_1}$ elements. Poro-elasticity and tensile plasticity are switched off. A low and constant porosity of $\varphi = 0.1\,\%$ is prescribed. Figure 3.3 shows snapshots of the square root of the second invariant of the strain rate tensor after 12 and 20 time steps, respectively.

3.4.3 Solitary Wave Benchmark

The propagation of a solitary wave under compaction and dilation of a surrounding solid matrix has been described in [112, 113]. It has become a common benchmark in melt migration modelling, see, e.g., [44, 46, 62, 78, 114, 115].

For a 1D solitary wave we fix the shear and compaction viscosity at $\eta = \zeta = 10^{20}\,\mathrm{Pa\,s}$, the fluid viscosity at $\eta_{\mathrm{f}} = 10^{2}\,\mathrm{Pa\,s}$, and introduce the characteristic compaction length $\delta \equiv \delta(\varphi)$,

$$\delta := \left(K_D\left(\zeta + \tfrac{4}{3}\eta\right)\right)^{1/2}. \tag{3.56}$$

Here, we use a power-law permeability $\kappa_\varphi = \kappa_0\varphi^3$, $\kappa_0 = 5\times10^{-9}\,\mathrm{m}^2$. This parameter set represents a partially molten upper mantle regime at low melt fraction, cp. [46].

We prescribe a low background porosity $\varphi_0 = 0.1\,\%$ with a perturbation following a discrete representation of the solitary wave as given by Barcilon and Richter [112]. We expect the wave to propagate without changing its shape at the analytically determined constant (non-dimensional) wave speed $c_{sw} = 2A + 1$, where A denotes the relative wave amplitude. For the compaction length at background porosity we obtain

$$\delta_0 := \delta(\varphi_0) \approx 3.42\,\mathrm{m}. \tag{3.57}$$

We use a pseudo-1D profile by fixing the horizontal number of elements at $n_x = 2$ and varying the vertical resolution of a model domain with the depth $D = 400\delta_0$. We start with $n_z = 150$ vertical elements and double the resolution until we reach 2 by 2400 elements. Figure 3.4 shows the initial porosity and compaction pressure profiles (solid lines), as well as the numerically ob-

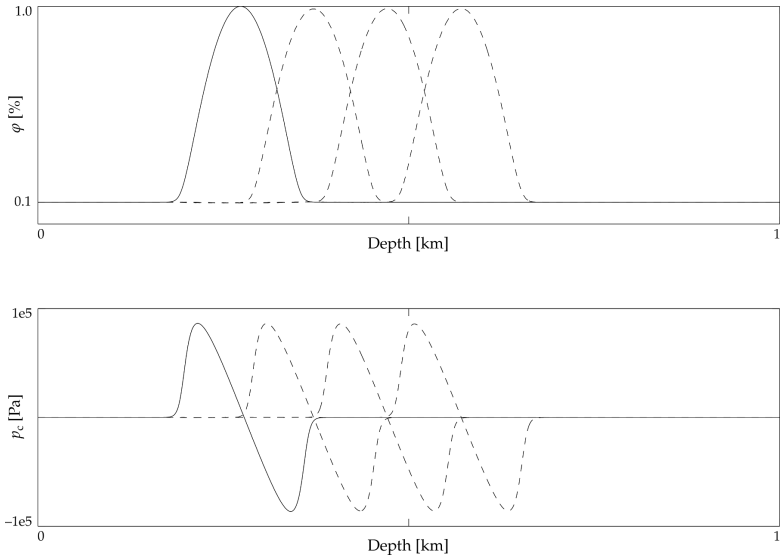

Figure 3.4: Initial porosity (top) and compaction pressure profile (bottom) in the solitary wave benchmark (solid lines), as well as numerically obtained profiles after 600, 1200 and 1800 kyrs corresponding to 20, 40 and 60 time steps with $\Delta t = 30$ kyrs. Simulation is run on 2 by 2400 $Q_2Q_1Q_1$ elements.

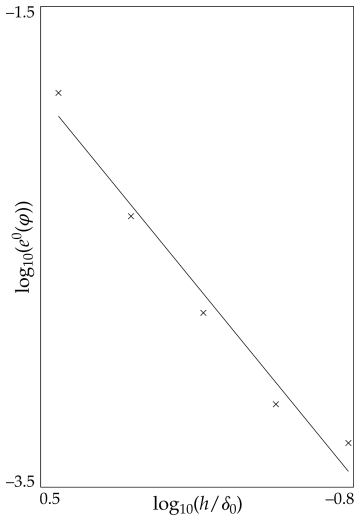

Figure 3.5: Non-dimensional grid size h/δ_0 versus L^2 porosity error for the solitary wave benchmark at resolutions of 150, 300, 600, 1200 and 2400 vertical $Q_2Q_2Q_1$ elements with respect to analytic solution. The slope of the linear trend is 1.23.

n_z	h [m]	$e^0(\varphi_h)$
150	9.11	1.4×10^{-2}
300	4.55	4.2×10^{-3}
600	2.28	1.7×10^{-3}
1200	1.14	7.0×10^{-4}
2400	0.57	4.8×10^{-4}

Table 3.5: Number of elements in vertical direction n_z, corresponding mesh size h, and L^2 error of porosity $e^0(\varphi_h)$ for the solitary wave benchmark with a characteristic compaction length of $\delta_0 \approx 3.42$ m.

tained profiles after 600, 1200 and 1800 kyrs (dashed lines), corresponding to 20, 40 and 60 time steps of size $\Delta t = 30$ kyrs at highest spatial resolution. In Figure 3.5 and Table 3.5 we present the L^2 errors of the porosity profile after 1.2 Myrs (40 time steps) for increasing vertical resolution. In this period the wave travels approximately the distance of its own wavelength, see Figure 3.4.

3.5 Discussion

The above coupled formulation of Stokes and Darcy flow in melt migration modelling is still novel, being initially published in 2013 [46]. We provide the mathematical framework to approximate its solution with a numerical method, namely the finite element method. Yet, this is to be seen as a first step in investigating mathematical properties of this formulation.

Previous results on Stokes and Darcy flow being considered separately indicate a good chance of the three-field formulation to have a solution in the proposed function spaces. However, uniqueness (modulo an additive constant in fluid pressure) is an open question. The answer to this question is certainly non-trivial and is not covered in this work.

We deduce expectations about the convergence of the described method in section 3.3.4. The ideal L^2 interpolation error would have decreased at third order for solid velocity v_s, at second order for fluid pressure p_f and compaction pressure p_c. For the H^1 error of solid velocity and fluid pressure second and first order would have been optimal, respectively. Reduction of this order in the total error needs to be expected due to the explicit first-order time stepping method and insufficient regularity of the weak solution for the particular setup.

Therefore, the expectations are partially met as we observe in section 3.4.1. The L^2 error of the solid velocity v_s decreases at second order, the L^2 error of the pressure terms a bit more slowly and at a slightly decreasing rate. This might be due to the termination criterion of the iterative solver that had been fine-tuned for the Stokes problem only. The only reference for EOCs for the three-field system is given by Rhebergen et al. [47] who observe a similar behavior for the fluid pressure error related to the convergence criterion. However, they do not present compaction pressure errors or H^1 errors of any of the three variables.

Remarkably, the H^1 error of the compaction pressure p_c reduces at a constant rate although it was not required to be weakly differentiable, but only in $L^2(\Omega)$.

The visco-elasto-plastic benchmark setups show the validity of the numerical method and its implementation for problems with shear and volumetric

deformation and failure. In particular, we observe that the method robustly reproduces results from Stokes flow equations when the porosity φ approaches zero. For zero porosity the second and third equation of the three-field system (3.27) approach linear dependence as K_D and ζ_{eff} approach zero and infinity, respectively. The prescribed maximum compaction to shear viscosity ratio, see section 3.3.7, effectively caps the compaction viscosity at a value that *(a)* prevents poro-elastic effects in absence of porosity and at the same time *(b)* avoids the algebraic singularity of the three-field system.

Finally, the solitary wave benchmark proves that the method is capable of handling the respective mode of magma transport. The Earth's upper mantle is considered to provide a regime that favors this type of migration.

3.6 Conclusions

We present in this chapter a system of equations considered to govern coupled processes of magma and lithosphere dynamics. The weak formulation of this system is presented in equations (3.27)–(3.29) and a stable numerical method using finite elements of Taylor-Hood type is derived in section 3.3.4.

We show that the method (and its implementation) is capable of solving the coupled Stokes/Darcy system with visco-elasto-plastic rheologies and, in absence of porosity, robustly reproduces Stokes flow results.

The experimental orders of convergence for the L^2 and H^1 errors of solid velocity v_s, fluid pressure p_f and compaction pressure p_c investigated in section 3.4.1 are in consistency with the considerations from section 3.3.4. However, theoretical foundations to this are incomplete.

The presented method has been implemented in the open-source Matlab[1] software MVEP2[2] where it integrates seamlessly with the already exisiting part of the code. MVEP2 is used extensively in geodynamics research and teaching [58, 104, 106, 107, 116–120]. The extension of the code for two-phase flow problems is immediately available to everyone and, in particular, to users already familiar with MVEP2. This has the potential to push forward our understanding of melt migration processes from the Earth's upper mantle to the surface in the near future because for the first time a consistent visco-elasto-plastic coupled Stokes/Darcy flow implementation exists in a software tool with a considerable user base.

In the next chapter we present the first application of this method in a parameter study for lithospheric scale setups.

[1] MATLAB is a registered trademark of The MathWorks, Inc.
[2] MVEP2 is available at https://bitbucket.org/bkaus/mvep2.

References

[1] S. Whitaker. Flow in porous media I: A theoretical derivation of Darcy's law. *Transport in Porous Media*, 1(1):3–25, 1986. DOI:10.1007/BF01036523.

[2] H. F. Wang and M. P. Anderson. *Introduction to Groundwater Modeling: Finite Difference and Finite Element Methods*. Academic Press, Inc., San Diego, CA, USA, 1995. ISBN 978-0-080-57194-2.

[3] P. Vidstrand, S. Follin, J.-O. Selroos, J.-O. Näslund, and I. Rhén. Modeling of groundwater flow at depth in crystalline rock beneath a moving ice-sheet margin, exemplified by the Fennoscandian Shield, Sweden. *Hydrogeology Journal*, 21(1):239–255, 2012. ISSN 1435-0157. DOI:10.1007/s10040-012-0921-8.

[4] T. F. Russell and M. F. Wheeler. *Finite Element and Finite Difference Methods for Continuous Flows in Porous Media*, pages 35–106. Frontiers in Applied Mathematics. SIAM, Philadelphia, PA, USA, 1983. ISBN 978-0-898-71662-7. DOI:10.1137/1.9781611971071.ch2.

[5] A. Masud and T. J. R. Hughes. A stabilized mixed finite element method for Darcy flow. *Computer Methods in Applied Mechanics and Engineering*, 191(39–40):4341–4370, 2002. ISSN 0045-7825. DOI:10.1016/S0045-7825(02)00371-7.

[6] M. F. Wheeler and I. Yotov. A Multipoint Flux Mixed Finite Element Method. *SIAM Journal on Numerical Analysis*, 44(5):2082–2106, 2006. DOI:10.1137/050638473.

[7] B. Rivière, M. F. Wheeler, and V. Girault. Improved energy estimates for interior penalty, constrained and discontinuous Galerkin methods for elliptic problems. Part I. *Computational Geosciences*, 3(3-4):337–360, 1999. DOI:10.1023/A:1011591328604.

[8] B. Rivière, M. F. Wheeler, and K. Banaś. Part II. Discontinuous Galerkin method applied to a single phase flow in porous media. *Computational Geosciences*, 4(4):337–349, 2000. ISSN 1573-1499. DOI:10.1023/A:1011546411957.

[9] F. Brezzi, T. J. R. Hughes, L. D. Marini, and A. Masud. Mixed Discontinuous Galerkin Methods for Darcy Flow. *Journal of Scientific Computing*, 22(1):119–145, 2005. ISSN 1573-7691. DOI:10.1007/s10915-004-4150-8.

[10] T. J. R. Hughes, A. Masud, and J. Wan. A stabilized mixed discontinuous Galerkin method for Darcy flow. *Computer Methods in Applied Mechanics and Engineering*, 195(25–28):3347–3381, 2006. ISSN 0045-7825. DOI:10.1016/j.cma.2005.06.018.

[11] B. Rivière and M. Wheeler. Coupling locally conservative methods for single phase flow. *Computational Geosciences*, 6(3):269–284, 2002. ISSN 1573-1499. DOI:10.1023/A:1021266409023.

[12] Z. Chen, Z. Wang, L. Zhu, and J. Li. Analysis of the pressure projection stabilization method for the Darcy and coupled Darcy-Stokes flows. *Computational Geosciences*, 17(6):1079–1091, 2013. ISSN 1573-1499. DOI:10.1007/s10596-013-9376-9.

[13] G. Lin, J. Liu, L. Mu, and X. Ye. Weak Galerkin finite element methods for Darcy flow: Anisotropy and heterogeneity. *Journal of Computational Physics*, 276:422–437, 2014. ISSN 0021-9991. DOI:10.1016/j.jcp.2014.07.001.

[14] M. Krotkiewski, I. S. Ligaarden, K.-A. Lie, and D. W. Schmid. On the Importance of the Stokes-Brinkman Equations for Computing Effective Permeability in Karst Reservoirs. *Communications in Computational Physics*, 10(05):1315–1332, 2011. ISSN 1991-7120. DOI:10.4208/cicp.290610.020211a.

[15] M. Discacciati, E. Miglio, and A. Quarteroni. Mathematical and numerical models for coupling surface and groundwater flows. *Applied Numerical Mathematics*, 43(1–2):57–74, 2002. ISSN 0168-9274. DOI:10.1016/S0168-9274(02)00125-3. 19th Dundee Biennial Conference on Numerical Analysis.

[16] B. Rivière. Analysis of a Discontinuous Finite Element Method for the Coupled Stokes and Darcy Problems. *Journal of Scientific Computing*, 22(1):479–500, 2005. DOI:10.1007/s10915-004-4147-3.

[17] L. Badea, M. Discacciati, and A. Quarteroni. Numerical Analysis of the Navier-Stokes/Darcy Coupling. *Numerische Mathematik*, 115(2):195–22, 2010. DOI:10.1007/s00211-009-0279-6.

[18] C. D'Angelo and P. Zunino. Robust numerical approximation of coupled Stokes' and Darcy's flows applied to vascular hemodynamics and biochemical transport. *ESAIM: Mathematical Modelling and Numerical Analysis*, 45(3):447–476, 2011. ISSN 1290-3841. DOI: 10.1051/m2an/2010062.

[19] Z. H. Wang, C. Y. Wang, and K. S. Chen. Two-phase flow and transport in the air cathode of proton exchange membrane fuel cells. *Journal of Power Sources*, 94(1):40–50, 2001. ISSN 0378-7753. DOI:10.1016/S0378-7753(00)00662-5.

[20] X. Xie, J. Xu, and G. Xue. Uniformly Stable Finite Element Methods for Darcy-Stokes-Brinkman Models. *Journal of Computational Mathematics*, 26(3):435–455, 2008.

[21] H. C. Brinkman. A calculation of the viscous force exerted by a flowing fluid on a dense swarm of particles. *Applied Scientific Research*, 1(1):27–34, 1949. ISSN 0003-6994. DOI:10.1007/BF02120313.

[22] S. Badia and R. Codina. Unified Stabilized Finite Element Formulations for the Stokes and the Darcy Problems. *SIAM Journal on Numerical Analysis*, 47(3):1971–2000, 2009. DOI: 10.1137/08072632X.

[23] N. Chen, M. Gunzburger, and X. Wang. Asymptotic analysis of the differences between the Stokes-Darcy system with different interface conditions and the Stokes-Brinkman system. *Journal of Mathematical Analysis and Applications*, 368(2):658–676, 2010. ISSN 0022-247X. DOI: 10.1016/j.jmaa.2010.02.022.

[24] M. Discacciati, A. Quarteroni, and A. Valli. Robin-Robin Domain Decomposition Methods for the Stokes-Darcy Coupling. *SIAM Journal on Numerical Analysis*, 45(3):1246–1268, 2007. DOI:10.1137/06065091X.

[25] Y. Cao, M. Gunzburger, X. He, and X. Wang. Robin-Robin domain decomposition methods for the steady-state Stokes-Darcy system with the Beavers-Joseph interface condition. *Numerische Mathematik*, 117(4):601–629, 2011. ISSN 0945-3245. DOI:10.1007/s00211-011-0361-8.

[26] A. Caiazzo, V. John, and U. Wilbrandt. On classical iterative subdomain methods for the Stokes-Darcy problem. *Computational Geosciences*, 18(5):711–728, 2014. DOI:10.1007/s10596-014-9418-y.

[27] M. Discacciati and A. Quarteroni. Navier-Stokes/Darcy coupling: Modeling, Analysis, and Numerical Approximation. *Revista Matemática Complutense*, 22(2):315–426, 2009. DOI:10.5209/rev_REMA.2009.v22.n2.16263.

[28] A. Çeşmelioğlu and B. Rivière. Existence of a weak solution for the fully coupled Navier-Stokes/Darcy-transport problem. *Journal of Differential Equations*, 252(7):4138–4175, 2012. ISSN 0022-0396. DOI:10.1016/j.jde.2011.12.001.

[29] A. Çeşmelioğlu, V. Girault, and B. Rivière. Time-dependent coupling of Navier-Stokes and Darcy flows. *ESAIM: Mathematical Modelling and Numerical Analysis*, 47:539–554, 2013. ISSN 1290-3841. DOI:10.1051/m2an/2012034.

[30] T. Arbogast and H. L. Lehr. Homogenization of a Darcy-Stokes system modeling vuggy porous media. *Computational Geosciences*, 10(3):291–302, 2006. DOI:10.1007/s10596-006-9024-8.

[31] T. Arbogast and D. S. Brunson. A computational method for approximating a Darcy-Stokes system governing a vuggy porous medium. *Computational Geosciences*, 11(3):207–218, 2007. ISSN 1573-1499. DOI:10.1007/s10596-007-9043-0.

[32] J. M. Urquiza, D. N'Dri, A. Garon, and M. C. Delfour. Coupling Stokes and Darcy equations. *Applied Numerical Mathematics*, 58(5):525–538, 2008. ISSN 0168-9274. DOI:10.1016/j.apnum.2006.12.006.

[33] T. Arbogast and M. S. M. Gomez. A discretization and multigrid solver for a Darcy-Stokes system of three dimensional vuggy porous media. *Computational Geosciences*, 13(3):331–348, 2009. DOI:10.1007/s10596-008-9121-y.

[34] B. Rivière and I. Yotov. Locally Conservative Coupling of Stokes and Darcy Flows. *SIAM Journal on Numerical Analysis*, 42(5):1959–1977, 2005. DOI:10.1137/S0036142903427640.

[35] G. Kanschat and B. Rivière. A strongly conservative finite element method for the coupling of Stokes and Darcy flow. *Journal of Computational Physics*, 229(17):5933–5943, 2010. ISSN 0021-9991. DOI:10.1016/j.jcp.2010.04.021.

[36] V. Girault, G. Kanschat, and B. Rivière. Error analysis for a monolithic discretization of coupled Darcy and Stokes problems. *Journal of Numerical Mathematics*, 22(2):109–142, 2014. DOI:10.1515/jnma-2014-0005.

[37] M. R. Correa and A. F. D. Loula. A unified mixed formulation naturally coupling Stokes and Darcy flows. *Computer Methods in Applied Mechanics and Engineering*, 198(33–36):2710–2722, 2009. ISSN 0045-7825. DOI:10.1016/j.cma.2009.03.016.

[38] H. Egger and C. Waluga. A Hybrid Discontinuous Galerkin Method for Darcy-Stokes Problems. In R. Bank, M. Holst, O. Widlund, and J. Xu, editors, *Domain Decomposition Methods in Science and Engineering XX*, pages 663–670. Springer, Berlin, Heidelberg, 2013. ISBN 978-3-642-35275-1. DOI:10.1007/978-3-642-35275-1_79.

[39] S. Badia and J. Baiges. Adaptive Finite Element Simulation of Incompressible Flows by Hybrid Continuous-Discontinuous Galerkin Formulations. *SIAM Journal on Scientific Computing*, 35(1):A491–A516, 2013. DOI:10.1137/120880732.

[40] D. P. McKenzie. The Generation and Compaction of Partially Molten Rock. *Journal of Petrology*, 25(3):713–765, 1984. DOI:10.1093/petrology/25.3.713.

[41] D. A. Drew. Averaged Field Equations for Two-Phase Media. *Studies in Applied Mathematics*, 50(2):133–166, 1971. ISSN 1467-9590. DOI:10.1002/sapm1971502133.

[42] D. A. Drew and L. A. Segel. Averaged Equations for Two-Phase Flows. *Studies in Applied Mathematics*, 50(3):205–231, 1971. ISSN 1467-9590. DOI:10.1002/sapm1971503205.

[43] M. Spiegelman. Flow in deformable porous media. Part 1—Simple analysis. *Journal of Fluid Mechanics*, 247:17–38, 1993. ISSN 1469-7645. DOI:10.1017/S0022112093000369.

[44] M. Spiegelman. Flow in deformable porous media. Part 2—Numerical analysis – the relationship between shock waves and solitary waves. *Journal of Fluid Mechanics*, 247:39–63, 1993. ISSN 1469-7645. DOI:10.1017/S0022112093000370.

[45] D. Bercovici, Y. Ricard, and G. Schubert. A two-phase model for compaction and damage: 1. General Theory. *Journal of Geophysical Research: Solid Earth*, 106(B5):8887–8906, 2001. ISSN 2156-2202. DOI:10.1029/2000JB900430.

[46] T. Keller, D. A. May, and B. J. P. Kaus. Numerical modelling of magma dynamics coupled to tectonic deformation of lithosphere and crust. *Geophysical Journal International*, 195(3):1406–1442, 2013. DOI:10.1093/gji/ggt306.

[47] S. Rhebergen, G. N. Wells, A. J. Wathen, and R. F. Katz. Three-Field Block Preconditioners for Models of Coupled Magma/Mantle Dynamics. *SIAM Journal on Scientific Computing*, 37(5):A2270–A2294, 2015. DOI:10.1137/14099718X.

[48] H. Schmeling, A. Y. Babeyko, A. Enns, C. Faccenna, F. Funiciello, T. Gerya, G. J. Golabek, S. Grigull, B. J. P. Kaus, G. Morra, S. M. Schmalholz, and J. van Hunen. A benchmark comparison of spontaneous subduction models—Towards a free surface. *Physics of the Earth and Planetary Interiors*, 171(1–4):198–223, 2008. ISSN 0031-9201. DOI:10.1016/j.pepi.2008.06.028.

[49] T. Duretz, D. A. May, T. V. Gerya, and P. J. Tackley. Discretization errors and free surface stabilization in the finite difference and marker-in-cell method for applied geodynamics: A numerical study. *Geochemistry, Geophysics, Geosystems*, 12(7):1200–1225, 2011. ISSN 1525-2027. DOI:10.1029/2011GC003567.

[50] M. Furuichi and D. A. May. Implicit solution of the material transport in Stokes flow simulation: Toward thermal convection simulation surrounded by free surface. *Computer Physics Communications*, 192:1–11, 2015. ISSN 0010-4655. DOI:10.1016/j.cpc.2015.02.011.

[51] O. C. Zienkiewicz and R. L. Taylor. *The Finite Element Method*, volume 2: Solid Mechanics. Butterworth-Heinemann, Oxford, UK, 5th edition, 2000. ISBN 978-0-750-65055-7.

[52] L. Moresi, F. Dufour, and H.-B. Mühlhaus. A Lagrangian integration point finite element method for large deformation modeling of viscoelastic geomaterials. *Journal of Computational Physics*, 184(2):476–497, 2003. ISSN 0021-9991. DOI:10.1016/S0021-9991(02)00031-1.

[53] M. Thielmann, B. J. P. Kaus, and A. A. Popov. Lithospheric stresses in Rayleigh–Bénard convection: effects of a free surface and a viscoelastic Maxwell rheology. *Geophysical Journal International*, 203(3):2200–2219, 2015. DOI:10.1093/gji/ggv436.

[54] K. Terzaghi. *Arching in Ideal Soils*, pages 66–76. John Wiley & Sons, Inc., 1943. ISBN 978-0-47-017276-6. DOI:10.1002/9780470172766.ch5.

[55] M. S. Paterson and T. Wong. *Experimental Rock Deformation – The Brittle Field*. Springer, Berlin Heidelberg, 2nd edition, 2005. ISBN 978-3-540-24023-5. DOI:10.1007/b137431.

[56] S. A. F. Murrell. The theory of the propagation of elliptical Griffith cracks under various conditions of plane strain or plane stress: Parts II and III. *British Journal of Applied Physics*, 15(10):1211–1223, 1964. DOI:10.1088/0508-3443/15/10/309.

[57] M. Cai. Practical estimates of tensile strength and Hoek-Brown strength parameter m_i of brittle rocks. *Rock Mechanics and Rock Engineering*, 43(2):167–184, 2010. DOI:10.1007/s00603-009-0053-1.

[58] B. J. P. Kaus. Factors that control the angle of shear bands in geodynamic numerical models of brittle deformation. *Tectonophysics*, 484(1–4):36–47, 2010. ISSN 0040-1951. DOI:10.1016/j.tecto.2009.08.042.

[59] S. Mei, W. Bai, T. Hiraga, and D. L. Kohlstedt. Influence of melt on the creep behavior of olivine-basalt aggregates under hydrous conditions. *Earth and Planetary Science Letters*, 201 (3–4):491–507, 2002. ISSN 0012-821X. DOI:10.1016/S0012-821X(02)00745-8.

[60] P. B. Kelemen, G. Hirth, N. Shimizu, M. Spiegelman, and H. J. Dick. A review of melt migration processes in the adiabatically upwelling mantle beneath oceanic spreading ridges. *Philosophical Transactions of the Royal Society of London A: Mathematical, Physical and Engineering Sciences*, 355(1723):283–318, 1997. ISSN 1364-503X. DOI:10.1098/rsta.1997.0010.

[61] G. Simpson, M. Spiegelman, and M. I. Weinstein. A multiscale model of partial melts: 1. Effective equations. *Journal of Geophysical Research: Solid Earth*, 115(B4):B04410, 2010. DOI:10.1029/2009JB006375.

[62] H. Schmeling. Partial Melting and Melt Segregation in a Convecting Mantle. In N. Bagdassarov, D. Laporte, and A. B. Thompson, editors, *Physics and Chemistry of Partially Molten Rocks*, volume 11 of *Petrology and Structural Geology*, pages 141–178. Springer, Netherlands, 2000. ISBN 978-9-401-05774-5. DOI:10.1007/978-94-011-4016-4_5.

[63] M. Rabinowicz and J.-L. Vigneresse. Melt segregation under compaction and shear channeling: Application to granitic magma segregation in a continental crust. *Journal of Geophysical Research: Solid Earth*, 109(B4):B04407, 2004. ISSN 2156-2202. DOI:10.1029/2002JB002372.

[64] R. F. Katz, M. Spiegelman, and B. Holtzman. The dynamics of melt and shear localization in partially molten aggregates. *Nature*, 442(7103):676–679, 2006. DOI:10.1038/nature05039.

[65] H. Schmeling, J. P. Kruse, and G. Richard. Effective shear and bulk viscosity of partially molten rock based on elastic moduli theory of a fluid filled poroelastic medium. *Geophysical Journal International*, 190(3):1571–1578, 2012. DOI:10.1111/j.1365-246X.2012.05596.x.

[66] D. Giordano, J. K. Russell, and D. B. Dingwell. Viscosity of magmatic liquids: A model. *Earth and Planetary Science Letters*, 271(1–4):123–134, 2008. ISSN 0012-821X. DOI:10.1016/j.epsl.2008.03.038.

[67] K.-U. Hess and D. B. Dingwell. Viscosities of hydrous leucogranitic melts: A non-Arrhenian model. *American Mineralogist*, 81(9–10):1297–1300, 1996. ISSN 1945-3027.

[68] F. Vetere, H. Behrens, J. A. Schuessler, F. Holtz, V. Misiti, and L. Borchers. Viscosity of andesite melts and its implication for magma mixing prior to Unzen 1991–1995 eruption. *Journal of Volcanology and Geothermal Research*, 175(1–2):208–217, 2008. ISSN 0377-0273. DOI:10.1016/j.jvolgeores.2008.03.028.

[69] U. H. Faul. Permeability of partially molten upper mantle rocks from experiments and percolation theory. *Journal of Geophysical Research: Solid Earth*, 102(B5):10299–10311, 1997. ISSN 2156-2202. DOI:10.1029/96JB03460.

[70] H. Schmeling. Dynamic models of continental rifting with melt generation. *Tectonophysics*, 480(1–4):33–47, 2010. ISSN 0040-1951. DOI:10.1016/j.tecto.2009.09.005.

[71] A. Jalalh. Compressibility of porous rocks: Part II. New relationships. *Acta Geophysica*, 54 (4):399–412, 2006. DOI:10.2478/s11600-006-0029-4.

[72] J. A. D. Connolly and Y. Y. Podladchikov. Compaction-driven fluid flow in viscoelastic rock. *Geodinamica Acta*, 11(2–3):55–84, 1998. DOI:10.1080/09853111.1998.11105311.

[73] S. Rhebergen, G. N. Wells, R. F. Katz, and A. J. Wathen. Analysis of block preconditioners for models of coupled magma/mantle dynamics. *SIAM Journal on Scientific Computing*, 36 (4):A1960–A1977, 2014. DOI:10.1137/130946678.

[74] D. N. Arnold, F. Brezzi, and M. Fortin. A stable finite element for the Stokes equations. *Calcolo*, 21(4):337–344, 1984. DOI:10.1007/BF02576171.

[75] M. Feistauer. *Mathematical Methods in Fluid Dynamics*. Chapman and Hall/CRC, 1993. ISBN 978-0-582-20988-6.

[76] C. Burstedde, O. Ghattas, G. Stadler, T. Tu, and L. C. Wilcox. Parallel scalable adjoint-based adaptive solution of variable-viscosity Stokes flow problems. *Computer Methods in Applied Mechanics and Engineering*, 198(21–26):1691–1700, 2009. DOI:10.1016/j.cma.2008.12.015.

[77] F. Brezzi and M. Fortin. *Mixed and Hybrid Finite Element Methods*. Springer, New York, NY, USA, 1991. ISBN 978-3-540-97582-3.

[78] J. Dannberg and T. Heister. 3D Compressible Melt Transport with Mesh Adaptivity. Submitted, 2015.

[79] V. John and G. Matthies. Higher-order finite element discretizations in a benchmark problem for incompressible flows. *International Journal for Numerical Methods in Fluids*, 37(8): 885–903, 2001. ISSN 1097-0363. DOI:10.1002/fld.195.

[80] R. Codina. A stabilized finite element method for generalized stationary incompressible flows. *Computer Methods in Applied Mechanics and Engineering*, 190(20–21):2681–2706, 2001. ISSN 0045-7825. DOI:10.1016/S0045-7825(00)00260-7.

[81] A. M. Maniatty, Y. Liu, O. Klaas, and M. S. Shephard. Stabilized finite element method for viscoplastic flow: formulation and a simple progressive solution strategy. *Computer Methods in Applied Mechanics and Engineering*, 190(35–36):4609–4625, 2001. ISSN 0045-7825. DOI:10.1016/S0045-7825(00)00346-7.

[82] T. Gelhard, G. Lube, M. A. Olshanskii, and J.-H. Starcke. Stabilized finite element schemes with LBB-stable elements for incompressible flows. *Journal of Computational and Applied Mathematics*, 177(2):243–267, 2005. ISSN 0377-0427. DOI:10.1016/j.cam.2004.09.017.

[83] D. A. May, J. Brown, and L. Le Pourhiet. pTatin3D: High-Performance Methods for Long-Term Lithospheric Dynamics. In *SC14: International Conference for High Performance Computing, Networking, Storage and Analysis*, pages 274–284, 2014. ISBN 978-1-4799-5500-8. DOI:10.1109/SC.2014.28.

[84] H. C. Elman, D. J. Silvester, and A. J. Wathen. *Finite Elements and Fast Iterative Solvers*. Numerical Mathematics and Scientific Computation. Oxford University Press, UK, 2006. ISBN 978-0-198-52867-8.

[85] B. J. P. Kaus, C. Steedman, and T. W. Becker. From passive continental margin to mountain belt: Insights from analytical and numerical models and application to Taiwan. *Physics of the Earth and Planetary Interiors*, 171(1–4):235–251, 2008. DOI:10.1016/j.pepi.2008.06.015.

[86] R. S. Lehmann, M. Lukáčová-Medvid'ová, B. J. P. Kaus, and A. A. Popov. Comparison of continuous and discontinuous Galerkin approaches for variable-viscosity Stokes flow. *ZAMM – Journal of Applied Mathematics and Mechanics/Zeitschrift für Angewandte Mathematik und Mechanik*, 2015. ISSN 1521-4001. DOI:10.1002/zamm.201400274.

[87] D. N. Arnold and J. Qin. Quadratic Velocity/Linear Pressure Stokes Elements. In R. Vichnevetsky, D. Knight, and G. Richter, editors, *Advances in Computer Methods for Partial Differential Equations VII*, pages 28–34, New Jersey, USA, 1992. IMACS.

[88] E. Burman and A. Linke. Stabilized finite element schemes for incompressible flow using Scott-Vogelius elements. *Applied Numerical Mathematics*, 58(11):1704–1719, 2008. ISSN 0168-9274. DOI:10.1016/j.apnum.2007.11.001.

[89] R. Verfürth. Error estimates for a mixed finite element approximation of the Stokes equations. *ESAIM: Mathematical Modelling and Numerical Analysis - Modélisation Mathématique et Analyse Numérique*, 18(2):175–182, 1984. ISSN 0764-583X.

[90] D. Braess. *Finite elements: Theory, fast solvers, and applications in solid mechanics*. Cambridge University Press, 3rd edition, 2007. ISBN 978-0-521-70518-9. DOI:10.1017/CBO9780511618635.

[91] M. Larson and F. Bengzon. *The Finite Element Method: Theory, Implementation and Applications*. Springer, 2013. ISBN 978-3-642-33286-9.

[92] M. Bercovier and O. Pironneau. Error estimates for finite element method solution of the Stokes problem in the primitive variables. *Numerische Mathematik*, 33(2):211–224, 1979. ISSN 0945-3245. DOI:10.1007/BF01399555.

[93] R. Barrett, M. Berry, T. F. Chan, J. Demmel, J. Donato, J. Dongarra, V. Eijkhout, R. Pozo, C. Romine, and H. van der Horst. *Templates for the Solution of Linear Systems: Building Blocks for Iterative Methods*. SIAM, Philadelphia, PA, USA, 1994. ISBN 978-0-898-71328-2.

[94] M. Benzi. Preconditioning Techniques for Large Linear Systems: A Survey. *Journal of Computational Physics*, 182(2):418–477, 2002. ISSN 0021-9991. DOI:10.1006/jcph.2002.7176.

[95] A. Meister. *Numerik linearer Gleichungssysteme*. Springer, 5th edition, 2011. ISBN 978-3-658-07199-8. DOI:10.1007/978-3-658-07200-1.

[96] I. S. Duff. MA57—a Code for the Solution of Sparse Symmetric Definite and Indefinite Systems. *ACM Transactions on Mathematical Software*, 30(2):118–144, 2004. ISSN 0098-3500. DOI:10.1145/992200.992202.

[97] L. P. Franca, S. L. Frey, and T. J. R. Hughes. Stabilized finite element methods: I. Application to the advective-diffusive model. *Computer Methods in Applied Mechanics and Engineering*, 95 (2):253–276, 1992. ISSN 0045-7825. DOI:10.1016/0045-7825(92)90143-8.

[98] J. E. Welch, F. H. Harlow, J. P. Shannon, and B. J. Daly. The MAC Method – A Computing Technique for Solving Viscous, Incompressible, Transient Fluid-Flow Problems Involving Free Surfaces. Technical Report LA-3425, Los Alamos Scientific Laboratory, University of California, 1965.

[99] F. H. Harlow and J. E. Welch. Numerical Calculation of Time-Dependent Viscous Incompressible Flow of Fluid with Free Surface. *Physics of Fluids*, 8(12):2182, 1965. DOI:10.1063/1.1761178.

[100] V. Girault. A Combined Finite Element and Marker and Cell Method for Solving Navier-Stokes Equations. *Numerische Mathematik*, 26(1):39–59, 1976. ISSN 0029-599X. DOI:10.1007/BF01396565.

[101] S. McKee, M.F. Tomé, V.G. Ferreira, J.A. Cuminato, A. Castelo, F.S. Sousa, and N. Mangiavacchi. The MAC method. *Computers & Fluids*, 37(8):907–930, 2008. ISSN 0045-7930. DOI:10.1016/j.compfluid.2007.10.006.

[102] G. Kanschat. Divergence-free Discontinuous Galerkin Schemes for the Stokes Equations and the MAC Scheme. *International Journal for Numerical Methods in Fluids*, 56(7):941–950, 2008. DOI:10.1002/fld.1566.

[103] T.V. Gerya. Plume-induced crustal convection: 3D thermomechanical model and implications for the origin of novae and coronae on Venus. *Earth and Planetary Science Letters*, 391: 183–192, 2014. ISSN 0012-821X. DOI:10.1016/j.epsl.2014.02.005.

[104] T. S. Baumann and B. J. P. Kaus. Geodynamic inversion to constrain the non-linear rheology of the lithosphere. *Geophysical Journal International*, 202(2):1289–1316, 2015. DOI:10.1093/gji/ggv201.

[105] M. Dabrowski, M. Krotkiewski, and D. W. Schmid. MILAMIN: MATLAB-based finite element method solver for large problems. *Geochemistry, Geophysics, Geosystems*, 9(4), 2008. ISSN 1525-2027. DOI:10.1029/2007GC001719.

[106] F. Crameri and Boris J. P. Kaus. Parameters that control lithospheric-scale thermal localization on terrestrial planets. *Geophysical Research Letters*, 37(9):L09308, 2010. ISSN 1944-8007. DOI:10.1029/2010GL042921.

[107] M. Thielmann and B. J. P. Kaus. Shear heating induced lithospheric-scale localization: Does it result in subduction? *Earth and Planetary Science Letters*, 359–360:1–13, 2012. DOI:10.1016/j.epsl.2012.10.002.

[108] V. Lemiale, H.-B. Mühlhaus, L. Moresi, and J. Stafford. Shear banding analysis of plastic models formulated for incompressible viscous flows. *Physics of the Earth and Planetary Interiors*, 171(1–4):177–186, 2008. ISSN 0031-9201. DOI:10.1016/j.pepi.2008.07.038. Recent Advances in Computational Geodynamics: Theory, Numerics and Applications.

[109] A. A. Popov and S. V. Sobolev. SLIM3D: A Tool for Three-dimensional Thermomechanical Modeling of Lithospheric Deformation with Elasto-visco-plastic Rheology. *Physics of the Earth and Planetary Interiors*, 171(1–4):55–75, 2008. DOI:10.1016/j.pepi.2008.03.007.

[110] Yury Mishin. *Adaptive multiresolution methods for problems of computational geodynamics*. PhD thesis, ETH Zürich, 2011.

[111] D. L. Turcotte and G. Schubert. *Geodynamics*. Cambridge University Press, 2nd edition, 2002. ISBN 978-0-521-66624-4.

[112] V. Barcilon and F. M. Richter. Nonlinear waves in compacting media. *Journal of Fluid Mechanics*, 164:429–448, 1986.

[113] V. Barcilon and O. M. Lovera. Solitary waves in magma dynamics. *Journal of Fluid Mechanics*, 204:121–133, 1989. ISSN 1469-7645. DOI:10.1017/S0022112089001680.

[114] G. Simpson and M. Spiegelman. Solitary Wave Benchmarks in Magma Dynamics. *Journal of Scientific Computing*, 49(3):268–290, 2011. DOI:10.1007/s10915-011-9461-y.

[115] G. C. Richard, S. Kanjilal, and H. Schmeling. Solitary-waves in geophysical two-phase viscous media: A semi-analytical solution. *Physics of the Earth and Planetary Interiors*, 198–199:61–66, 2012. ISSN 0031-9201. DOI:10.1016/j.pepi.2012.03.001.

[116] F. Crameri, H. Schmeling, G. J. Golabek, T. Duretz, R. Orendt, S. J. H. Buiter, D. A. May, B. J. P. Kaus, T. V. Gerya, and P. J. Tackley. A comparison of numerical surface topography calculations in geodynamic modelling: An evaluation of the 'sticky air' method. *Geophysical Journal International*, 189(1):38–54, 2012. DOI:10.1111/j.1365-246X.2012.05388.x.

[117] M. Thielmann, D. A. May, and B. J. P. Kaus. Discretization Errors in the Hybrid Finite Element Particle-in-cell Method. *Pure and Applied Geophysics*, 171(9):2165–2184, 2014. ISSN 0033-4553. DOI:10.1007/s00024-014-0808-9.

[118] T. E. Johnson, M. Brown, B. J. P. Kaus, and J. A. van Tongeren. Delamination and recycling of Archaean crust caused by gravitational instabilities. *Nature Geoscience*, 7(1):47–52, 2014. DOI:10.1038/ngeo2019.

[119] A. E. Pusok and B. J. P. Kaus. Development of topography in 3-D continental-collision models. *Geochemistry, Geophysics, Geosystems*, 16(5):1378–1400, 2015. ISSN 1525-2027. DOI: 10.1002/2015GC005732.

[120] G. Reuber, B. J. P. Kaus, S. M. Schmalholz, and R. White. Non-lithostatic pressure during subduction and collision and the formation of HP/UHP rocks. Submitted, 2016.

CHAPTER 4

A Parameter Study on Lithospheric Scale Melt Migration

4.1 Introduction

With approximately 500 million people living in or near volcanically active regions it is of utmost importance to improve our understanding of magmatic processes. Although there has been a lot of research in the last decades, many questions remain essentially unanswered. How does melt rise through the Earth's mantle and crust? In what kind of physical regimes does it reach the surface? How much reaches the surface? How do plumbing systems of volcanoes work? How is the melt migration process affected by large scale tectonic deformation?

Numerical modelling has been among the tools to approach magmatic systems since the 1980s. One of the features described in the work by McKenzie [1] is the existence of finite-amplitude one-dimensional solitary waves. The propagation of solitary waves might contribute to the episodic behavior observed in melt migration [2, 3]. They have been studied analytically and numerically [3–6]. Analytic solutions serve as benchmarks for numerical methods, see, e.g., [7, 8].

Connolly and Podladchikov [9] considered 2D solitary waves in a viscoelastic host rock. in a later study [10] they added a parameterized plastic decompaction failure effect yielding elongated melt "tubes" instead of spherical waves. Other studies have covered, e.g., (percolative) channelling instabilities [11, 12] or dikes that arise under tensile stress [13].

Yet, all of these models have in common that they consider particular deformation modes and, hence, *a priori* prescribe the deformation mode in the

respective model, i.e., diapiric, percolative, diking.

Of course, with such modelling constraints it is not possible to recover all phases of the melt propagation through the Earth's mantle and crust. The pressure-temperature regime in the mantle is likely to favour viscous and diapiric deformation modes, while we expect narrow structures and plastic failure in shallower (crustal) depths, i.e., at lower temperature and pressure. Also, we know from geological observations that significant amounts of magma crystallize in (large) bodies in the crust. Some of these batholiths get exposed by later mountain-building processes and erosion and are well studied.

An ideal mathematical model of the physics involved in the process would self-consistently reproduce the different deformation modes at all scales, incorporate phase changes (melting and crystallization), and yield results that match geological and geophysical observations. However, we decided not to take phase changes into account for this work to focus on the mechanical system. Instead we refer to [14, 15] for ways to include parameterized phase changes.

Based on the work by Keller et al. [7] we present in this chapter the first broad parameter study of lithospheric scale melt migration setups using realistic (temperature-dependent) visco-elasto-plastic rheologies in a coupled Stokes/Darcy system. We apply a stable numerical method as described in chapter 3. Varying different physical parameters we investigate key factors in driving efficient melt ascent through the Earth's upper mantle and crust.

In the following section 4.2 we briefly recap the governing equations that were derived in more detail in chapter 3. In section 4.3 we describe our reference model and list the physical parameters that we varied for the lithospheric scale study. Section 4.4 is destined to present the observations from the numerical experiments that we discuss in section 4.5. Finally, we conclude and summarize our results in section 4.6.

4.2 Governing Equations

In section 4.2.1 we repeat the mechanical system that has already been derived in detail in section 3.2 and then describe in section 4.2.2 how we handle the energy conservation in a separate step. The details of the material properties are provided in section 4.2.3.

4.2.1 Conservation of Momentum and Mass

In this section we briefly recap the governing equations that control the system of coupled magma and lithosphere dynamics as described in full detail in section 3.2, see also [7].

$$-\nabla\cdot\left(\eta_{\text{eff}}\left(\nabla\boldsymbol{v}_{\text{s}}+(\nabla\boldsymbol{v}_{\text{s}})^{\mathsf{T}}\right)-\frac{2}{3}\eta_{\text{eff}}\nabla\cdot\boldsymbol{v}_{\text{s}}\boldsymbol{I}_d\right)+\nabla p_{\text{f}}+\nabla p_{\text{c}}= \\ =-\bar{\varrho}\boldsymbol{g}+\nabla\cdot\chi_\tau\tilde{\boldsymbol{\tau}}^o_{\text{s}}, \tag{4.1a}$$

$$-\nabla\cdot\boldsymbol{v}_{\text{s}}+\nabla\cdot K_D\nabla p_{\text{f}}=-\nabla\cdot K_D\varrho_{\text{f}}\boldsymbol{g} \tag{4.1b}$$

$$-\nabla\cdot\boldsymbol{v}_{\text{s}}-\frac{p_{\text{c}}}{\zeta_{\text{eff}}}=-\frac{\chi_p\Delta p^o}{\zeta_{\text{eff}}}, \tag{4.1c}$$

$$\frac{\mathrm{D}_{\text{s}}\varphi}{\mathrm{D}t}-(1-\varphi)\nabla\cdot\boldsymbol{v}_{\text{s}}=0. \tag{4.2}$$

The effective viscosities η_{eff} and ζ_{eff} are given by (3.23) and (3.25), respectively. The system is complemented by an initial condition for the porosity $\varphi(t_0)=\varphi_0$ and the following boundary conditions, see [16]. Let the boundary $\partial\Omega=\Gamma_D\cup\Gamma_N$, where $\Gamma_D\cap\Gamma_N=\emptyset$, and denote the outward unit normal vector on $\partial\Omega$ as $\boldsymbol{n}$,

$$\boldsymbol{v}_{\text{s}}=\boldsymbol{b}_D \qquad \text{on } \Gamma_D, \tag{4.3a}$$

$$\boldsymbol{\tau}_{\text{s}}\boldsymbol{n}-(p_{\text{f}}+p_{\text{c}})\,\boldsymbol{n}=\boldsymbol{b}_N \qquad \text{on } \Gamma_N, \tag{4.3b}$$

$$-K_D(\nabla p_{\text{f}}+\varrho_{\text{f}}\boldsymbol{g})\cdot\boldsymbol{n}=0 \qquad \text{on } \partial\Omega, \tag{4.3c}$$

where $\boldsymbol{b}_D:\Gamma_D\to\mathbf{R}^d$, $\boldsymbol{b}_N:\Gamma_N\to\mathbf{R}^d$ are given boundary data.

4.2.2 Conservation of Energy

The conservation of energy is enforced by the following equation,

$$\bar{\varrho}c_p\frac{\mathrm{D}_{\text{s}}T}{\mathrm{D}t}-\nabla\cdot(k\nabla T)=H, \tag{4.4}$$

where $\bar{\varrho}$ denotes porosity-weighted density average, c_p specific heat capacity, T temperature, k conductivity, and H source terms such as radiogenic, shear or adiabatic (de)compression heating. For simplification we neglect the latter effects in this study. This still captures temperature effects on, particularly, density and viscosity. Bercovici et al. [17] provide a detailed derivation of the energy equation for the two-phase system.

The advection is explicitly handled on Lagrangian markers, see setion 3.3.6. The remaining energy equation is solved with a standard second order finite element method (as for velocity we use continuous, piecewise biquadratic shape functions) that we do not describe in detail. The temperature is fixed at the top and bottom boundary of the domain, on side boundaries we enforce zero-flux.

4.2.3 Material Properties

In this section we describe the material properties. For the shear viscosity η we apply diffusion and dislocation creep laws as presented in Table 4.2,

$$\tau_{\mathrm{II}} = 2\eta\dot{\varepsilon}_{\mathrm{II}}, \tag{4.5a}$$

$$\dot{\varepsilon}_{\mathrm{II}} = A\tau_{\mathrm{II}}^{n} d_0^{-p^*} c_{\mathrm{OH}}^{r} \exp(-(E - pV)/\mathrm{R}T), \tag{4.5b}$$

where A is a constant, d_0 denotes grain size, c_{OH} water fugacity, E activation energy, V activation volume, and R the universal gas constant, see [18]. For diffusion creep $n = 1$, for dislocation creep $p^* = 0$. The compaction and fluid viscosities follow the description in section 3.2.5, analogously the permeability, plasticity parameters and elastic moduli, cp. Table 4.1.

Different from the previous chapter, the solid density is chosen to be temperature-dependent as follows,

$$\varrho = \varrho_0(1 - \alpha_v(T - T_0)), \tag{4.6}$$

where ϱ_0 is a reference density at reference temperature T_0 that corresponds to the considered phase (upper crust, lower crust, mantle), and α_v is thermal expansivity.

The specific heat c_p and the conductivity k are chosen to be constant for all phases, see Table 4.1 for their values.

4.3 Study Setup

We perform a set of numerical experiments to explore how the magma migrates in different physical regimes. First, we describe our reference setup, second, we name the parameters that we varied. Furthermore, in section 4.3.2 we provide a detailed description of the evolution of the reference setup followed by simulations in which we systematically vary the model parameters.

4.3.1 Parameter Ranges

Reference Setup The initial geometry is identical for all lithospheric scale simulations, i.e., we start with a domain that is 160 km deep and 240 km wide in (x, z) coordinates. The top 30 km are assigned crustal phases (upper and lower crust, 15 km each) and corresponding rheologies, see below. The lower 130 km represent lithospheric mantle rocks.

We apply no external deformation in the reference setup (zero background strainrate). The geothermal gradient is initialized at $15\,\mathrm{K\,km^{-1}}$. The surface

Table 4.1: Parameters for the presented lithospheric scale study.

Symbol	Name	Value
ϱ_{UC}	reference density (upper crust)	$2.70 \times 10^3\,\mathrm{kg\,m^{-3}}$
ϱ_{LC}	reference density (lower crust)	$2.90 \times 10^3\,\mathrm{kg\,m^{-3}}$
ϱ_{MA}	reference density (mantle)	$3.25 \times 10^3\,\mathrm{kg\,m^{-3}}$
ϱ_{f}	fluid density	$2.50 \times 10^3\,\mathrm{kg\,m^{-3}}$
η_{f}	fluid viscosity	$10^2\,\mathrm{Pa\,s}$
κ_0	reference permeability	$10^{-8}\,\mathrm{m^2}$
K_0	reference pore modulus	1 GPa
G	reference shear modulus	50 GPa
C	cohesion	40 MPa
ϕ	friction angle	30°
σ_T	tensile strength	10 MPa
T_0	reference temperature	293 K
T_s	surface temperature	293 K
T_b	bottom temperature	1573 K
α	melt weakening parameter	27
k	conductivity	$3\,\mathrm{W\,m^{-1}K^{-1}}$
c_p	specific heat capacity	$1.05 \times 10^3\,\mathrm{J\,kg^{-1}K^{-1}}$
α_v	thermal expansivity	$3 \times 10^{-5}\,\mathrm{K^{-1}}$
R	gas constant	$8.3145\,\mathrm{Jmol^{-1}K^{-1}}$
g	gravitational acceleration	$9.81\,\mathrm{m\,s^{-2}}$

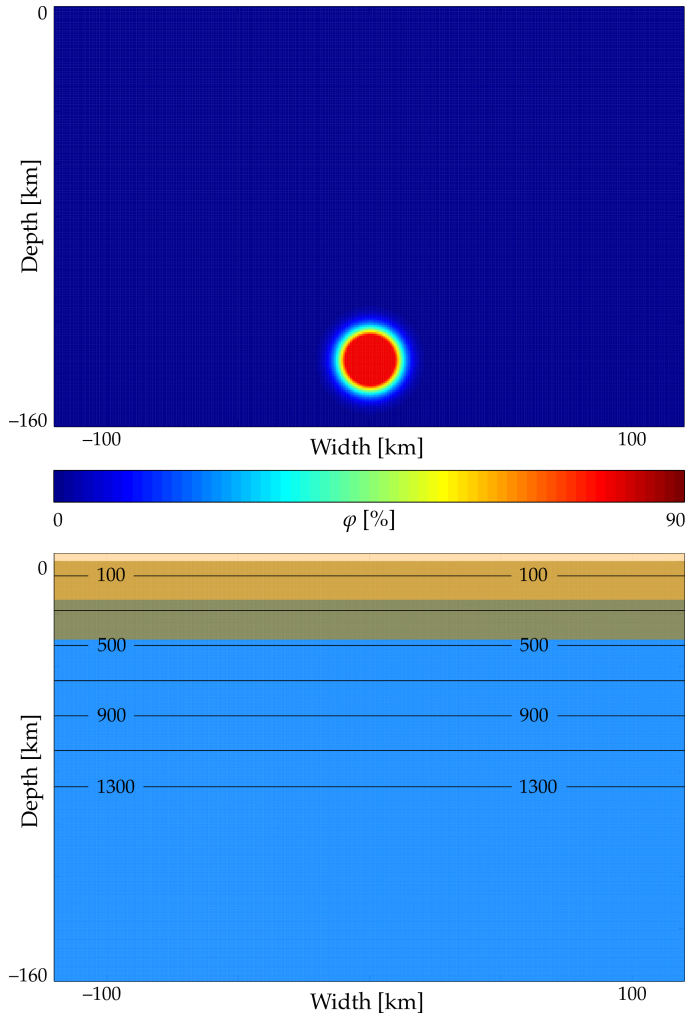

Figure 4.1: Reference setup with quartzitic upper and lower crust, dry dislocation and diffusion creep mantle rheology, geothermal gradient of $\partial_z T = 15\,\mathrm{K\,km^{-1}}$, magmatic pulse with 20 km diameter and up to 80 % porosity. Top: Initial porosity field. Bottom: Compositional phases and temperature contours at 100 °C, 300 °C, …, 1300 °C.

and bottom temperatures are fixed at 20 and 1300 °C, respectively. A circular Gaussian melt pulse is introduced horizontally centered at a depth of 135 km with an upper cut-off at 80 %. This roughly approximates a mantle wedge plume of hydrated mantle material as investigated in, e.g., [19–21].

For the reference setup, we choose the creep viscosities presented in the top part of Table 4.2. For the crustal phases we apply quartzite dislocation creep, for the mantle we harmonically average dry olivine dislocation and diffusion creep viscosities being denoted as subscripts disl and diff, respectively.

Parameter Variations The upper crust is assumed to be quartzitic in all simulations. The lower crust is either made up of quartzite or mafic granulite [22]. The mantle is either described by dry olivine dislocation creep only, or by dry or wet olivine dislocation and diffusion creep [18]. This yields a set of 12 different rheological setups.

Apart from the rheology we vary the initial geothermal gradient, the extent of the magma pulse and the background strainrate as follows. The geothermal gradient takes on the values 10, 15 and 20 $\mathrm{K\,km^{-1}}$. In most contintental regions, the geothermal gradient is steeper than this range for shallow depths but flattens with depth. Hence, the examined range roughly corresponds to averaged continental geotherms. In volcanically active zones the geothermal gradient may be locally significantly steeper, see, e.g., [23, ch. 3], [24, ch. 14], [25].

The background strainrate is either zero or $10^{-15}\,\mathrm{s^{-1}}$ as laterally extensional or compressional strain rate mimicking deformational tectonic regimes. In the deformational cases we apply a vertical velocity at the bottom boundary to balance the volume change of the domain. The top boundary can deform following a stress-free condition. Furthermore, the size of the initial melt pulse (diameter) is 20 km in most setups but reduced to 10 and 5 km for some simulations.

The prescribed fluid viscosity $\eta_f = 10^2$ Pa s corresponds to a basaltic melt. At the end of section 4.4 we present simulation results using an increased fluid viscosity of $\eta_f = 10^{10}$ Pa s corresponding to a melt of more felsic composition.

4.3.2 Evolution of Reference Setup

In this section we describe in detail the evolution of the reference setup and present figures of the porosity field, the viscoplastic shear viscosity, the strainrate and the compositional field (with temperature contours). We split the following description into three parts where major evolution takes place in the mantle, the lower crust and the upper crust, respectively, see Figures 4.2 and 4.3.

Table 4.2: Creep rheology flow laws as used in the numerical simulations, $\dot{\varepsilon} = A\tau^n d_0^{-p^*} c_{\mathrm{OH}}^r \exp(-(E-pV)/RT)$ [18], where r is non-zero only for wet olivine diffusion creep ($c_{\mathrm{OH}} = 10^3$ H/10^6 Si, $r = 0.8$). Furthermore, A is a constant, d_0 denotes grain size, c_{OH} water fugacity, E activation energy, V activation volume, and R $= 8.3145\,\mathrm{J mol^{-1} K^{-1}}$ the universal gas constant, see [18]. The abbreviations in the first column represent the upper crust (UC), lower crust (LC) and the mantle (MA).

Phase	Flow Law	A [MPa^{-n} s^{-1}]	n	d_0 [µm]	p^*	E [J mol^{-1}]	V [m^3 mol^{-1}]
UC	Quartzite (qz) [22]	6.7×10^{-6}	2.4	—	0	156×10^3	0
LC	Quartzite [22]	6.7×10^{-6}	2.4	—	0	156×10^3	0
$\mathrm{MA_{disl}}$	Dry Olivine ($\mathrm{do_{disl}}$) [18]	1.1×10^5	1.5	—	0	530×10^3	15×10^{-6}
$\mathrm{MA_{diff}}$	Dry Olivine ($\mathrm{do_{diff}}$) [18]	1.5×10^9	1.0	10×10^3	3	375×10^3	5×10^{-6}
	Mafic Granulite (mg) [22]	1.4×10^4	4.2	—	0	445×10^3	0
	Wet Olivine ($\mathrm{wo_{disl}}$) [18]	1.6×10^3	3.5	—	0	520×10^3	22×10^{-6}
	Wet Olivine ($\mathrm{wo_{diff}}$) [18]	2.5×10^7	1.0	10×10^3	3	375×10^3	10×10^{-6}

Mantle Initially, the melt pulse rises at a velocity of more than 1 m/yr and flattens. After roughly 50 kyrs it splits into two branches at a depth of about 70 km and the vertical velocity drops down to 20 to 30 cm/yr. Starting at about 100 kyrs we observe strain localization in the upper crust. The maximum porosity in the two branches gradually decreases to about 60 % while becoming narrower and reaching the lower crust at 30 km depth after approximately 150 kyrs.

Lower Crust While rising towards the upper crust the two branches widen again and tend to converge. The maximum vertical velocity after 250 kyrs is around 5 cm/yr. The strain localization in the upper crust intensifies locally leading to lower shear viscosity. The pulse reaches the upper crust after roughly 300 kyrs.

Upper Crust In the upper crust the two branches slightly diverge and narrow again leaving behind significant amounts of melt in reservoirs in and below the lower crust. They reach the surface through very small channel-like structures that seem to develop where the viscosity in the upper crust has dropped locally due to previous strain localization. The pulse reaches the surface after 420 kyrs.

4.4 Experiments

In this section we describe the effects that we observe when varying different parameters: the geothermal gradient, the rheology, the size of the magmatic pulse, the background strainrate, and the fluid viscosity.

4.4.1 Geothermal Gradient

We performed the simulations with initial geothermal gradients $\partial_z T$ of 10, 15 and 20 K km^{-1}. This leads to temperatures of 320, 470 and 620 °C at the bottom of the crust, respectively. The maximum temperature of 1300 °C is reached at a depth of 128, 85 and 64 km, respectively.

The pulse starts rising in a diapiric manner but starts diverging into two branches at a depth that correlates to the initial geothermal gradient. For $\partial_z T = 10, 15, 20$ K km^{-1} the localization starts in a depth of 110, 70 and 50 km, respectively. We observe the melt pulse to split along the 1100 °C isotherm, cp. Figure 4.3.

The geothermal gradient also affects how fast the magma rises towards the lower crust. For a geothermal gradient of $\partial_z T = 10$ K km^{-1} and zero background strainrate this translates into approximately 350, 400 and 450 kyrs for wet, dry dislocation, dry dislocation and diffusion creep, respectively.

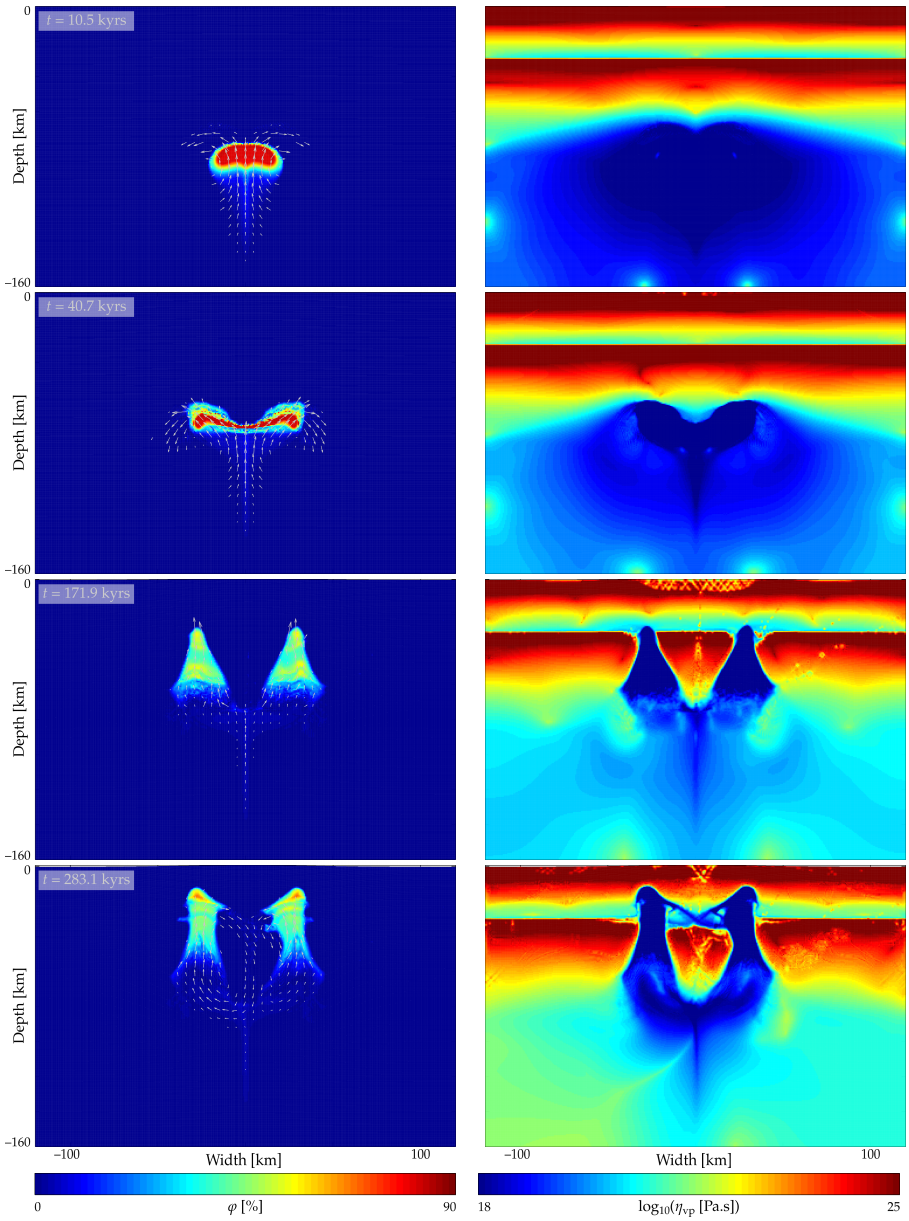
t = 10.5 kyrs
t = 40.7 kyrs
t = 171.9 kyrs
t = 283.1 kyrs
Depth [km]
0
−160
−100
100
Width [km]
0
φ [%]
90
18
log10(ηvp [Pa.s])
25

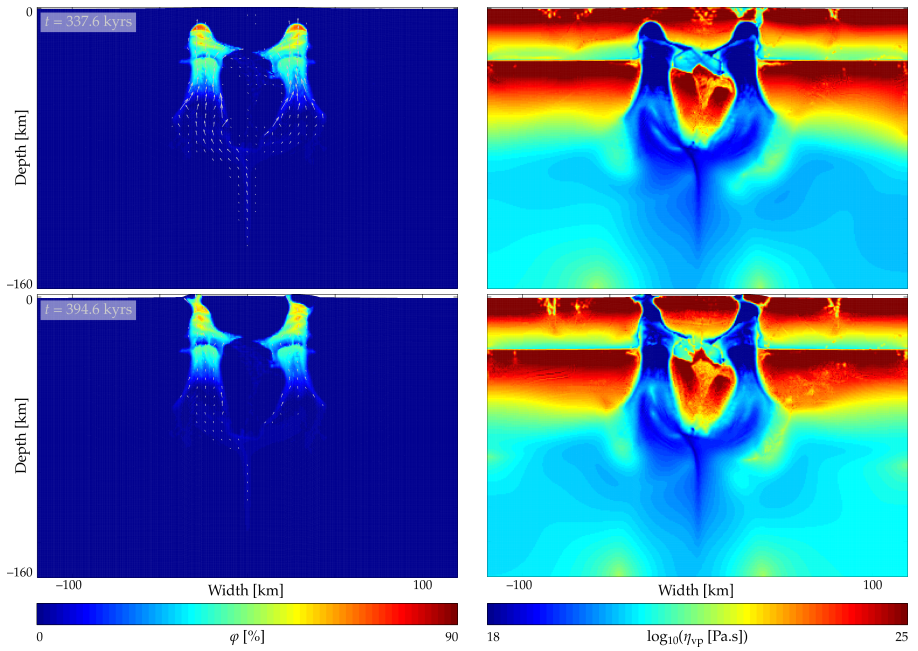

Figure 4.2: Porosity field (with fluid velocity arrows) and viscoplastic shear viscosity snapshots from the reference setup. The melt pulse first rises rapidly and gradually flattens. It splits into two branches at a depth of about 70 km. The two branches become narrower and reach the lower crust (30 km depth) after approximately 150 kyrs.

While rising towards the upper crust the two branches widen again and tend to converge. The strain localization in the upper crust intensifies leading to lower shear viscosity locally.

In the upper crust the two branches slightly diverge and narrow again leaving behind significant amounts of melt in reservoirs in and below the lower crust. They reach the surface through very small channel-like structures that seem to develop where the viscosity in the upper crust has dropped locally due to previous strain localization.

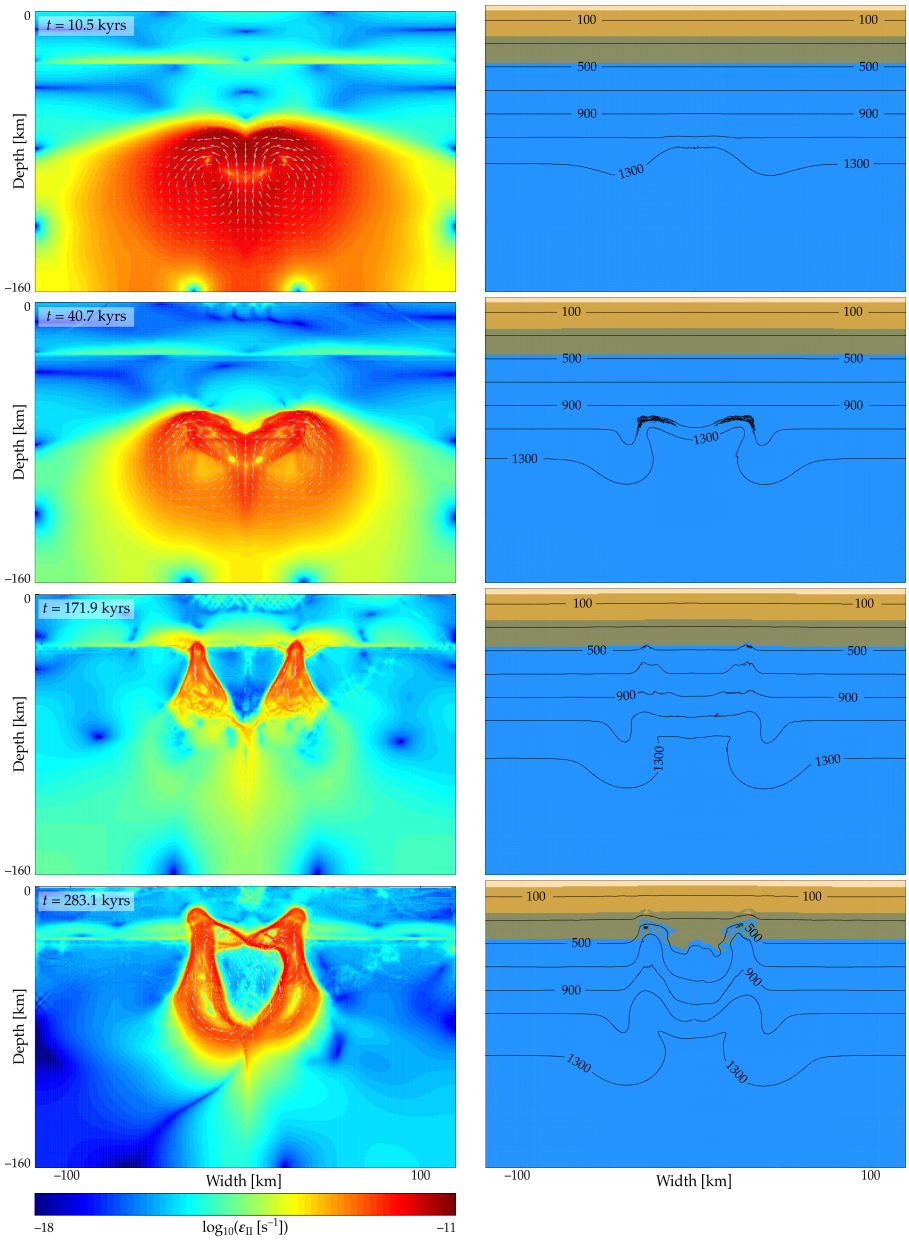
t = 10.5 kyrs
t = 40.7 kyrs
t = 171.9 kyrs
t = 283.1 kyrs
Depth [km]
0
−160
100
500
900
1300
−100
Width [km]
100
−18
log10(εII [s−1])
−11

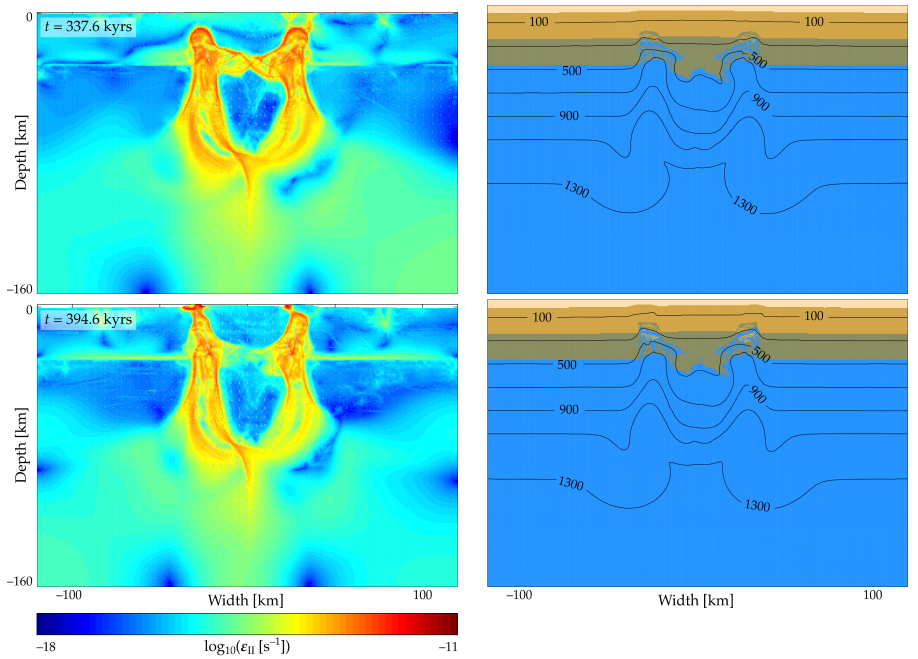

Figure 4.3: (Square root of) Strain rate invariant (with solid velocity arrows) and compositional field (with temperature contours in °C) from reference setup. Starting at about 100 kyrs we observe strain localization in the upper crust (top center of domain).

Regions of higher porosity lead to increased velocities leading to larger strainrate. Towards the end of the simulation the strainrate more and more localizes into narrow bands.

When the pulse reaches the crust it also brings mantle material up, some of it even to upper crustal depths. The temperature contours follow the branched pulse. This increases the temperature at the base of the crust from 470 °C to more than 700 °C.

For a steeper geothermal gradient, i.e., $\partial_z T = 15\,\mathrm{K\,km^{-1}}$, and zero background strainrate the difference reduces. For all three mantle rheologies the magma pulse reaches the lower crust after 100 to 130 kyrs.

An extensional or compressional background strainrate of $10^{-15}\,\mathrm{s^{-1}}$ accelerates the process moderately making the pulse reach the crust after 95 to 105 kyrs.

Further increasing the geothermal gradient to $\partial_z T = 20\,\mathrm{K\,km^{-1}}$ leads to a timing of 65 to 75 kyrs for the pulse to reach the lower crust.

4.4.2 Mantle Rheology

As already described in the preceding section, the mantle rheology affects the velocity of the magma ascent, e.g., the branches of the pulse reach the lower crust after 350, 400 and 450 kyrs in case of *(a)* a wet dislocation and diffusion, *(b)* dry dislocation, *(c)* dry dislocation and diffusion creep rheology, respectively, for a geothermal gradient of $10\,\mathrm{K\,km^{-1}}$.

As described in the following section 4.4.3 we also observe that the lower viscosity that results from the wet rheology aids the pulse in developing separate branches. Hence, we see the small pulse branch in the case of wet mantle rheology (Figure 4.7) but not for dry mantle rheology (Figure 4.6). This counteracts the accelerated melt ascent as the branched pulse rises more slowly than a single pulse due to reduced buoyancy.

4.4.3 Size of Magmatic Pulse and Lower Crustal Rheology

In the simulations presented so far, the magmatic pulse always reached the surface and Figures 4.2 and 4.3 give a good idea of the evolution. It is known that in many cases magma actually does not reach the surface but instead crystallizes in batholiths in crustal depths [26, sec. 4-19]. As our model does not include crystallization or evolution of melt rheology, we cannot recover this process. Instead, we decreased the size of the pulse to see if the magma ascent stops before reaching the surface. For these simulations we kept the geothermal gradient at $\partial_z T = 15\,\mathrm{K\,km^{-1}}$, used wet or dry olivine dislocation and diffusion creep rheology for the mantle and quartzitic or mafic granulitic dislocation creep rheology in the lower crust.

Medium Magma Pulse In the simulations with halved pulse diameter (compared to the reference setup presented in section 4.3.2, corresponds to roughly 10 km) and zero background strainrate we can observe very well that most of the fluid remains in and below the crust, see Figures 4.4 and 4.5.

For a *dry mantle*, i.e., dry olivine dislocation and diffusion creep rheology, we observe that the pulse splits into two branches in 75 km depth. They reach the lower crust after 1.7 Myrs and start widening. In quartzitic lower crust they reunite to form a single massive structure of increased porosity. The ascent does not stop until the surface is reached after roughly 5 Myrs. If the lower crust is made of mafic granulite, the branches converge slightly, form a spread-out region of low porosity and the ascent stagnates. In both cases (quartzite or mafic granulite lower crust) we observe that most of the magma remains in a vertically extended structure that spans depths from 10 to 50 km.

In a *wet mantle* the pulse starts splitting in a shallower depth (60 km) and the branches move further apart than in the dry mantle. They form narrow vertical structures that reach the lower crust after 550 kyrs. In the quartzitic lower crust they widen and reunite after another 100 kyrs. After this, the process slows down and parts of the pulse start reaching the surface only after 8 Myrs. Most of the magma remains in the upper crust. For a mafic granulite lower crust the branches reunite in the lower crust and the ascent stagnates. Similarly to the dry mantle rheology case, most of the magma remains in the lower crust.

Small Magma Pulse For an initial magma pulse with 5 km diameter and zero background strainrate the pulse does not reach the surface. Instead it forms magmatic bodies of different shape in and below the crust, see Figures 4.6 and 4.7.

For a dry dislocation and diffusion creep mantle we observe that the pulse does not split into two branches but instead rises as a single pulse towards the lower crust and reaches it after 3.5 Myrs. For quartzitic lower crust rheology it forms a chamber in the uppermost mantle that feeds another magma body in the upper crust through a narrow dike-like structure, see Figure 4.6, bottom left. In the case of mafic granulite lower crust a less localized low porosity structure spreads out in the lower crust without reaching upper crustal depths. It is fed from a higher porosity magma body just below the crust.

For a wet mantle rheology the pulse splits into two narrow branches in a depth of about 75 km. As in the dry rheology case, the rise of the magma slows down after about 2 Myrs when a depth of roughly 40 km is reached. The branches rise more slowly than the single pulse in the dry mantle rheology reaching the lower crust after roughly 4 Myrs. However, they develop similar features as the single pulse in the dry rheology case, i.e., magma chambers below the (quartzitic) lower crust that feed magmatic bodies in the upper crust and spread out low porosity regions in the (mafic granulite) lower crust.

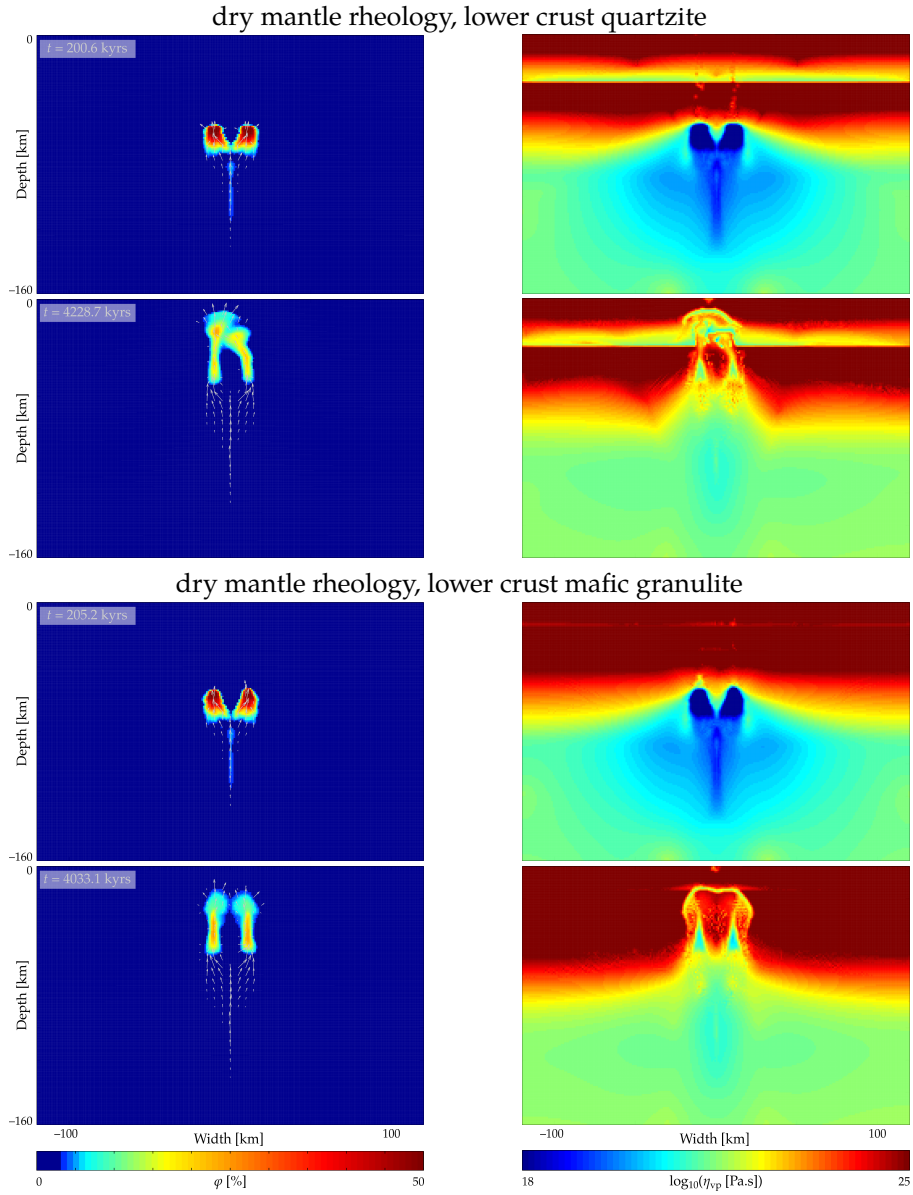

Figure 4.4: Porosity and fluid velocity arrows (left) and viscoplastic shear viscosity (right) during ascent of medium-sized magma pulse (initial diameter 10 km) in a dry mantle at zero background strainrate.

Pulse branches into two parts that reunite later. For quartzitic lower crust most of the magma remains in a vertically elongated structure spanning from 5 to 50 km depth. For mafic granulitic lower crust only a very minor part of the pulse reaches the upper crust, most of it remains in the lower crust and the uppermost mantle.

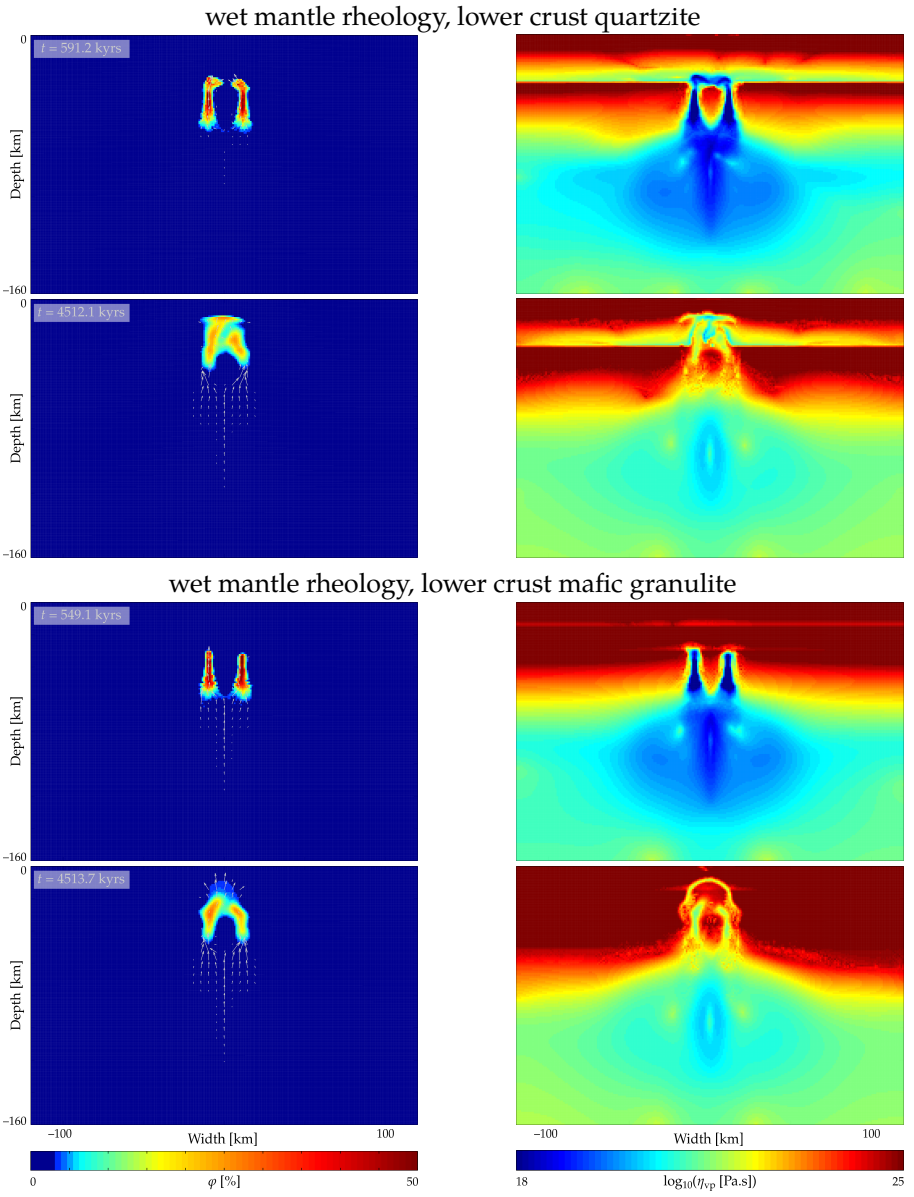

Figure 4.5: Porosity and fluid velocity arrows (left) and viscoplastic shear viscosity (right) during ascent of medium-sized magma pulse (initial diameter 10 km) in a wet mantle at zero background strainrate.

Pulse branches into two parts that reunite later. For quartzitic lower crust most of the pulse forms a magmatic body in the upper crust. For mafic granulitic lower crust only a very minor part of the pulse reaches the upper crust, most of it remains in and just below the lower crust.

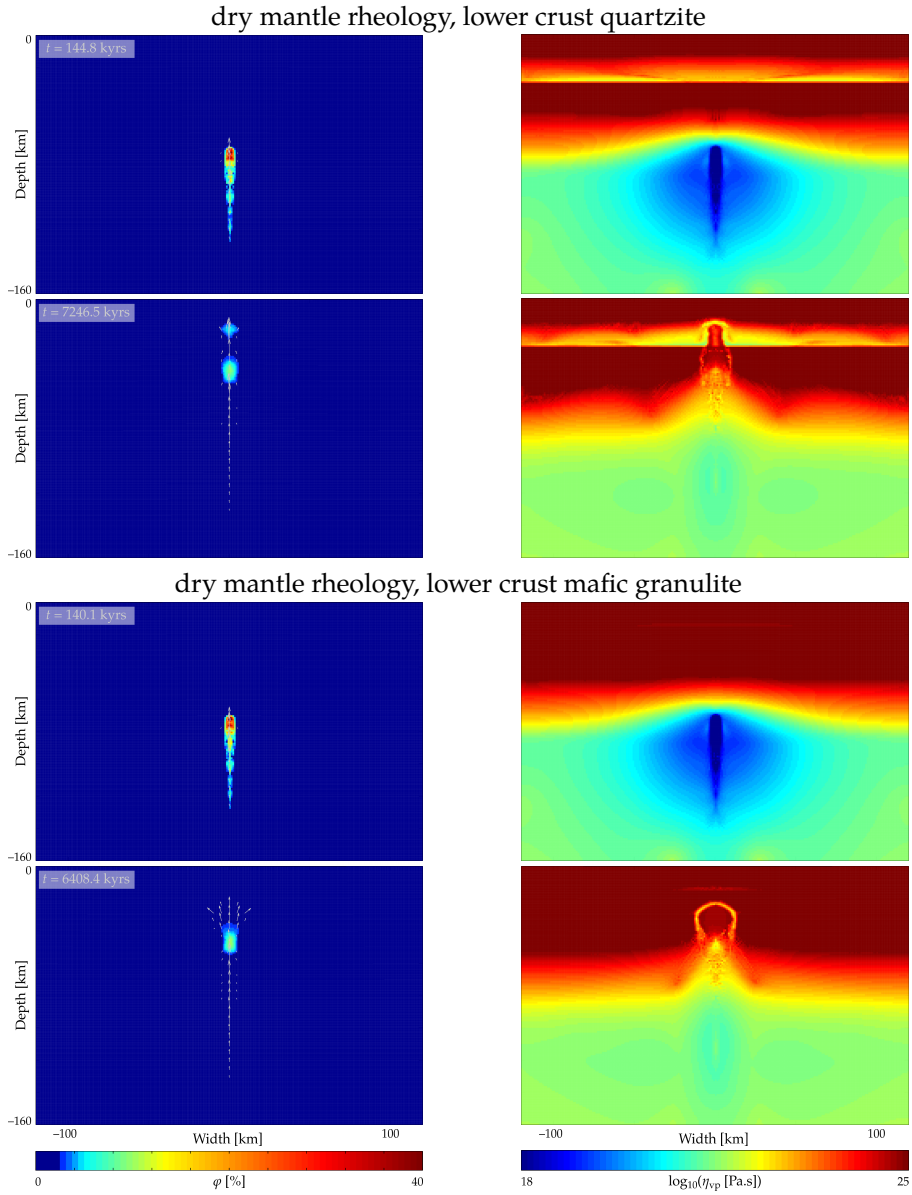

Figure 4.6: Porosity and fluid velocity arrows (left) and viscoplastic shear viscosity (right) during ascent of small-sized magma pulse (initial diameter 5 km) in a dry mantle at zero background strainrate.

Pulse does not branch. For quartzitic lower crust most of the magma remains in the mantle feeding a magmatic body in the upper crust through a lower crustal dike-like structure. For mafic granulitic lower crust part of the pulse spreads out in a wide low porosity structure in the lower crust being fed from a magmatic body below the crust.

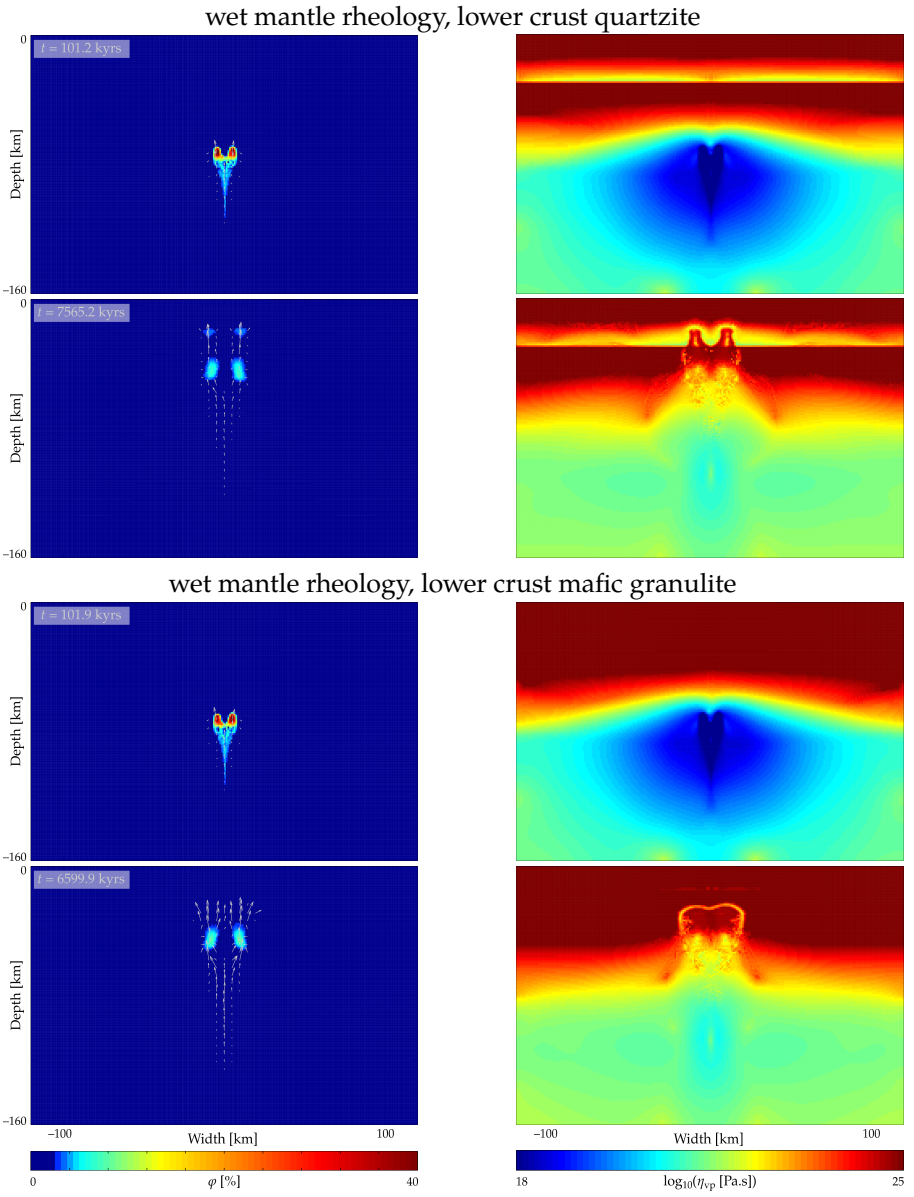

Figure 4.7: Porosity and fluid velocity arrows (left) and viscoplastic shear viscosity (right) during ascent of small-sized magma pulse (initial diameter 5 km) in a wet mantle at zero background strainrate.

Pulse branches into two parts after roughly 80 kyrs. The two smaller pulses propagate similar to the dry rheology case. For quartzitic lower crust they form dike-like structures in the lower crust feeding a body of magma that accumulates in the upper crust. For mafic granulite lower crust they form a higher porosity magmatic body in the uppermost mantle feeding a spread out lower porosity region in the lower crust.

Summary (Initial Size of Pulse) In Figure 4.8 we present the porosity field and the viscoplastic shear viscosity from a late stage of a choice of simulations. We chose a set of simulations where we successively changed parameters one by one. We started with a medium-sized pulse in a wet mantle with mafic granulite as lower crustal rheology. Then we changed *(i)* the size of the pulse, *(ii)* the lower crustal rheology, and *(iii)* the mantle rheology, such that the last row shows snapshots from a simulation that started with a small-sized pulse in a dry mantle with quartzitic lower crustal rheology.

Hence, in Figure 4.8 we can observe well the effects of the three parameters (initial size of pulse, rheology of mantle, rheology of lower crust) comparing two succeeding rows of figures.

Size of Pulse The smaller the pulse, the slower its ascent. While most of the medium-sized pulse ends up in the lower crust and forms a low-porosity region in parts of the upper crust, the small-sized almost completely remains below the lower crust.

Lower Crustal Rheology In both cases (quartzite, mafic granulite) most of the magma remains below the crust. Yet, in quartzitic lower crust dike-like features feed magma bodies at the base of the upper crust, while for mafic granulite part of the pulse propagates like porous flow in the lower crust without reaching upper crustal depths.

In the spread-out low porosity regions that occur for a mafic granulite lower crust the shear viscosity is relatively high with a narrow rim of lower viscosity (roughly 2 orders of magnitude) around the region. This implies that in this regime the strain rate dependence of the shear viscosity dominates over the porosity dependence.

Figure 4.8: Snapshots of the porosity field and the viscoplastic shear viscosity from late stages of four different simulations. Top: Medium-sized pulse, wet mantle rheology, lower crust mafic granulite. From top to bottom the following cumulative modifications are applied: *(i)* small-sized pulse, *(ii)* quartzitic lower crust, *(iii)* dry mantle rheology.

(i) Comparing first and second row: The smaller the pulse, the slower its ascent. While most of the medium-sized pulse ends up in the lower crust and forms a low-porosity region in parts of the upper crust, the small-sized almost completely remains below the lower crust.

(ii) Comparing second and third row: For quartzite and mafic granulite lower crustal rheology most of the magma remains below the crust. Yet, in quartzitic lower crust dike-like features feed magma bodies at the base of the upper crust, while for mafic granulite part of the pulse propagates like porous flow in the lower crust without reaching upper crustal depths. In the spread-out low porosity regions that occur for a mafic granulite lower crust the shear viscosity is relatively high with a narrow rim of lower viscosity (roughly 2 orders of magnitude) around the region. This implies that in this regime the strain rate dependence of the shear viscosity dominates over the porosity dependence.

(iii) Comparing third and fourth row: The wet mantle supports splitting of the pulse into branches and the split branches have lower buoyancy slowing down the ascent compared to dry mantle rheology. Apart from this, the simulations develop very similar features.

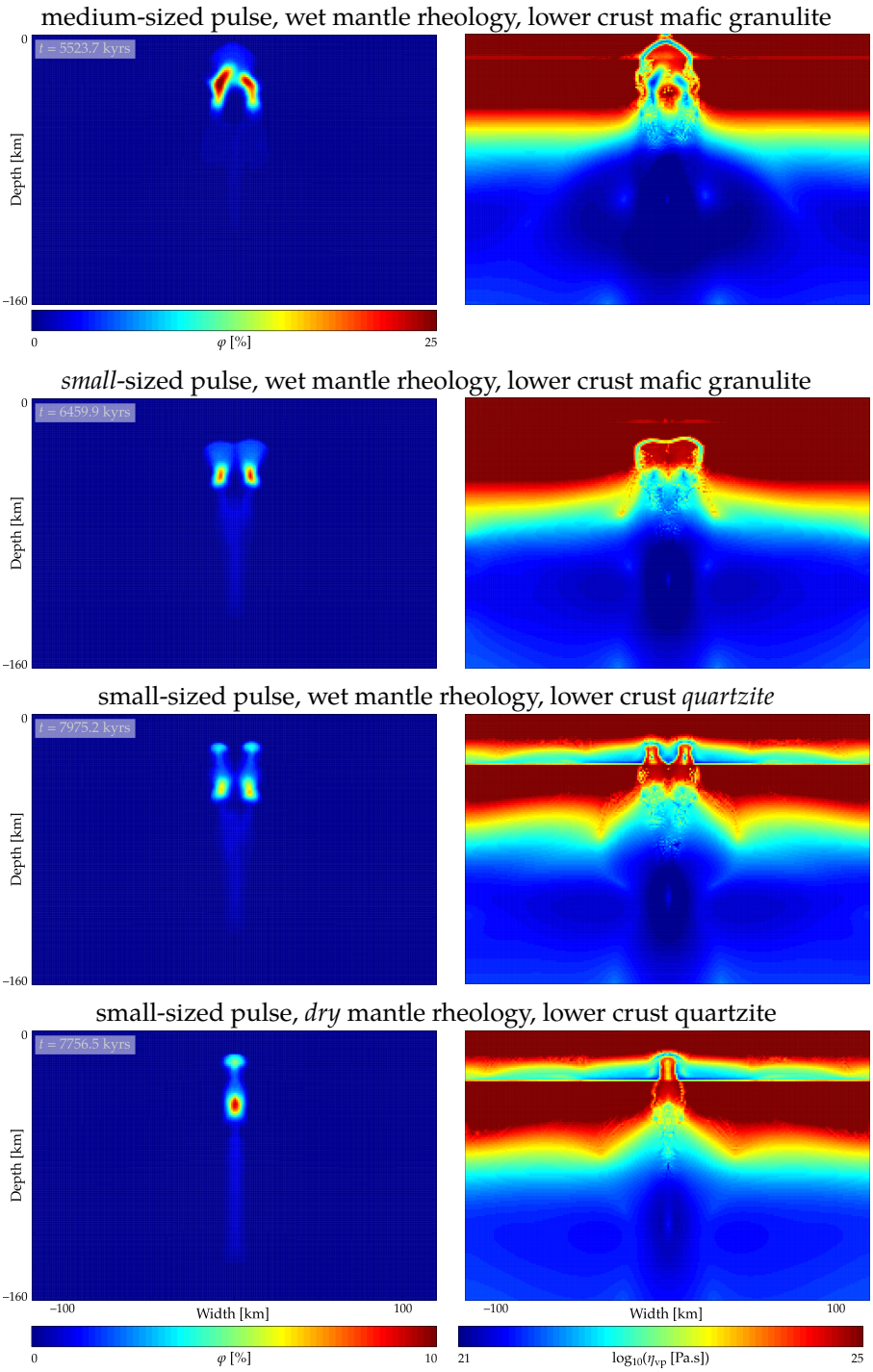
medium-sized pulse, wet mantle rheology, lower crust mafic granulite
t = 5523.7 kyrs
small-sized pulse, wet mantle rheology, lower crust mafic granulite
t = 6459.9 kyrs
small-sized pulse, wet mantle rheology, lower crust quartzite
t = 7975.2 kyrs
small-sized pulse, dry mantle rheology, lower crust quartzite
t = 7756.5 kyrs
Depth [km]
0
−160
Width [km]
−100
100
φ [%]
0
25
10
log10(ηvp [Pa.s])
21

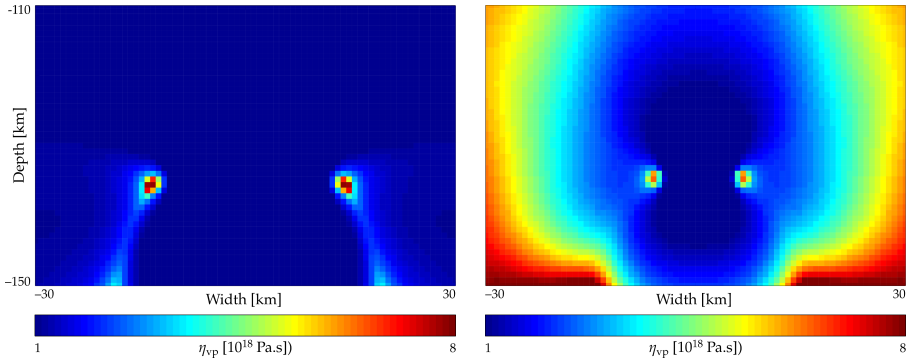

Figure 4.9: Zoomed view of viscoplastic shear viscosity for medium (left) and small-sized (right) pulse after first time step. Increased viscosity at the sides of the pulse effectively limits the maximum velocity in the middle of the pulse. Doubling the distance leads to roughly quadrupled maximum vertical velocity.

Mantle Rheology The wet mantle supports splitting of the pulse into branches and the split branches have lower buoyancy slowing down the ascent compared to dry mantle rheology. Apart from this, the simulations develop very similar features.

4.4.4 Background Tectonic Deformation

We ran simulations without deformation (zero background strainrate), in a compressional and in an extensional regime (background strainrate $\dot{\epsilon}_{BG} = 10^{-15}\,s^{-1}$). We observe that the magma ascends most efficiently in the extensional regime, least efficiently without deformation.

Dry Mantle Rheology First, we consider *quartzitic crustal phases* and a dry olivine dislocation and diffusion creep mantle rheology. For a geothermal gradient of $\partial_z T = 15\,K\,km^{-1}$ the pulse branches at a depth of about 70 km after roughly 42 kyrs, independent of the three background strainrate regimes. Yet, for the extensional setup we already observe strain localization in the upper crust at this early stage, see Figure 4.10, right.

As expected, the deformational regimes lead to much higher stress levels in the crust and uppermost mantle. When the branched pulse is at a depth of 50 km we observe a maximum stress of 70 MPa without external deformation, but 250 to 300 MPa in the compressional and extensional regime, respectively, see Figure 4.10, left. Larger stresses seem to support a more rapid melt ascent. The pulse reaches the lower crust after approximately 105, 115 and 140 kyrs for extensional, compressional and free-slip lateral boundary conditions, respectively.

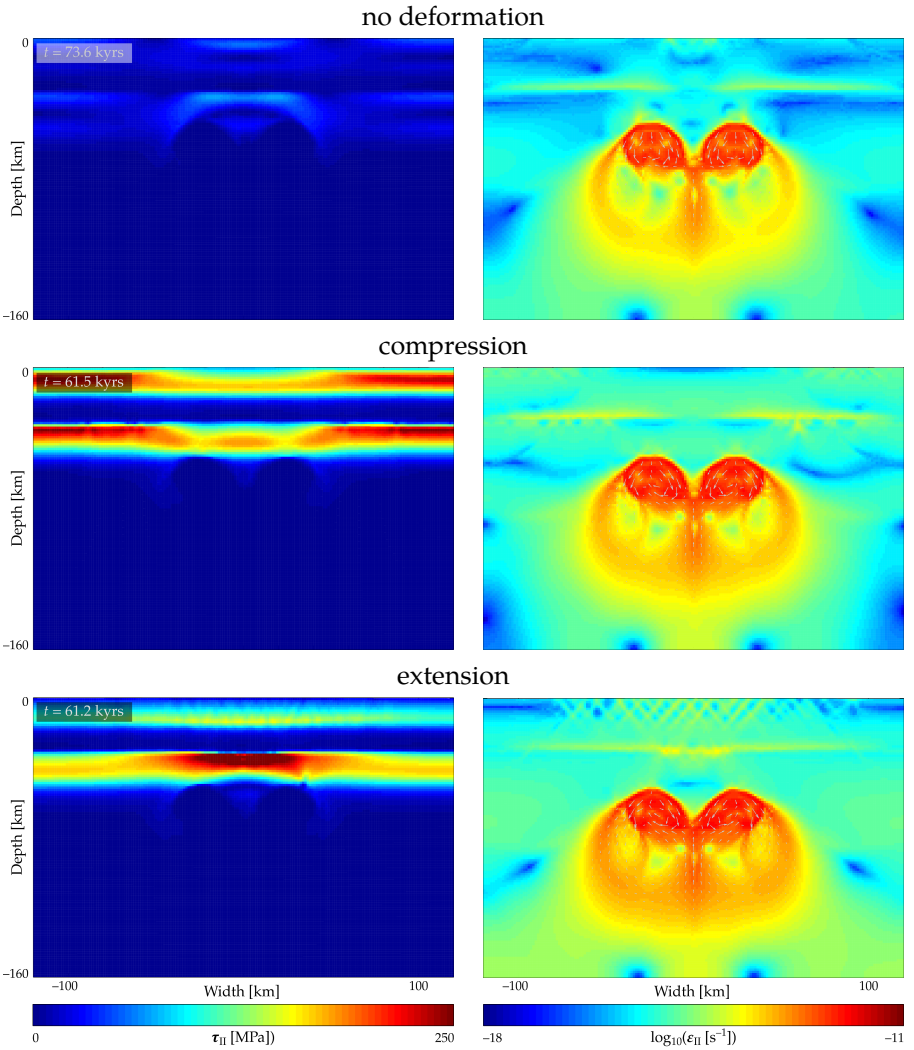

Figure 4.10: Snapshots of stress and (square root of) strain rate invariant when melt reaches 50 km depth for different deformational regimes: no external deformation, compressional, extensional lateral boundary conditions (top to bottom).

In the deformational setups the stresses are a lot larger. For the extensional setup strain localizes in the upper crust early during the simulation. Strain localization is observed for the compressional setup soon after the presented snapshot. Without external deformation there is barely any strain localization throughout the simulation.

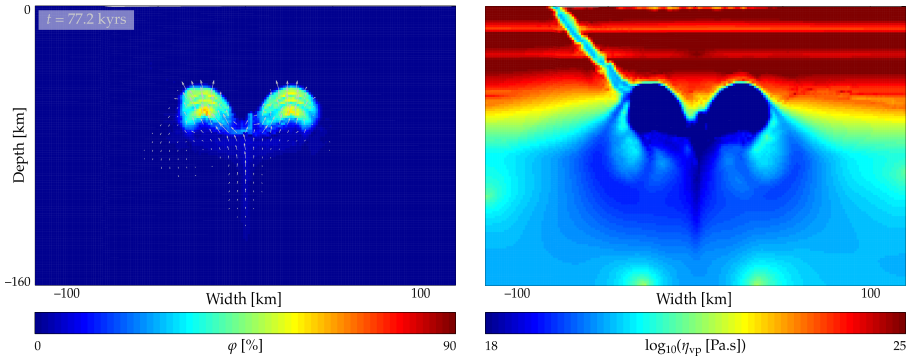

Figure 4.11: Porosity field (with fluid velocity arrows) and viscoplastic shear viscosity snapshot from a simulation with extensional background strainrate, mafic granulite lower crust and dry olivine mantle rheology. A zone of shear localization reaches from the surface to the tip of the melt branch traversing both crustal layers.

Part of the pulse reaches the surface after 240, 380 and 420 kyrs for the extensional, compressional and free-slip regime, respectively. In all three cases a larger magma body remains just below the lower crust but most of the magma pulse traverses both crustal layers.

For a *mafic granulite lower crust* deformational boundary conditions lead to early local weakening of the crust. We observe this after 70 to 80 kyrs in the extensional and compressional case, respectively, where a narrow weakenend structure ranges from the surface to the tip of one of the pulse branches in 50 km depth, see Figure 4.11. This structure is the continuation of a shear zone that starts at the surface a few time steps earlier. A similar structure develops in the non-deformational simulation only after more than 370 kyrs when the tip of the pulse is at 20 km depth.

Although the melt does not follow these structures exactly, their development seems to support a more rapid ascent. In the deformational setups the pulse reaches the surface after about 200 kyrs (extensional) ot 250 kyrs (compressional), without deformation only after about 500 kyrs.

Wet Mantle Rheology The pulse traverses the wet olivine dislocation and diffusion creep rheology mantle in 90 to 100 kyrs and reaches the *quartzitic* lower crust. Again, the extensional regime leads to a (slightly) faster ascent in the mantle. The time to reach the surface is about 240 kyrs in the extensional setup, 280 kyrs for compressional boundary conditions. Without deformation it takes about 360 kyrs. After reaching the lower crust the branches of the pulse slightly diverge in the compressional case and slightly converge in the extensional case.

Similar to the case of a dry mantle we observe shear zones that stretch through the *mafic granulite* lower crust to the tip of the melt pulse in deformational setups. On the one hand, the melt pulse takes longer (420 kyrs) to reach the surface for zero background strainrate than in the case of quartzitic lower crust. On the other hand, the melt ascent is accelerated by the weakened zones letting it reach the surface after 190 and 210 kyrs in the extensional and compressional case, respectively.

4.4.5 Fluid Viscosity

Changing the fluid viscosity in the reference setup leads to a surprisingly similar melt ascent at first, i.e., the melt pulse rises to a depth of 70 km and starts diverging into two branches within roughly 60 kyrs. After this, differences to the reference setup dominate. The process strongly slows down, i.e., the vertical velocity gradually drops by two orders of magnitude from tens of centimeters per year to millimeters per year and below. Two symmetric massive bodies of increased porosity form in more than 50 km depth, each more than 50 km wide but less than 15 km deep. The ascent stagnates quite soon and we can observe how the porosity slowly extends horizontally, see Figure 4.12.

4.5 Discussion

In this study we examined the effect of several physical parameters on the process of magma ascending from the upper mantle towards the surface: the geothermal gradient, the mantle and lower crust rheology, the size of the magmatic pulse, the background strainrate, and the fluid viscosity.

A predominant feature in most of the simulations is the splitting of the flattened pulse into two separate branches that (temporarily) rise independent of each other. This provides an explanation for the shape of temperature anomalies in numerical models of the East African Rift [27, 28]. Bastow et al. [29] interpret a seismically imaged low-velocity region of similar shape below Ethiopia as upper mantle continuation of an African superplume.

As we can see well from Figure 4.3 the process of ascending magma is an efficient way of bringing mantle material up into the upper crust. This study does not take into account surface processes which support exposure of these rocks.

The formation of plutons in crustal depths can be observed particularly for medium to small initial melt pulses. While significant parts of large pulses reach the surface, still we observe horizontal structures in about 30 km depth, see Figure 4.2.

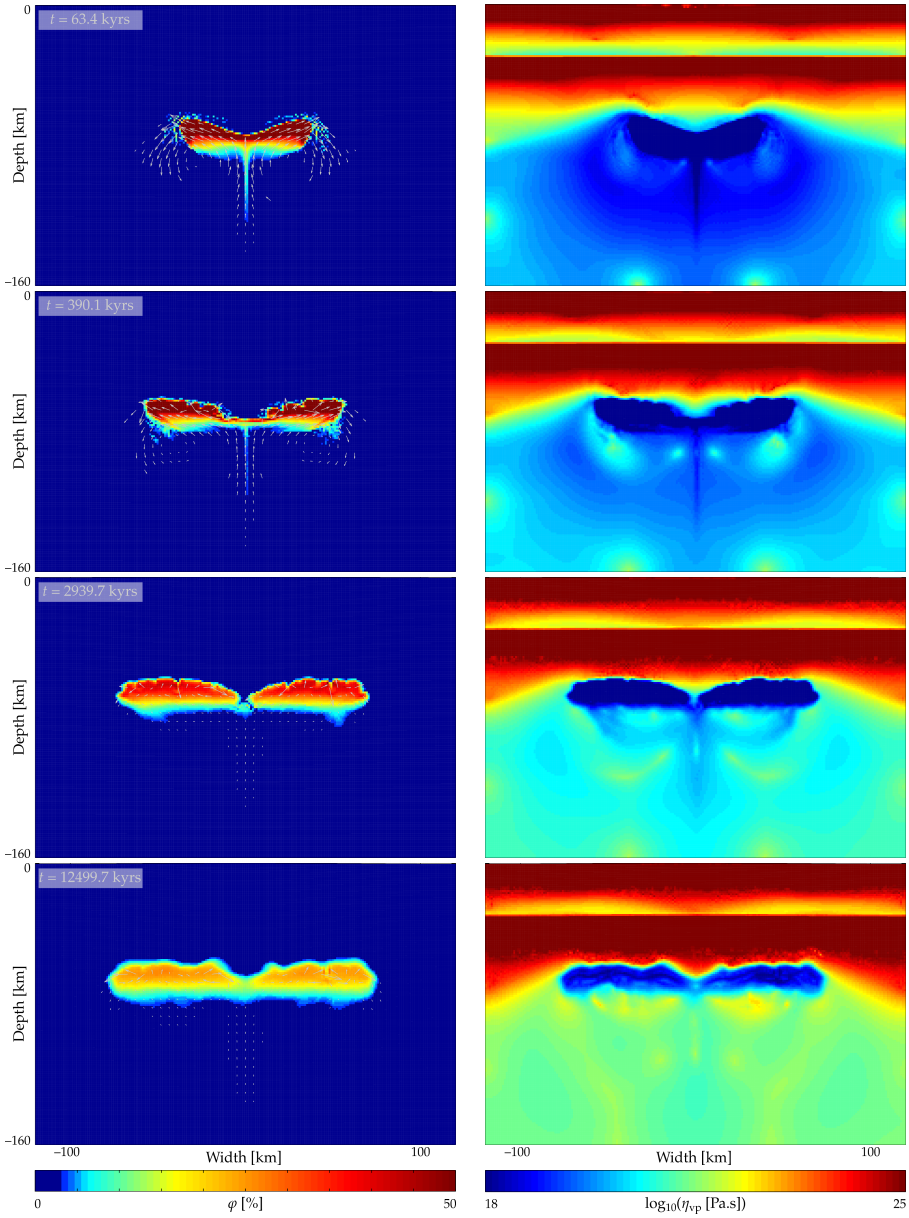

Figure 4.12: Porosity and fluid velocity arrows (left) and viscoplastic shear viscosity (right) during ascent of magma pulse with increased fluid viscosity $\eta_f = 10^{10}$ Pa s compared to reference setup in a dry mantle at zero background strainrate.

First, the melt ascent seems similar to the reference setup but after the pulse starts branching it strongly extends horizontally almost without any vertical ascent. Furthermore, the process slows down massively and even after several millions of years we see very little evolution.

One needs to keep in mind that the model does not consider crystallization. The pulse reaches the crust at a temperature of roughly 500 °C. Only later, when fluid velocity has dropped, the temperature advection "catches up", cp. Figure 4.3 (171.9 and 337.6 kyrs). This would lead to crystallization of most of the material which cannot be captured by the underlying model. On the other hand, heat sources such as radiogenic or shear heating effects, are neglected. Including these would lead to higher temperatures.

For small pulses we observe that most of the melt settles just below the crust causing smaller partially molten regions in the crust, see Figures 4.6–4.8. This can be interpreted as feeding instances of large magma chambers that are assumed to be below volcanic systems like, e.g., Vesuvius [30, 31] or Mt. St. Helens [32].

For small to medium-sized pulses we can observe well that the mafic granulite lower crust poses a strong obstacle for the ascent of the pulse, see Figures 4.4–4.8. In all of these cases, the melt ascent is interrupted in greater depths than for the corresponding setup with quartzitic lower crust. However, in section 4.4.4 we observed that in regimes of tectonic deformation the melt ascent is more rapid for the lower crust being made of mafic granulite than in the quartzitic case.

Larger fluid viscosity corresponding to a more felsic composition of the molten material leads to a slower ascent and the formation of massive subcrustal magmatic bodies. However, we realize that the assumption of a felsic melt in 130 km depth is a very rough approximation. In this respect, it would be beneficial to consider variable melt viscosity that evolves from a mafic to a more felsic composition while rising through the lithosphere. Unfortunately, this could not be covered in the present study.

For an improved model the energy equation would need to be coupled to the mechanical system more closely by including separate terms for fluid and solid specific heat capacity and a more complex material derivative applied to the temperature T, see [17, 33]. Furthermore, melting and crystallization would need to be taken into account as described in, e.g., [14, 15]. As compositional mineral phases of the molten material crystallize at different temperature/pressure regimes the composition of the melt changes while it ascends through the lithosphere. As mentioned above, these compositional changes are not considered in our model, see [34] for recent research on this.

4.6 Summary and Conclusions

Varying physical parameters in the lithospheric scale setup we have seen numerous effects that we summarize in what follows.

Geothermal gradient A steeper geothermal gradient effectively decreases the viscosity and, hence, leads to higher velocities and faster melt ascent. Furthermore, for higher temperatures the pulse rises to shallower depths before it splits into branches. For the simulations in section 4.4.1 the splitting happens roughly along the 1100 °C isotherm, cp. Figure 4.3. For smaller melt pulses there does not seem to be an equivalent correlation.

Mantle Rheology We used dry olivine dislocation, dry olivine dislocation and diffusion, as well as wet olivine dislocation and diffusion creep rheologies for the mantle phase. Adding diffusion creep to the dry olivine rheology accelerates the melt ascent. Choosing wet olivine rheologies increases this effect but also facilitates branching of the melt pulse which in turn leads to slower ascent. The three types of mantle rheology do not yield qualitatively different features but rather affect the timing of the overall process.

Size of Pulse Pulses smaller than the one in the reference setup not necessarily reach the surface. The ascent of medium-sized pulses stops if the lower crust has mafic granulite rheology. Smaller pulses have not been observed to reach the surface in our simulations. Generally, smaller pulses rise more slowly than larger ones and are less likely to split into two branches.

Background Strainrate When external deformation is applied via lateral boundary conditions the stresses in the domain are higher. This leads to a more efficient melt ascent in the mantle and crust. The efficiency is maximal for the extensional regime, minimal for the non-deformational regime.

Rheology of Lower Crust For smaller melt pulses we observe that the lower crust with mafic granulite rheology was harder to pass than with quartzite rheology. However, these simulations where run without external deformation. In the context of different background strainrates we observed that a mafic granulite lower crust is more sensitive to deformational boundary conditions than quartzite. Hence, in deformational regimes the melt propagation is more efficient if the lower crust has mafic granulite rheology, without deformation it is more efficient for quartzitic lower crust rheology.

Fluid Viscosity In one experiment we prescribed a fluid viscosity of $\eta_f = 10^{10}$ Pa s corresponding to molten material of felsic composition, compared to $\eta_f = 10^2$ Pa s in the reference setup corresponding to basaltic composition. Initially, we observed similar ascent and branching of the pulse. However, for

increased fluid viscosity the ascent stops in about 50 km depth and the fluid extends horizontally forming massive bodies well below the crust.

We found that melt propagates most efficiently for *(i)* steeper geothermal gradients, *(ii)* wet mantle rheology, and *(iii)* in a deformational tectonic setting. We also described the effect of different initial pulse sizes, lower crustal rheologies, increased fluid viscosity as well as some of the interactions of these parameters. However, we recognize that this study barely scratches the surface of lithospheric scale melt migration modelling. We consider it to be a "signpost" for future numerical modelling of melt migration processes.

The model underlying this study is described in more detail in chapter 3. We found it to be robust for broad parameter ranges relevant in lithospheric scale melt migration setups. This enables us to investigate numerous questions in the future that could not be addressed with numerical modelling before.

References

[1] D. P. McKenzie. The Generation and Compaction of Partially Molten Rock. *Journal of Petrology*, 25(3):713–765, 1984. DOI:10.1093/petrology/25.3.713.

[2] D. R. Scott and D. J. Stevenson. Magma ascent by porous flow. *Journal of Geophysical Research: Solid Earth*, 91(B9):9283–9296, 1986. DOI:10.1029/JB091iB09p09283.

[3] C. Wiggins and M. Spiegelman. Magma migration and magmatic solitary waves in 3-D. *Geophysical Research Letters*, 22(10):1289–1292, 1995. DOI:10.1029/95GL00269.

[4] V. Barcilon and F. M. Richter. Nonlinear waves in compacting media. *Journal of Fluid Mechanics*, 164:429–448, 1986.

[5] V. Barcilon and O. M. Lovera. Solitary waves in magma dynamics. *Journal of Fluid Mechanics*, 204:121–133, 1989. ISSN 1469-7645. DOI:10.1017/S0022112089001680.

[6] M. Spiegelman. Flow in deformable porous media. Part 2—Numerical analysis – the relationship between shock waves and solitary waves. *Journal of Fluid Mechanics*, 247:39–63, 1993. ISSN 1469-7645. DOI:10.1017/S0022112093000370.

[7] T. Keller, D. A. May, and B. J. P. Kaus. Numerical modelling of magma dynamics coupled to tectonic deformation of lithosphere and crust. *Geophysical Journal International*, 195(3): 1406–1442, 2013. DOI:10.1093/gji/ggt306.

[8] J. Dannberg and T. Heister. 3D Compressible Melt Transport with Mesh Adaptivity. Submitted, 2015.

[9] J. A. D. Connolly and Y. Y. Podladchikov. Compaction-driven fluid flow in viscoelastic rock. *Geodinamica Acta*, 11(2–3):55–84, 1998. DOI:10.1080/09853111.1998.11105311.

[10] J. A. D. Connolly and Y. Y. Podladchikov. Decompaction weakening and channeling instability in ductile porous media: Implications for asthenospheric melt segregation. *Journal of Geophysical Research: Solid Earth*, 112(B10), 2007. DOI:10.1029/2005JB004213.

[11] C. N. Richardson. Melt flow in a variable viscosity matrix. *Geophysical Research Letters*, 25(7): 1099–1102, 1998. ISSN 1944-8007. DOI:10.1029/98GL50565.

[12] R. F. Katz, M. Spiegelman, and B. Holtzman. The dynamics of melt and shear localization in partially molten aggregates. *Nature*, 442(7103):676–679, 2006. DOI:10.1038/nature05039.

[13] A. Y. Rozhko, Y. Y. Podladchikov, and F. Renard. Failure patterns caused by localized rise in pore-fluid overpressure and effective strength of rocks. *Geophysical Research Letters*, 34(22): L22304, 2007. DOI:10.1029/2007GL031696.

[14] H. Schmeling. A model of episodic melt extraction for plumes. *Journal of Geophysical Research: Solid Earth*, 111(B3):B03202, 2006. ISSN 2156-2202. DOI:10.1029/2004JB003423.

[15] H. Schmeling. Dynamic models of continental rifting with melt generation. *Tectonophysics*, 480(1–4):33–47, 2010. ISSN 0040-1951. DOI:10.1016/j.tecto.2009.09.005.

[16] S. Rhebergen, G. N. Wells, A. J. Wathen, and R. F. Katz. Three-Field Block Preconditioners for Models of Coupled Magma/Mantle Dynamics. *SIAM Journal on Scientific Computing*, 37 (5):A2270–A2294, 2015. DOI:10.1137/14099718X.

[17] D. Bercovici, Y. Ricard, and G. Schubert. A two-phase model for compaction and damage: 1. General Theory. *Journal of Geophysical Research: Solid Earth*, 106(B5):8887–8906, 2001. ISSN 2156-2202. DOI:10.1029/2000JB900430.

[18] G. Hirth and D. Kohlstedt. *Rheology of the Upper Mantle and the Mantle Wedge: A View from the Experimentalists*, pages 83–105. American Geophysical Union, 2003. ISBN 978-1-118-66857-3. DOI:10.1029/138GM06.

[19] A. Castro and T. V. Gerya. Magmatic implications of mantle wedge plumes: Experimental study. *Lithos*, 103(1–2):138–148, 2008. ISSN 0024-4937. DOI:10.1016/j.lithos.2007.09.012.

[20] T. V. Gerya and F. I. Meilick. Geodynamic regimes of subduction under an active margin: effects of rheological weakening by fluids and melts. *Journal of Metamorphic Geology*, 29(1): 7–31, 2011. ISSN 1525-1314. DOI:10.1111/j.1525-1314.2010.00904.x.

[21] G. Zhu, T. V. Gerya, P. J. Tackley, and E. Kissling. Four-dimensional numerical modeling of crustal growth at active continental margins. *Journal of Geophysical Research: Solid Earth*, 118 (9):4682–4698, 2013. ISSN 2169-9356. DOI:10.1002/jgrb.50357.

[22] G. Ranalli. *Rheology of the Earth*. Springer, Netherlands, 2nd edition, 1995. ISBN 978-0-412-54670-9.

[23] W. Frisch, M. Meschede, and R. C. Blakey. *Plate Tectonics: Continental Drift and Mountain Building*. Springer Science & Business Media, Heidelberg, 2010. ISBN 978-3-540-76503-5. DOI:10.1007/978-3-540-76504-2.

[24] J. Grotzinger, T. H. Jordan, F. Press, and R. Siever. *Allgemeine Geologie (orig. Understanding Earth)*. Springer, Berlin, Heidelberg, 5th edition, 2011. ISBN 978-3-827-41828-8.

[25] A. Tanaka, M. Yamano, Y. Yano, and M. Sasada. Geothermal gradient and heat flow data in and around Japan (I): Appraisal of heat flow from geothermal gradient data. *Earth, Planets and Space*, 56(12):1191–1194, 2014. ISSN 1880-5981. DOI:10.1186/BF03353339.

[26] D. L. Turcotte and G. Schubert. *Geodynamics*. Cambridge University Press, 2nd edition, 2002. ISBN 978-0-521-66624-4.

[27] G. Corti, J. van Wijk, M. Bonini, D. Sokoutis, S. Cloetingh, F. Innocenti, and P. Manetti. Transition from continental break-up to punctiform seafloor spreading: How fast, symmetric and magmatic. *Geophysical Research Letters*, 30(12):1604, 2003. ISSN 1944-8007. DOI:10.1029/2003GL017374.

[28] Herbert Wallner and Harro Schmeling. Rift induced delamination of mantle lithosphere and crustal uplift: a new mechanism for explaining Rwenzori Mountains' extreme elevation? *International Journal of Earth Sciences*, 99(7):1511–1524, 2010. DOI:10.1007/s00531-010-0521-6.

[29] I. D. Bastow, A. A. Nyblade, G. W. Stuart, T. O. Rooney, and M. H. Benoit. Upper mantle seismic structure beneath the Ethiopian hot spot: Rifting at the edge of the African low-velocity anomaly. *Geochemistry, Geophysics, Geosystems*, 9(12):Q12022, 2008. ISSN 1525-2027. DOI:10.1029/2008GC002107.

[30] E. Auger, P. Gasparini, J. Virieux, and A. Zollo. Seismic Evidence of an Extended Magmatic Sill Under Mt. Vesuvius. *Science*, 294(5546):1510–1512, 2001. ISSN 0036-8075. DOI:10.1126/science.1064893.

[31] B. Scaillet, M. Pichavant, and R. Cioni. Upward migration of Vesuvius magma chamber over the past 20,000 years. *Nature*, 455(7210):216–219, 2008.

[32] Eric Hand. Fire down below. *Science*, 350(6262):725–726, 2015. DOI:10.1126/science.350.6262.725.

[33] D. Bercovici and Y. Ricard. Energetics of a two-phase model of lithospheric damage, shear localization and plate-boundary formation. *Geophysical Journal International*, 152(3):581–596, 2003. DOI:10.1046/j.1365-246X.2003.01854.x.

[34] T. Keller and R. F. Katz. Effects of volatiles on melt production and reactive effects of volatiles on melt production and reactive flow in the mantle. *arXiv Geophysics (physics.geo-ph)*, 1510.01334, 2015. URL http://arxiv.org/abs/1510.01334.

CHAPTER 5

Selected Applications in Melt Migration Modelling

5.1 Introduction

In this chapter we showcase two applications based on the parameter study presented in chapter 4. The major assumption of the study was the existence of a single melt pulse in the Earth's upper mantle that rises independent of other magmatic effects through a horizontally homogeneous lithosphere. By introducing multiple pulses with temporal offset we can investigate *(i)* how episodic magmatic events interact, *(ii)* how the melt ascent differs if the lithospheric host rock has been weakened by previous magmatic activity, *(iii)* how previously formed crustal magmatic bodies are affected by later magmatic pulses.

Secondly, we vary the setup by introducing a region of (randomized) low, yet increased, porosity instead of a single high porosity pulse. From this, we expect multiple small pulses to rise towards the surface simultaneously. To resolve these we use an unstructured mesh that is adaptively refined to reach higher resolutions where significant porosity is present without spending too much computational effort on resolving areas that are less important for the overall dynamics.

As magmatic structures are known to occur on very different spatial scales—from meter-scale dikes to kilometer-scale batholiths—it is desirable to account for this in the discretization. An adaptive mesh is the most attractive way to achieve this. Dannberg and Heister [1] have performed a study on dynamics of the *asthenospheric* mantle and melt migration using adaptive meshes not considering visco-elasto-plastic rheologies. Hence, the present work is the first on

modelling coupled lithosphere and two-phase melt migration dynamics with visco-elasto-plastic rheologies using mesh adaptivity.

5.2 Governing Equations

We consider a system of coupled lithosphere and two-phase porous flow dynamics in a bounded, connected domain $\Omega \in \mathbf{R}^2$ with Lipschitz continuous boundary $\partial\Omega$. We briefly repeat the governing equations described in more detail in the respective sections 3.2.4 and 4.2 in the previous chapters, see also [2, 3],

$$-\nabla \cdot \left(\eta_{\text{eff}} \left(\nabla \boldsymbol{v}_{\text{s}} + (\nabla \boldsymbol{v}_{\text{s}})^{\mathsf{T}} \right) - \frac{2}{3} \eta_{\text{eff}} \nabla \cdot \boldsymbol{v}_{\text{s}} \boldsymbol{I}_2 \right) + \nabla p_{\text{f}} + \nabla p_{\text{c}} = \\ = -\bar{\varrho} \boldsymbol{g} + \nabla \cdot \chi_\tau \tilde{\boldsymbol{\tau}}_{\text{s}}^o, \tag{5.1a}$$

$$-\nabla \cdot \boldsymbol{v}_{\text{s}} + \nabla \cdot K_D \nabla p_{\text{f}} = -\nabla \cdot K_D \varrho_{\text{f}} \boldsymbol{g} \tag{5.1b}$$

$$-\nabla \cdot \boldsymbol{v}_{\text{s}} - \frac{p_{\text{c}}}{\zeta_{\text{eff}}} = -\frac{\chi_p \Delta p^o}{\zeta_{\text{eff}}}, \tag{5.1c}$$

$$\frac{\mathrm{D}_{\text{s}} \varphi}{\mathrm{D}t} - (1 - \varphi) \nabla \cdot \boldsymbol{v}_{\text{s}} = 0, \tag{5.2}$$

The effective viscosities η_{eff} and ζ_{eff} are given by (3.23) and (3.25), respectively. Furthermore, $\boldsymbol{v}_{\text{s}}$ denotes the solid velocity, $\boldsymbol{I}_2$ the 2-dimensional identity tensor, p_{f} fluid pressure, p_{c} compaction pressure, $\bar{\varrho}$ the porosity-weighted average density, $\boldsymbol{g}$ gravitational acceleration, χ_τ a visco-elastic shear stress evolution parameter, $\tilde{\boldsymbol{\tau}}_{\text{s}}^o$ the rotated solid deviatoric stress tensor from the previous time step, $K_D = \kappa_\varphi / \eta_{\text{f}}$ a Darcy coefficient (permeability to fluid viscosity ratio), ϱ_{f} fluid density, χ_τ a compaction stress evolution parameter, Δp^o the pressure difference from the previous time step, φ the porosity (volume melt fraction), and t time. The operator $\mathrm{D}_{\text{s}}/\mathrm{D}t = \partial/\partial t + \boldsymbol{v}_{\text{s}} \cdot \nabla$ denotes the solid material derivative.

Here, effective viscosities η_{eff} and ζ_{eff}, average density $\bar{\varrho}$, and permeability κ_φ are functions of the porosity φ introducing nonlinearities to the system. Additionally, as geomaterials are non-Newtonian, the effective shear viscosity η_{eff} depends on the strain rate $\dot{\boldsymbol{\varepsilon}}$.

The system is complemented by an initial condition for the porosity $\varphi(t_0) = \varphi_0$ and the following boundary conditions. Let the boundary $\partial\Omega = \Gamma_D \cup \Gamma_N$, $(\Gamma_D \cap \Gamma_N = \emptyset)$, and let $\boldsymbol{b}_D : \Gamma_D \to \mathbf{R}^2$, $\boldsymbol{b}_N : \Gamma_N \to \mathbf{R}^2$ be given boundary data. Denoting the outward unit normal vector on $\partial\Omega$ as $\boldsymbol{n}$ we assume the following boundary conditions.

$$\boldsymbol{v}_\mathrm{s} = \boldsymbol{b}_D \qquad \text{on } \Gamma_D, \tag{5.3a}$$
$$\boldsymbol{\tau}_\mathrm{s}\boldsymbol{n} - (p_\mathrm{f} + p_\mathrm{c})\,\boldsymbol{n} = \boldsymbol{b}_N \qquad \text{on } \Gamma_N, \tag{5.3b}$$
$$-K_D(\nabla p_\mathrm{f} + \varrho_\mathrm{f}\boldsymbol{g}) \cdot \boldsymbol{n} = 0 \qquad \text{on } \partial\Omega, \tag{5.3c}$$

We solve the quasi-static three-field equations (5.1) for the major unknowns solid velocity $\boldsymbol{v}_\mathrm{s}$, fluid pressure p_f, and compaction pressure p_c with the finite element method described in section 3.3. Then, the porosity is updated inserting the current solid velocity solution guess into (5.2). These two steps are iteratively repeated until a convergence criterion is met.

When the nonlinearities are resolved sufficiently, an energy conservation equation is solved with a standard second order continuous finite element method, see 4.2.2,

$$\bar{\varrho} c_p \frac{\mathrm{D}_\mathrm{s} T}{\mathrm{D}t} - \nabla \cdot (k \nabla T) = 0, \tag{5.4}$$

where c_p denotes specific heat capacity, T temperature, and k conductivity. For simplicity, we assume no heat sources or sinks.

All material properties are determined in the same way as in the previous chapter, see 4.2.3 and Table 5.1.

5.3 Episodic Melt Pulses

5.3.1 Experimental Setup

In section 4.4.3 we considered melt pulses of different size starting off at the base of the lithosphere and rising towards the surface. We found that smaller pulses ascend more slowly and that, depending on the rheology of the manle and the crust as well as on the tectonic deformational regime, the fluid reaches the surface or remains in crustal and sub-crustal depths.

Based on the simulations using wet dislocation and diffusion creep mantle and a mafic granulite lower crustal rheology, see Table 4.2, we perform further experiments with multiple episodic melt pulses as considered in, e.g., [4–7]. As in chapter 4, the upper crust follows a quartzite dislocation creep law that we already used in all simulations presented in chapter 4. We assume no external deformation of the domain, i.e., free-slip lateral boundaries.

To introduce a second (or third) pulse at a given time instant we set the porosity φ on the markers that are in the location where the initial pulse started off to the values of another Gaussian pulse of same size and extent.

Table 5.1: Parameters for the experiments on multiple episodic melt pulses.

Symbol	Name	Value
ϱ_{UC}	reference density (upper crust)	$2.70 \times 10^3\,\mathrm{kg\,m^{-3}}$
ϱ_{LC}	reference density (lower crust)	$2.90 \times 10^3\,\mathrm{kg\,m^{-3}}$
ϱ_{MA}	reference density (mantle)	$3.25 \times 10^3\,\mathrm{kg\,m^{-3}}$
ϱ_f	fluid density	$2.50 \times 10^3\,\mathrm{kg\,m^{-3}}$
η_f	fluid viscosity	$10^2\,\mathrm{Pa\,s}$
κ_0	reference permeability	$10^{-8}\,\mathrm{m^2}$
K_0	reference pore modulus	1 GPa
G	reference shear modulus	50 GPa
C	cohesion	40 MPa
ϕ	friction angle	30°
σ_T	tensile strength	10 MPa
T_0	reference temperature	293 K
T_s	surface temperature	293 K
T_b	bottom temperature	1573 K
α	melt weakening parameter	27
k	conductivity	$3\,\mathrm{W\,m^{-1}K^{-1}}$
c_p	specific heat capacity	$1.05 \times 10^3\,\mathrm{J\,kg^{-1}K^{-1}}$
α_v	thermal expansivity	$3 \times 10^{-5}\,\mathrm{K^{-1}}$
R	gas constant	$8.3145\,\mathrm{Jmol^{-1}K^{-1}}$
g	gravitational acceleration	$9.81\,\mathrm{m\,s^{-2}}$

With these experiments we investigate whether subsequent pulses rise more rapidly due to the previously weakened lithospheric host rock, and whether the additional supply aids the pulse in reaching the surface where it has been stagnating in crustal depths before. We introduce the second pulse at a late stage of the mentioned experiments, see Figure 4.8 (top two rows).

5.3.2 Medium-Sized Pulses

For a medium-sized pulse (roughly 10 km initial diameter) in a wet mantle we observed that the ascent stagnated when most of the pulse has reached the (mafic granulite) lower crust. After roughly 2 Myrs of stagnation with very little evolution we introduce a second pulse at 135 km depth that has the size and extent of the first pulse, see Figure 5.1.

The first pulse reaches a depth of 60 km after approximately 65 kyrs and

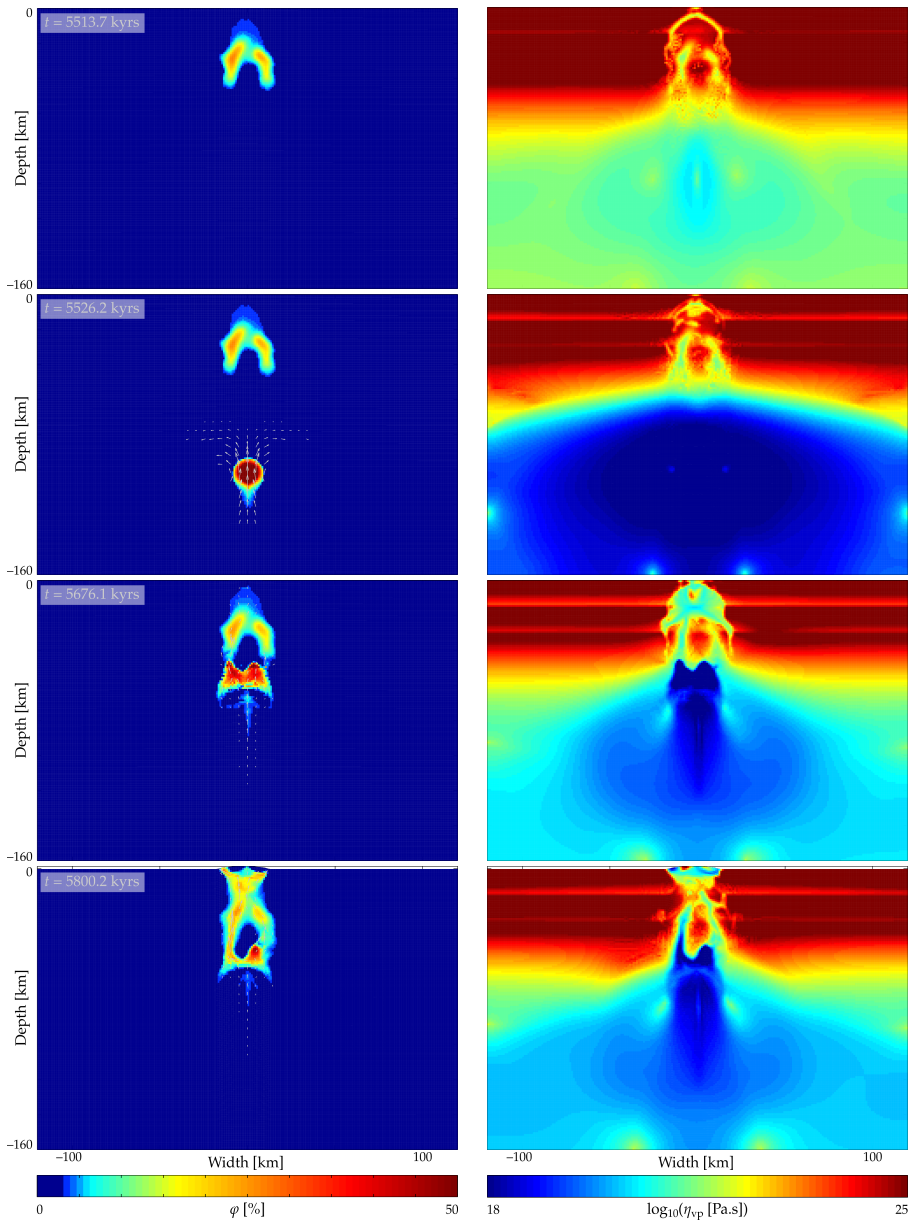

Figure 5.1: Porosity and fluid velocity arrows (left) and viscoplastic shear viscosity (right) during ascent of *second* medium-sized magma pulse in a wet mantle at zero background strain rate.

The pulse rises more rapidly than the first and barely splits into branches. It reaches the bottom of the previous pulse after roughly 65 kyrs. The additional supply leads to the melt rise to the upper crust and, ultimately, reach the surface within less than 300 kyrs after the second pulse has been introduced.

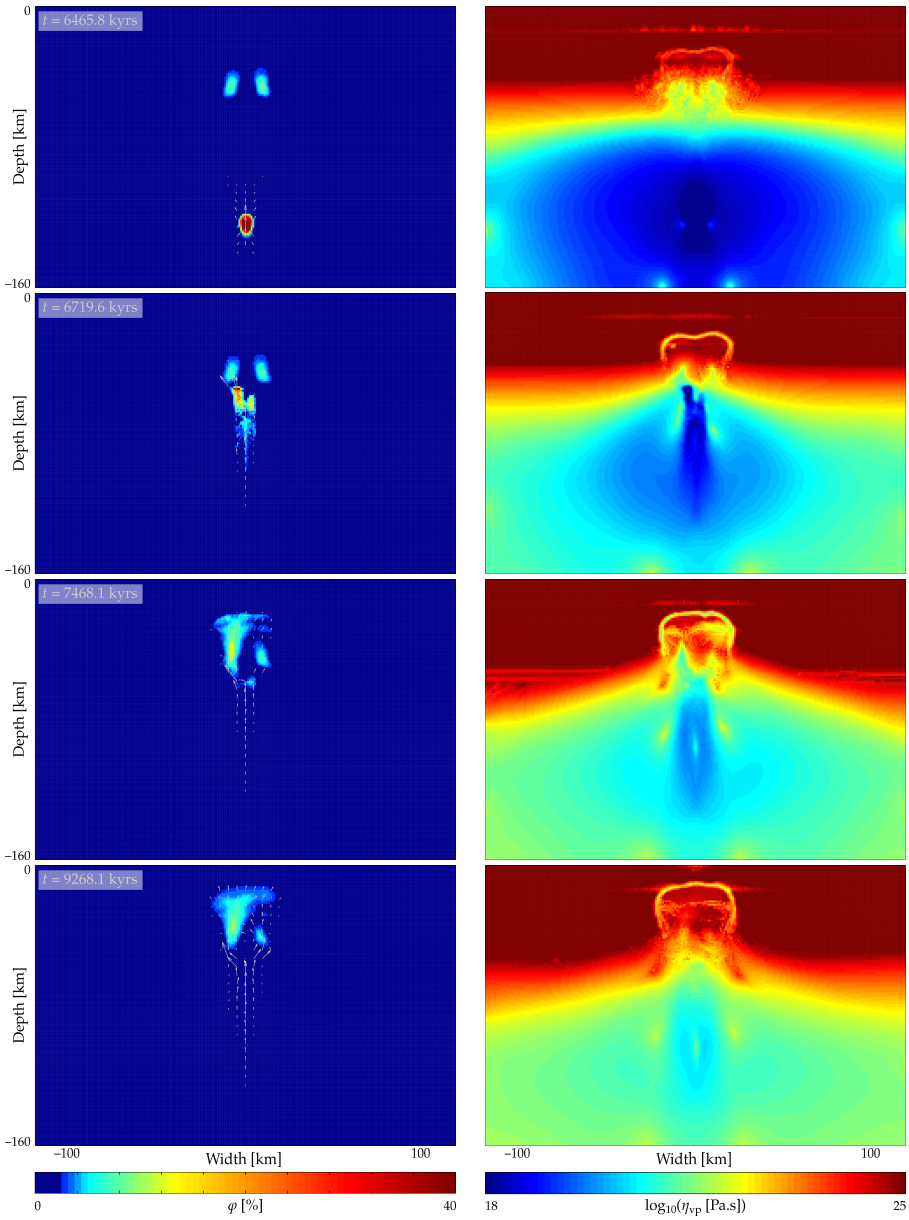

Figure 5.2: Porosity and fluid velocity arrows (left) and viscoplastic shear viscosity (right) during ascent of *second* small-sized magma pulse in a wet mantle at zero background strain rate.

Pulse branches into two parts that are indistinct compared to the previous pulse. Left branch dominates and merges with the previously settled magmatic body resuming the ascent. However, the upper crust is not reached within 10 Myrs.

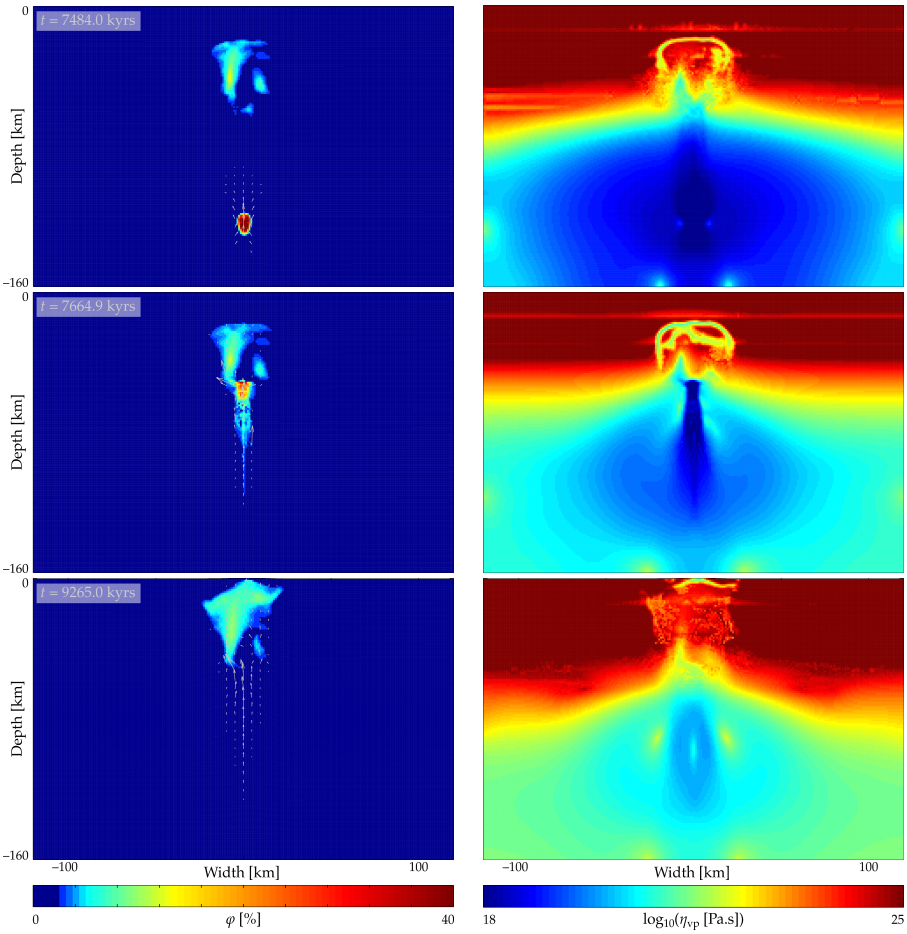

Figure 5.3: Porosity and fluid velocity arrows (left) and viscoplastic shear viscosity (right) during ascent of *third* small-sized magma pulse in a wet mantle at zero background strain rate.

Pulse mainly follows the path of the previous pulse, joining the magmatic body in the lower crust less than 200 kyrs after being introduced. The additional supply significantly supports the ascent making the pulse reach the surface after roughly 9.3 Myrs where we observed stagnation with two pulses.

starts splitting into two clearly distinct branches. The second pulse is introduced after 5513.7 kyrs, rises to 60 km depth within 45 kyrs and only slightly diverges laterally. When it reaches the bottom of the previously settled pulse, the porosity in the (first) left branch increases and the ascent continues to the upper crust. Ultimately, the pulse reaches the surface at an angle through two channels less than 300 kyrs after the second pulse has been introduced.

Parts of the second pulse remain below the right branch of the previous pulse possibly forming a magma chamber with a porosity of up to 40 %.

The shear viscosity drops accordingly, mainly in the left branch, and a network of low viscosity zones develops in the crust.

5.3.3 Small-Sized Pulses

We proceed in a similar way for a setup with a small pulse (5 km initial diameter). After about 3 Myrs the ascent of the first pulse stagnates. Another 3.4 Myrs later we introduce a second pulse with the size and extent of the previous. After a total time of roughly 7.4 Myrs the two pulses are merged and their ascent stagnates. At this stage we split the simulation as follows. One keeps running with the two pulses, to another one we introduce a third pulse.

Second Pulse The first (small) pulse reaches a depth of 60 km after about 160 kyrs. The second pulse rises at about the same velocity, being introduced at 6.45 Myrs and reaching 60 km depth after approximately 6.6 Myrs. It splits into two branches that slightly diverge following the pathways of the previous pulse, predominantly to the left. A large magmatic body develops in and below the lower crust, very similar to what we observed for a medium-sized pulse in the same rheological setup, see Figure 4.5.

After 7.5 Myrs the ascent stagnates, no fluid enters the upper crust within 10 Myrs. The shear viscosity develops structures that we already observed before, see Figures 4.6 and 4.7, with a low-viscosity rim around a higher viscosity region in crustal depths.

Third Pulse As a modification of the previous experiment we introduce a third pulse after 7468.1 kyrs (when we observe the ascent to start stagnating), see Figure 5.3. The third pulse reaches a depth of 60 km within 120 kyrs which is signicantly faster than the previous pulses. It adds fluid material to the magmatic body leading to higher porosity in the major supply structure and at its top rim, see Figure 5.4. Consequently, the pulse continues to ascend and reaches the surface after roughly 9.3 Myrs.

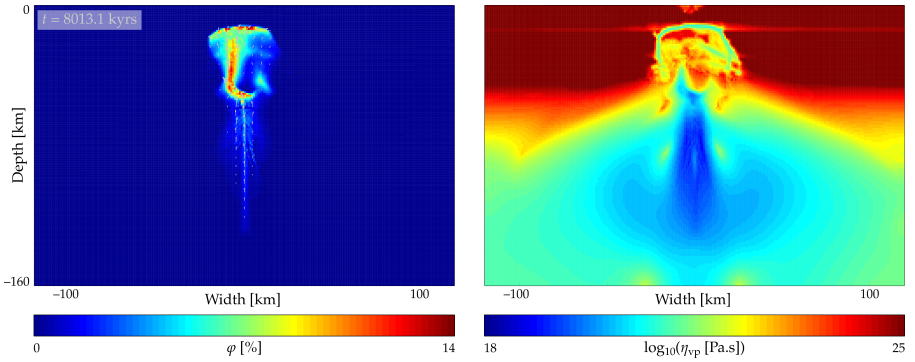

Figure 5.4: Snapshots of porosity and fluid velocity arrows (left) and viscoplastic shear viscosity (right) when third pulse has reached the previous pulses. Notice the modified porosity color scale compared to previous figures.

We observe that the porosity does not spread equally but instead focusses in the vertical major supply structure and at the top rim of the pulse.

5.4 Simultaneous Pulses and Mesh Adaptivity

5.4.1 Experimental Setup and Temporal Evolution

In this section, the porosity field of the initial setup differs from the setups presented so far. Instead of introducing a single circular melt pulse with porosity of up to 80 % we define a (rectangular) region with an equally distributed low, but increased porosity. Connolly and Podladchikov [8] have modelled the transport of asthenospheric melts with a similar initial condition. They observed vertically elongated waves spaced on the compaction length scale. However, they made a number of assumptions for simplification, such as constant shear viscosity and a non-deforming solid matrix.

We keep the domain size with depth 160 km and width 240 km and introduce a horizontally centered 40 by 10 km rectangular region at a depth of 135 km where we prescribe a randomized porosity between 1 and 10 % (and zero porosity elsewhere). The mantle rheology follows harmonically averaged wet olivine dislocation and diffusion creep laws, the lower crust mafic granulite dislocation creep, and the upper crust quartzite dislocation creep, see Table 4.2. The bottom and lateral boundaries follow a free-slip condition, the top boundary is held stress-free.

As we use a different power-law for the permeability and non-constant shear and compaction viscosities η, ζ, we cannot directly apply the reasoning of Barcilon and Richter [9] about the compaction length scale. Nevertheless, assuming characteristic viscosities in the mantle of $\eta = \zeta = 10^{18}\,\mathrm{Pa\,s}$, and a characteristic permeability in the range $\kappa \in [1,5] \times 10^{-9}\,\mathrm{m}^2$, we obtain a theoretical compaction length in the range $\delta \in [4.8, 10.8]$ km.

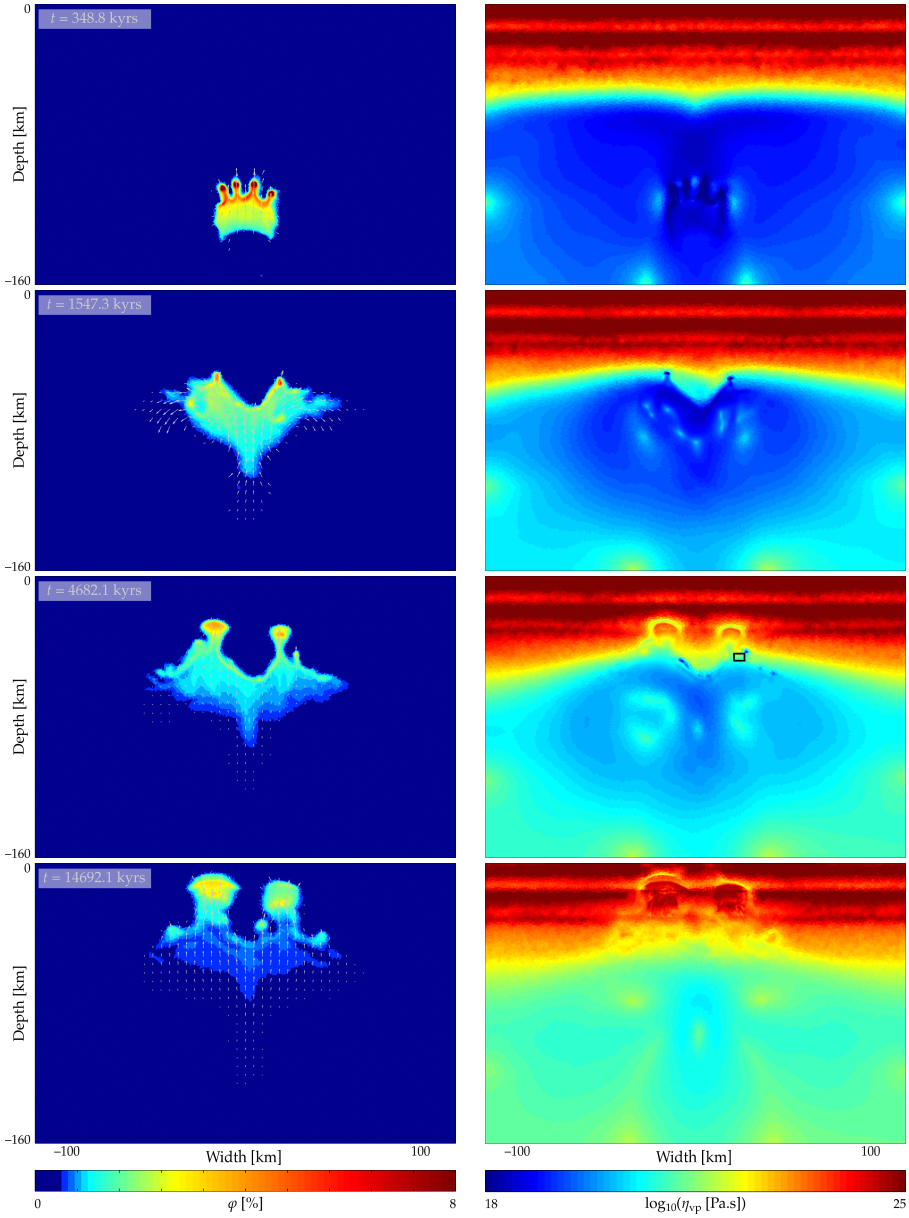

Figure 5.5: Porosity and fluid velocity arrows (left) and viscoplastic shear viscosity (right) during ascent of pulses developing simulatenously from region of initially randomized increased porosity in a wet mantle (lower crust mafic granulite) at zero background strain rate.

Pulses rise vertically first, then obliquely. While the outer pulses diffuse, the central pulses return to vertical ascent after 1.5 Myrs and later flatten, particularly in and just below the lower crust. Smaller pulses develop from trailing structure of increased porosity without reaching crustal depths.

The black rectangle indicates the mesh region shown in a blown-up view in Figure 5.6.

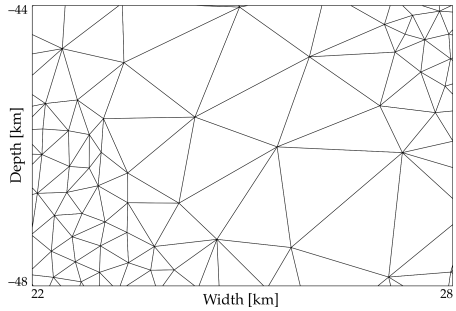

Figure 5.6: Blown-up view of the refined unstructured mesh after 4682.1 Myrs as indicated by the black rectangle in the shear viscosity field in Figure 5.5.

In the first 100 kyrs the fluid focuses at the top rim of the rectangular region, then four roughly equidistant pulses develop and start ascending. Their distance varies from about 7 to 10 km. In these pulses the maximum porosity reaches up to 16 % and the vertical fluid velocity is on the order of 10 cm/yr. The central pulses rise slightly faster than the outer ones. They reach a depth of 70 km after 690 kyrs and start diverging horizontally. By this time, the maximum porosity at the tip of the pulse has reduced to 6 to 7 %. From a depth of 55 km (after roughly 1.5 Myrs the two central pulses return to a vertical ascent. Meanwhile the other two pulses have diffused and stagnate in 70 km depth.

Below the (lower) crust the the two remaining pulses flatten, i.e., their size increases while the maximum porosity decreases. They reach the lower crust after about 3.7 Myrs. The ascending velocity strongly reduces (< 1 mm/yr) and the pulses spread out in the lower crust as well as, to some extent, in the upper crust in the following more than 10 Myrs. Some minor pulses rise from the trailing structure of increased porosity but remain well below the crust. However, the ascent of the left pulse does not stop before it reaches the surface after almost 18 Myrs.

5.4.2 Triangulation and Mesh Refinement

The domain triangulation is created using the open-source tool *Triangle*[1] by Jonathan Shewchuck [10]. The mesh is newly refined after every time step in regions where the porosity exceeds 1 %. In our implementation two major parameters control the refinement: the number of refinement steps and the "degree" of refinement. We apply two refinement steps, i.e., *(i)* we decide which triangles to refine and *(ii)* reduce the triangles' area by a factor (the "degree" of refinement) by remeshing. Then, *(iii)* we repeat steps *(i)* and *(ii)*.

[1]The source code is available from https://www.cs.cmu.edu/~quake/triangle.html.

An average element in our initial mesh, i.e., before it is refined, covers an area of roughly $1.54\,\mathrm{km}^2$. After the refinement, we reach a local resolution of $2.6 \times 10^{-2}\,\mathrm{km}^2$ increasing the total number of (velocity) nodes by only 20 %.

In Figure 5.6 we present a zoomed part of the mesh as indicated by the black rectangle in Figure 5.5 illustrating the refinement.

5.5 Discussion and Conclusions

We performed a small set of experiments with, on the one hand, multiple pulses of different sizes and, on the other hand, an initial setup with randomized porosity using an adaptively refined unstructured mesh. Even with the *ad hoc* introduction of additional pulses we were able to observe that pulses rise faster through a previously weakened lithospheric host rock and strongly support the further ascent of magmatic bodies previously emplaced in or below the crust.

The randomized porosity initial condition reproduces the porosity waves described in [8]. From this we deduce a compaction length scale of roughly 8.5 km which roughly coincides with theoretical results [9, 11]. As the setup evolves we obtain more complex behavior with phases of diverging pulses, vertical ascent in the uppermost mantle, and flattening of the pulse towards the crust.

As described in section 3.3.7 we use an explicit first-order method for time stepping. Refining the mesh in regions of increased porosity leads to a restrictive time step size as this also coincides in many cases with the regions of highest (fluid) velocities. Hence, the corresponding CFL criterion required to ensure numerical stability yields very small time steps (down to $< 1000\,\mathrm{yrs}$). Thus, a more advanced time stepping scheme would be of great benefit.

Mesh adaptivity is a powerful tool that by far has not been exhausted in the presented simulation. We expect it to be crucial in future studies on melt migration modelling. In addition to the level of porosity one could also consider, e.g., the viscosity gradient as refinement criterion. This would probably resolve the boundary between porosity-bearing and other regions particularly well.

References

[1] J. Dannberg and T. Heister. 3D Compressible Melt Transport with Mesh Adaptivity. Submitted, 2015.

[2] T. Keller, D. A. May, and B. J. P. Kaus. Numerical modelling of magma dynamics coupled to tectonic deformation of lithosphere and crust. *Geophysical Journal International*, 195(3): 1406–1442, 2013. DOI:10.1093/gji/ggt306.

[3] S. Rhebergen, G. N. Wells, A. J. Wathen, and R. F. Katz. Three-Field Block Preconditioners for Models of Coupled Magma/Mantle Dynamics. *SIAM Journal on Scientific Computing*, 37 (5):A2270–A2294, 2015. DOI:10.1137/14099718X.

[4] D. R. Scott and D. J. Stevenson. Magma ascent by porous flow. *Journal of Geophysical Research: Solid Earth*, 91(B9):9283–9296, 1986. DOI:10.1029/JB091iB09p09283.

[5] C. Wiggins and M. Spiegelman. Magma migration and magmatic solitary waves in 3-D. *Geophysical Research Letters*, 22(10):1289–1292, 1995. DOI:10.1029/95GL00269.

[6] H. Schmeling. A model of episodic melt extraction for plumes. *Journal of Geophysical Research: Solid Earth*, 111(B3):B03202, 2006. ISSN 2156-2202. DOI:10.1029/2004JB003423.

[7] A. Castro, T. V. Gerya, A. García-Casco, C. Fernández, J. Díaz-Alvarado, I. Moreno Ventas, and I. Löw. Melting Relations of MORB–Sediment Mélanges in Underplated Mantle Wedge Plumes; Implications for the Origin of Cordilleran-type Batholiths. *Journal of Petrology*, 51 (6):1267–1295, 2010. DOI:10.1093/petrology/egq019.

[8] J. A. D. Connolly and Y. Y. Podladchikov. Decompaction weakening and channeling instability in ductile porous media: Implications for asthenospheric melt segregation. *Journal of Geophysical Research: Solid Earth*, 112(B10), 2007. DOI:10.1029/2005JB004213.

[9] V. Barcilon and F. M. Richter. Nonlinear waves in compacting media. *Journal of Fluid Mechanics*, 164:429–448, 1986.

[10] J. R. Shewchuk. Triangle: Engineering a 2D Quality Mesh Generator and Delaunay Triangulator. In M. C. Lin and D. Manocha, editors, *Applied Computational Geometry: Towards Geometric Engineering*, volume 1148 of *Lecture Notes in Computer Science*, pages 203–222. Springer, 1996. ISBN 978-3-540-61785-3.

[11] V. Barcilon and O. M. Lovera. Solitary waves in magma dynamics. *Journal of Fluid Mechanics*, 204:121–133, 1989. ISSN 1469-7645. DOI:10.1017/S0022112089001680.

CHAPTER 6

SUMMARY AND OUTLOOK

Despite its importance many questions in magmatic processes remain open until the present day. One of the challenges inherent to driving our understanding of magmatism is the insufficient availability of data from the deep Earth. Gathered data comprises, e.g., geological outcrops and seismographic data. But interpreting data that is the result of millions of years of magmatic activity, tectonic deformation, surface processes, and putting it into a physically consistent model of the process yielding these results is cumbersome and topic of current research activities.

It is compelling to use numerical modelling to improve our understanding of melt migration processes. Different transport mechanisms have successfully been modelled numerically, mostly based on the work on generation and compaction of partially molten rock by McKenzie [1]. However, only recently a novel formulation of the model has been proposed by Keller et al. [2] combining it with lithosphere dynamics considering visco-elasto-plastic rheologies. For the first time, it has become possible to model lithospheric scale melt migration where different modes of transport (diapiric, percolative channelling, diking) arise self-consistently. Previous studies typically focussed on certain transport mechanisms prescribed by model assumptions which is insufficient when modelling melt ascent through the whole lithosphere, see, e.g., [3–5].

SUMMARY

The two major flow regimes decribing a coupled system of melt migration and lithosphere dynamics are Stokes and Darcy flow. In chapter 2 we focussed on (stationary) Stokes flow with strongly varying shear viscosity, derived and

tested a discontinuous Galerkin (DG) method using locally divergence-free approximation spaces. We compared this method to commonly used finite element methods using the Q_1P_0 or the Q_2P_1 element. Our main result was that, for the considered benchmark setups, the DG method was not superior to the second order finite element method when comparing computational expenses required to reach a certain accuracy.

In chapter 3 we formally derived our method to solve the coupled Stokes and Darcy problem avoiding methodological shortcomings of the study by Keller et al. [2]. We presented a stable method using suitable approximation spaces, we showed the validity of our implementation in geodynamically relevant setups, and we investigated the experimental order of convergence of the method. We found it to work robustly for a large range of physical and numerical parameters such as viscosity and mesh size.

In chapter 4 we applied the method introduced in the preceding chapter. We performed the first broad parameter study on melt migration on the lithospheric scale considering visco-elasto-plastic rheologies. We used realistic creep viscosities in an initially layered lithosphere (mantle, lower crust, upper crust) and introduced a circular Gaussian melt pulse with maximum porosity $\varphi = 80\,\%$ as initial condition. We varied, e.g., the rheological setup, the tectonic background deformation, and the size of the initial melt pulse. Among other results, we were able to relate the velocity of the ascent to the initial size of the pulse. Furthermore, we found deformational regimes leading to more efficient melt ascent. Also, we observed mafic granulite in the lower crust to pose a stronger obstacle than quartzite when no external deformation is applied. In contrast, for deformational regimes quartzitic lower crust is more resistive to rising melt.

Based on our findings in chapter 4 we focussed on two possible applications of the method in chapter 5, i.e., introducing multiple pulses with temporal offset mimicking episodic magmatism and showcasing adaptive refinement of an unstructured mesh with a modified initial setup where multiple pulses arise simultaneously from a region of increased, randomized porosity. We investigated how the rise of a melt pulse differs if the host rock has been weakened by a pulse that ascended before, and whether it leads to a continuation of stagnated ascent of the previous pulse.

Using the randomized porosity field we reproduced the equidistant porosity waves described by Connolly and Podladchikov [6]. The mesh adaptivity helped in resolving these initially very small pulses while keeping the computational expenses low. The rise of these pulses went through different phases of oblique as well as vertical ascent and flattening near the crust.

Model Limitations

As mentioned in section 4.5 there is several possible extensions of the model that are likely to improve its accuracy in depicting real-world magmatism. Among them are a more elaborated energy conservation equation and a model of melting and crystallization. The latter would ideally feedback to the viscosity of the partially molten material that we kept constant in every simulation.

Also, further investigation of the rheological stress-strain relationship is required as we did not observe the clearly distinct dikes in our experiments that Keller et al. [2] reported and that are (in crystallized form) well-known geological features.

The explicit first-order time stepping method is a numerical shortcoming that becomes particularly apparent when refining the mesh. Typically, the largest velocities are fluid velocities where the porosity is significant. As this is where we refine the grid, the CFL condition yields a very restrictive time step. Therefore, for future research it is necessary to introduce a different time stepping scheme such as second order implicit Runge-Kutta.

To more precisely capture the evolution of shear stress one could consider to explicitly include the integral term arising from the Maxwell body constitutive equation, see section 3.2.3. In addition, it would be mathematically more consistent to not split the advection terms from the remaining systems as described in section 3.3. Hence, investigating the effects of this could be beneficial.

Research Outlook

We described in section 3.6 that we implemented the method as part of the Matlab software MVEP2 that is and has been used extensively in teaching and research to solve Stokes flow in a variety of setups. Hence, it is immediately available to a significant user base. This has the obvious potential to lead to numerical reconstructions of numerous magmatic setups that have not been modelled numerically before with comparable capabilities.

Focussing on crustal plutons one could introduce (felsic) melt in the crust as initial condition and vary the tectonic regime to investigate the creation of dikes (during extension) and sills (under compression). For this a smaller scale computational domain could be considered and/or an adaptive mesh should be used to spatially resolve these features.

With a (constant or time-dependent) inflow boundary condition it would be possible to study the evolution of magmatic networks with prescribed additional melt supply on the lithospheric (or crustal) scale.

Investigating the formation of subduction zone arcs would be another application. This process is considered to be controlled largely by how melt migrates through the lithosphere [7, 8]. However, so far models of this were 1D or have not taken into account lithosphere dynamics.

As last example, one could model the crustal setup below Mt. St. Helens that has recently been imaged seismically in detail [9] to investigate how the different magmatic bodies interact, or how complex networks of crustal melt channels develop.

References

[1] D. P. McKenzie. The Generation and Compaction of Partially Molten Rock. *Journal of Petrology*, 25(3):713–765, 1984. DOI:10.1093/petrology/25.3.713.

[2] T. Keller, D. A. May, and B. J. P. Kaus. Numerical modelling of magma dynamics coupled to tectonic deformation of lithosphere and crust. *Geophysical Journal International*, 195(3):1406–1442, 2013. DOI:10.1093/gji/ggt306.

[3] V. Barcilon and F. M. Richter. Nonlinear waves in compacting media. *Journal of Fluid Mechanics*, 164:429–448, 1986.

[4] M. Spiegelman. Flow in deformable porous media. Part 2—Numerical analysis – the relationship between shock waves and solitary waves. *Journal of Fluid Mechanics*, 247:39–63, 1993. ISSN 1469-7645. DOI:10.1017/S0022112093000370.

[5] J. A. D. Connolly and Y. Y. Podladchikov. Compaction-driven fluid flow in viscoelastic rock. *Geodinamica Acta*, 11(2–3):55–84, 1998. DOI:10.1080/09853111.1998.11105311.

[6] J. A. D. Connolly and Y. Y. Podladchikov. Decompaction weakening and channeling instability in ductile porous media: Implications for asthenospheric melt segregation. *Journal of Geophysical Research: Solid Earth*, 112(B10), 2007. DOI:10.1029/2005JB004213.

[7] J. M. S. Solano, M. D. Jackson, R. S. J. Sparks, J. D. Blundy, and C. Annen. Melt Segregation in Deep Crustal Hot Zones: a Mechanism for Chemical Differentiation, Crustal Assimilation and the Formation of Evolved Magmas. *Journal of Petrology*, 53(10):1999–2026, 2012. DOI: 10.1093/petrology/egs041.

[8] C. Annen, J. D. Blundy, J. Leuthold, and R. S. J. Sparks. Construction and evolution of igneous bodies: Towards an integrated perspective of crustal magmatism. *Lithos*, 230:206–221, 2015. ISSN 0024-4937. DOI:10.1016/j.lithos.2015.05.008.

[9] Eric Hand. Fire down below. *Science*, 350(6262):725–726, 2015. DOI:10.1126/science.350.6262.725.

This page is left blank intentionally.

I hereby declare that I wrote the dissertation submitted without any unauthorized external assistance and used only sources acknowledged in the work. All textual passages which are appropriated verbatim or paraphrased from published and unpublished texts as well as all information obtained from oral sources are duly indicated and listed in accordance with bibliographical rules. In carrying out this research, I complied with the rules of standard scientific practice as formulated in the statutes of Johannes Gutenberg-University Mainz to insure standard scientific practice.

Lebenslauf

[…]